Wavefront shaping for stimulated emission depletion microscopy

Aurélien Barbotin

University College

University of Oxford

Supervisors: Prof. Martin Booth, Prof. Christian Eggeling

A thesis submitted for the degree of

Doctor of Philosophy

October 2020

Abstract

Super-resolution microscopy has significantly expanded the scope of application of biological microscopes by allowing the resolution of features smaller than the diffraction limit. Several super-resolution microscopy techniques exist, among which stimulated emission depletion (STED) microscopy has become a tool of choice for many biological applications, particularly in living specimens. STED has also proven useful as a tool for biophysics, thanks to its capability to be combined with fluorescence correlation spectroscopy (FCS). Unfortunately, the excellent resolution of STED microscopes comes at the cost of an increased experimental complexity, which limits the scope of potential applications. This is particularly true in deep, three-dimensional specimens, where optical aberrations and undepleted background significantly reduce measurement quality. In this thesis, we developed methods based on wavefront shaping to overcome these issues, for STED imaging and STED-FCS. We used for this an adaptive STED microscope equipped with a spatial light modulator for wavefront shaping, for which we first developed a bespoke calibration protocol. We particularly optimised the performance of z-STED, a STED confinement mode that increases the axial resolution and was so far scarcely used due to its sensitivity to optical aberrations. Using this newly calibrated z-STED microscope, we investigated the dynamics and structure of the plasma membrane of living cells. To image deeper in aberrating specimens, we developed a novel aberration correction method, based on a novel image quality metric developed in our lab. This method was then adapted to establish a new aberration correction method for STED-FCS, which we could use to increase the performance of z-STED-FCS in solution as well as in cells.

Finding suboptimal performance of z-STED-FCS even after aberration correction, we investigated the origins of background noise in STED-FCS in 3D and found that it could be minimised by means of coherent-hybrid STED created with a bivortex phase mask.

Acknowledgements

This thesis represents the outcome of more than three years of hard work: of my own off course, but also of the work of all the people who supported me during this project. First and foremost, I would like to thank Martin Booth, my supervisor, for giving me the opportunity to work in his lab, for initiating the great collaborative project I had the chance to work on, and for giving me the freedom to develop it in the way I wanted. Thanks to him, I believe I became a much better scientist than I was before, for which I am extremely grateful. I would also like to thank Christian Eggeling, my co-supervisor, for allowing me to join his lab. Thanks to this unique opportunity, I could discover what has now become one of my favourite techniques: FCS. As important as my supervisors to the success of this project were the postdocs who supervised and mentored me, especially at the beginning of the project. In order of apparition, I would therefore like to warmly thank Jacopo Antonello, Silvia Galiani and Iztok Urbančič. All three, in their manner, have become not only mentors but also good friends. They taught me a lot in their respective fields of expertise and I truly hope that we will work again together in the future. I would like to deeply thank my colleague and friend Erdinc Sezgin, for his mentoring and support, and for introducing me to the field of membrane research. I expect his influence to have a long-lasting impact on my scientific interests. I would like to thank Christoffer Lagerholm for his help with even my most peculiar

requests related to microscopes. A special thanks also goes to Jens Rittscher, who supervised my first rotation project and supported me through the beginning of my PhD. I could learn a lot from him about computer vision, a field for which I have a great interest. Even though she was not involved in my DPhil, I would like to warmly thank Ilaria Testa, my master thesis supervisor, whose teaching about STED microscopy made me incredibly well prepared to undertake this project. I would certainly have achieved less had it not been for my training in her lab.

When starting this PhD, I was hoping I could spend all my available time on my work to develop the best scientific project possible. Fortunately, this was made impossible by the great people I met during these years, some of whom I am proud to call my friends now. A comprehensive enumeration of what they did for me is beyond the scope of these acknowledgements, and I will instead focus here on a few anecdotes for each. I was lucky enough to have the friendship and support of Liliana Barbieri from my first day in Oxford. She was there when I needed it the most in my early isolated days in the UK, for which I cannot thank her enough. She also tried, though rather unsuccessfully, to teach me to "think outside the pub". I would like to warmly thank Falk Schneider, my conference mate who almost converted me to his motto "I don't care how the universe works, I want to know how lipids diffuse". Life at the WIMM would not have been the same had it not been for the legendary tea breaks, where so many interesting discussions happened with Dominc Waithe, Marco Fritzsche, Huw Colin-York and all other members of the nanoimmunology group and beyond, for which I would like to thank them

all. I want to thank here the FCS boys Valentin Dunsing and Pablo Carravilla, for all our useful and fun discussions. I would like to also thank all the members of the dynamic optics and photonic group for their support and kindness, as well as for the fantastic afterwork sessions we had at the Royal Oak. With this regard, I would like to thank especially Chris Chong and Andrew Kirkpatrick. The life of a student in Oxford is often marked by periodic changes in accomodation: at least mine was. This taught me valuable life lessons, such that moving house by foot and bus only is not a good idea (the experiment was repeated four times for statistical significance). Fortunately, it also allowed me to meet and live with fantastic flatmates who brightened my Oxford days: among them, I would like particularly to thank Huw Foden, Stefaan Feltes, George Zedginidze, Victor Lu, James Kirkpatrick, Shane D'Souza and Anna Booth for the great moments we spent together. I also want to warmly thank my classmates from the ONBI course, with whom we spent many unforgettable moments.

I want to thank both my mother Odile Hurpin and my father Christophe Barbotin for their continuous support throughout the four years of my DPhil, despite their initial reluctance with regard to my choice of host country. Finally, I want to express my gratitude to my dear Marion, whose uninterrupted kindness kept me happy even during the hardest times. She even tried to get interested in my research despite her aversion to anthing related to optics, to the point of learning the meaning of STED and FCS. I cannot thank her enough for her support.

Declaration

I hereby declare that except where specific references to the work of others are given, the contents of this thesis are original and have not been submitted in whole or in part for consideration for any other degree or qualification in this, or any other university. This dissertation is my own work and contains nothing which is the outcome of work done in collaboration with others, except in the following:

- Cells in chapter 4 were prepared and labelled by Dr Erdinc Sezgin
- Analysis of spectral data in chapter 4 (Figure 4.8) was performed by Dr Erdinc Sezgin
- Biological samples in chapter 5 were prepared fully, or in collaboration with, Dr Silvia Galiani, Dr Erdinc Sezgin and Dr Huw Colin-York
- Biological samples in chapters 6 and 7 were kindly prepared and provided by Dr Silvia Galiani

List of DPhil publications

1. Saha, D.; Schmidt, U.; Zhang, Q.; **Barbotin, A.**; Hu, Q.; Ji, N.; Booth, M. J.; Weigert, M.; Myers, E. W. Practical Sensorless Aberration Estimation for 3D Microscopy with Deep Learning. Opt. Express 2020, 28 (20), 29044. h

2. **Barbotin, A.**; Urbančič, I.; Galiani, S.; Eggeling, C.; Booth, M. Background Reduction in STED-FCS Using a Bivortex Phase Mask. ACS Photonics 2020, 7 (7), 1742−1753.

3. Tröger, J., Hoischen, C.; Perner, B.; Monajembashi, S.; **Barbotin, A.**; Löschberger, A.; Eggeling, C.; Kessels, M. M.; Qualmann, B.; Hemmerich, P. Comparison of Multiscale Imaging Methods for Brain Research. *Cells*, 2020, 25.

4. Antonello, J., **Barbotin, A.**, Chong, E. Z., Rittscher, J. and Booth, M. J. Multi-scale sensorless adaptive optics: application to stimulated emission depletion microscopy. *Optics Express 28*, 16749 (2020).

5. **Barbotin, A.**; Urbančič, I.; Galiani, S.; Eggeling, C.; Booth, M.; Sezgin, E. Z-STED Imaging and Spectroscopy to Investigate Nanoscale Membrane Structure and Dynamics. *Biophysical Journal* 2020, 118 (10), 2448−2457.

6. **Barbotin, A.**, Galiani, S., Urbancic, I., Eggeling, C., and Booth, M. J. (2019). Adaptive optics allows STED-FCS measurements in the cytoplasm of living cells. *Optics express, 27(16)*, 23378-23395

Acronyms

ACF autocorrelation function.

APD avalanche photodiode.

BFP back focal plane.

CH coherent-hybrid.

DM deformable mirror.

DWS direct wavefront sensing.

FCS fluorescence correlation spectroscopy.

FRC Fourier ring correlation.

FWHM full width at half maximum.

GUI graphical user interface.

MSD mean square displacement.

NA numerical aperture.

ODL optical delay line.

OTF optical transfer function.

PALM photoactivated localisation microscopy.

PBS polarisation beam splitter.

PMT photomultiplier tube.

PSF point spread function.

RESOLFT reversible saturable optical fluorescence transitions.

ROI region of interest.

SBR signal-to-background ratio.

SIM structured illumination microscopy.

SLB supported lipid bilayer.

SLM spatial light modulator.

SMS single molecule switching.

STED stimulated emission depletion.

STORM stochastic optical reconstruction microscopy.

TIRF total internal reflection.

WIMM Weatherall Institute of Molecular Medicine.

Contents

List of Figures

Chapter 1

Introduction

1.1 Context

Optical microscopes are one of the most important tools used in biological research. Initially made of a couple of lenses to magnify details too small to be visualised with a human eye, microscopes have since then significantly evolved. Multiple technical progresses contributed to a diversification of the types and capabilities of microscopes, which are now able to now acquire multiple types of data: two- and three-dimensional images, dynamic and spectral measurements, etc. One of the most widely used types of optical microscopes for biological research are fluorescence microscopes. Fluorescent microscopes offer to maximise image contrast and specificity by attaching fluorescent molecules to the structures of interest and collecting only the light emitted by these molecules. Like every optical microscopes, the resolution of fluorescent microscopes is limited by a diffraction limit which depends on the wavelength of light and on the numerical aperture of the objective lens and is usually comprised between 200 and 400 nm. In practice, two fluorescent emitters separated by less than the diffraction limit cannot be individually resolved. The diffraction limit can be bypassed by a class of microscopes named super-resolution micro-

scope that offer to selectively image a subset of fluorophores located in sub-diffraction areas instead of imaging all fluorophores at the same time. One of the main super-resolution techniques is named stimulated emission depletion (STED) microscopy. Thanks to its excellent resolution, STED has found many applications, essentially in cell biology and biophysics but also in other fields like neurosciences. STED can also be coupled with fluorescence correlation spectroscopy (FCS), a technique used to measure molecular diffusion speed and concentration within an observation volume. Together with STED, FCS allowed the measurement of diffusion speeds at different observation lengthscales, down to scales of 20-50 nm. This proved to be an extremely valuable tool, especially in membrane research, where the unique spatiotemporal resolution of STED-FCS allowed to monitor fast molecular interactions that were otherwise not observable. Unfortunately, the excellent resolution of STED microscopes comes with several drawbacks. A high power density leading to exacerbated photobloeaching and phototoxicity is usually considered to be the major drawback of STED microscopes, but is not the only one: a high sensitivity to optical aberrations in deep samples and high background levels in three-dimensional, dense samples have severely limited the applicability of STED microscopy in deep, non-flat samples.

1.2 Research contributions and outline of this thesis

1.2.1 Research contributions

The aim of this DPhil research work consisted in improving the performance of STED microscopy and spectroscopy in 3D and in aberrating specimens. For this, we used wavefront shaping to alter the shape of the STED depletion pattern, one of the key components of such microscopes. Using a spatial light modulator (SLM) as a wavefront shaping device,

we developed a protocol of alignment and calibration of a STED microscope, which we later used to investigate the structure and dynamics of biological membranes in 3D. We further developed methods to correct optical aberrations and to optimise the shape of the depletion pattern, both in the specific cases of imaging and FCS.

1.2.2 Outline of this thesis

1. In this chapter, I introduced this thesis work.
2. In the second chapter of this thesis, I reviewed the literature on the topics of interest and introduced the key concepts and methods used throughout this thesis.
3. In the third chapter, I detailed the protocol I developed for the calibration of SLM-based STED microscopes.
4. In the fourth chapter, I used STED microscopy and spectroscopy to investigate the dynamics and structure of closely spaced biological membranes.
5. In the fifth chapter, I developed an aberration correction protocol for STED imaging.
6. In the sixth chapter, I developed an aberration correction protocol for STED-FCS.
7. In the seventh chapter, I investigated how different STED confinement modes can be used to increase the performance of STED-FCS in 3D.

Chapter 2

Background

2.1 Conventional microscopy

2.1.1 Principles of microscopy

A microscope is a device used to observe details that would be too small to be observed by eye. Optical microscopes use for this a series of optical elements that increase the size of the image of an object in order to make it detectable, either by a human eye or a detector like a camera. Many different classes of microscopes exist, suited to different purposes and which differ in performance. Among them, fluorescence microscopes have become extremely popular for biological research. In fluorescence microscopy, a subset of the molecules within the sample are fluorescent. Upon illumination at a specific wavelength, these molecules emit photons at a longer wavelength (the difference between excitation and emission wavelengths is called Stokes shift). The emitted photons are collected by the microscope and photons at the excitation wavelength are filtered out. As a result, the only signal in theory collected by a fluorescence microscope originates from the fluorescent proteins inside the sample. Combined with a specific labelling of structures

of interest (for instance, antibody labelling or genetic expression of fluorescent proteins), fluorescence microscopy offers a prodigious contrast and specificity. The performance of such microscopes can be described with multiple parameters, some of which are listed here:

- **Resolving power** is the smallest detail that a microscope can resolve. Two objects separated by less than the resolution of a microscope cannot be told apart, while two objects separated by a larger distance can.
- **Optical sectioning** is the capability of a microscope to remove light emitted out of the plane of focus of the microscope[1].
- **Penetration depth** is the maximum depth at which imaging with a given microscope is possible. There is not a unique definition of penetration depth: it can be defined for instance at the depth at which the resolution or signal levels are halved. Penetration depth can be limited for instance by absorption, scattering or aberration of light by the specimen and is therefore heavily sample-dependent.

2.1.2 Image formation in fluorescence microscopy

Fluorescence microscopes contain at least two distinct optical paths: one for excitation of fluorescent molecules and one for detection of fluorescence light. There exist many different optical configurations for fluorescence microscopes, yet excitation and detection paths can be classified in two categories: widefield and point-scanning. In the case of the detection path of a **widefield** microscope, the entirety of the field of view is detected at once. The object plane is imaged by the objective and a set of relay lenses onto the chip of a camera.

In a **point-scanning** microscope, instead, the light from a single point is collected on a point-like detector. The position of the detection focus is moved across the sample (for example using galvanometric mirrors placed in an intermediate Fourier plane) to reconstruct an image. In most microscopes, excitation and detection paths are of a similar type (point-scanning or widefield) and share most of the same optical path, even though exceptions exist (for instance, multifocal confocal microscopes scan arrays of excitation foci which are detected by a camera [2]).

2.2 Super-resolution microscopy

2.2.1 The diffraction limit

The resolution of conventional fluorescence microscopes is ultimately limited by the diffraction limit. Due to the finite aperture of microscope objectives, the impulse response of these microscopes, named point spread function (PSF), is a diffraction spot that cannot be arbitrarily small. The Abbe resolution limit defines the maximum achievable lateral resolution of microscopes as:

$$d_{xy} = \frac{\lambda}{2n\sin(\alpha)} \tag{2.1}$$

where λ is the wavelength, n the refractive index of the propagation medium and α is the half angular aperture of the imaging device. Along the optical axis, the diffraction limit defined by Abbe is:

$$d_z = \frac{2\lambda}{NA^2} \tag{2.2}$$

In microscopy, light is usually collected by an objective which has a numerical aperture

(NA) defined as:

$$NA = n \sin(\alpha) \tag{2.3}$$

At visible wavelength, this makes it impossible to distinguish two features separated by less than a couple of hundreds nanometres: for instance, at 488 nm and with an objective with a NA of 1.4, the lateral and axial resolution limits are approximatively equal to 180 nm and 500 nm. This is higher by two orders of magnitude than the characteristic size of proteins, which are the building blocks of cellular processes, making many biological processes impossible to study with conventional microscopes. To circumvent this, several super-resolution microscopy methods capable of imaging structures smaller than the diffraction limit were developed. At least three of them are now widely used in biology: structured illumination microscopy (SIM) [3], which has a better resolution than conventional microscopes but is still diffraction limited, and single molecule localisation microscopy (SMLM) [4–6] and STED [7, 8] which are not limited by diffraction.

2.2.2 Single molecule localisation microscopy

Two emitters separated by less than the diffraction limit defined in equation 2.1 cannot be individually resolved at the same time. However, if two such emitters can be imaged one by one, they can be individually localised with sub-diffraction precision and a super-resolved image can be reconstructed. This principle is at the core of super-resolution microscopy. SMLM offers to resolve individual fluorophores well below the diffraction limit by addressing one molecule at a time. In photoactivated localisation microscopy (PALM), widefield super-resolution localisation of individual molecules is achieved by stochastically exciting a sparse subset of fluorophores. They are then localised and bleached[4, 5].

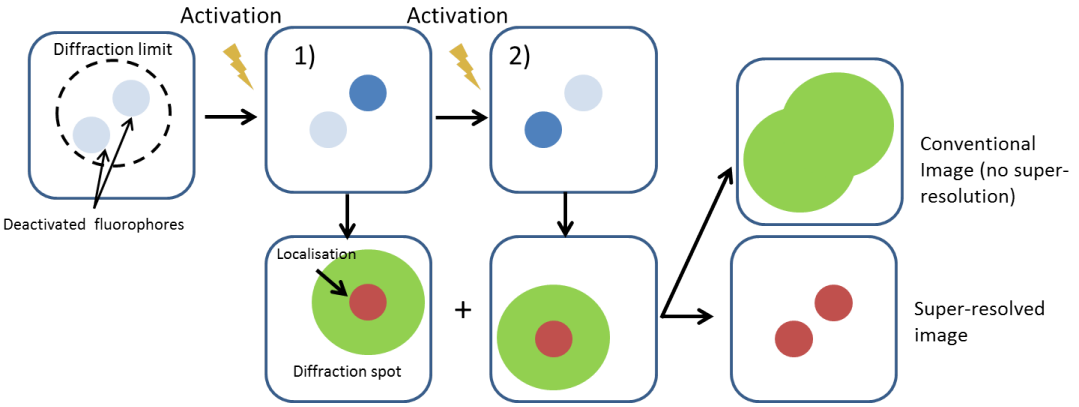

Figure 2.1: Principle of SMLM microscopy. Left: A subset of fluorophores separated by less than the diffraction limit (dotted black line) are activated one by one (middle, top row) and localised with subdiffraction precision (middle, bottom row). The fluorophores can be separated in the reconstructed image (bottom right), but not in a conventional image (top right).

This process is afterwards repeated to localise most of the molecules in the field of view.

A similar technique, named stochastic optical reconstruction microscopy (STORM)[6], used reversible off-switching of fluorophores instead of photobleaching to image different subsets of fluorophores (using either reversibly switchable fluorescent proteins or blinking fluorophores). The principle of SMLM is illustrated in Figure 2.1.

Labelling is critical in SMLM, and in certain samples photobleaching could limit the maximum achievable resolution. This could be alleviated using diffusing fluorophores which were localised once immobilised by their target (point accumulation for imaging in nanoscale topography (PAINT) [9]), and were therefore constantly replenished. SMS methods rely on precise localisations of individual fluorescence emitters. First implementations relied on simply fitting individual fluorescence spots with a model of the lateral PSF of the microscope, usually a two-dimensional Gaussian [4]. Sub-diffraction axial information could be gained using a more advanced optical configuration, either based on PSF engineering [10–13] or using the near-field component of light for localisations close

to the coverslip [14]. Recently, MINFLUX increased the localisation accuracy by an order of magnitude [15], both laterally and axially [16] using a ring-shaped detection PSF. SMLM however suffers from major shortcomings. First, SMS requires specific fluorophores that can either blink or be photoactivated, in turn imposing specific conditions on the properties of the imaging medium. Besides, in SMLM, image reconstruction requires hundreds or even thousands of frames, leading to acquisition times generally in the order of minutes and thus precluding most applications in living, moving specimens. STED, on the contrary, is a super-resolution technique with a speed comparable to that of confocal microscopy and is as such preferred to SMLM for live specimen imaging.

2.2.3 STED microscopy

STED microscopy is a particular case of a class of microscopes called reversible saturable optical fluorescence transitions (RESOLFT) microscopes [17]. These microscopes are point-scanning microscopes in which the effective excitation area is reduced below the diffraction limit by means of a deterministic transition from the bright state to the dark state of fluorescent molecules. This is achieved with a laser focus shaped to exhibit a central intensity minimum. This focus is overlaid to the excitation focus, quenching the fluorescence of molecules located in the periphery of the excitation focus and allowing the emission of fluorescence light in the centre. Different sorts of RESOLFT microscopes exist, which rely on different quenching mechanisms. The acronym RESOLFT is generally used improperly to refer to the specific case when reversibly switchable proteins are used to quench fluorescence [18], although in principle it refers to the more general approach described above. The first and most common implementation, STED [7, 8], uses instead stimulated emission as a fluorescence depletion mechanism (Figure 2.2).

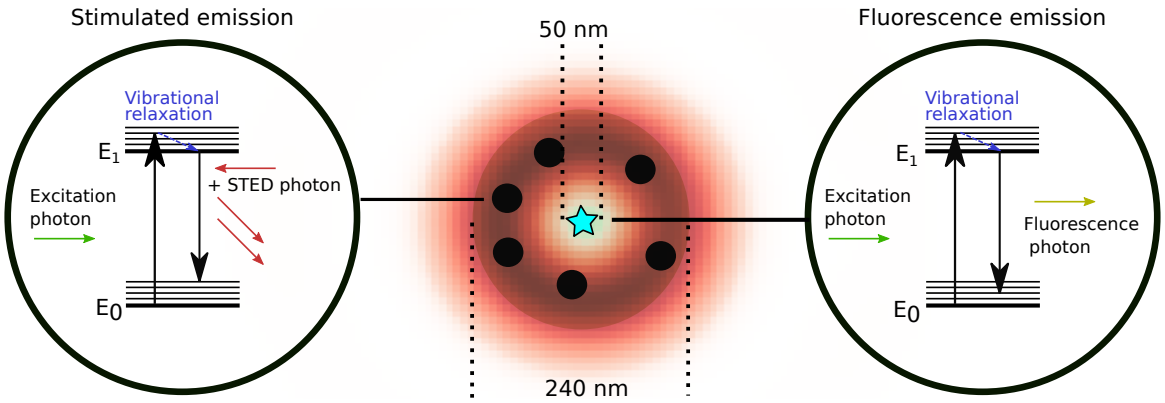

Figure 2.2: Principle of STED microscopy. A diffraction-limited excitation focus (gray circle) is overlaid with a depletion pattern (red ring) with a longer wavelength. Fluorophores in the areas of high depletion intensity (black circles) undergo stimulated emission, while fluorophores in areas of low depletion intensity (cyan star) undergo fluorescence emission. Insets: Jablonski diagrams describing the stimulated emission (left) and fluorescence emission (right) processes.

In a diffraction-limited point-scanning microscope, fluorophores within the excitation area are excited by a photon from the excitation laser, inducing an electronic transition from the ground state E_0 to an excited state E_1. After a vibrational relaxation occurring much faster than the rest of the fluorescence process (1-5 ps as opposed to the nanosecond timescale of the fluorescence emission process [7]), the electron relaxes to its ground state, emitting a photon in the process (Figure 2.2, right). In presence of a red-shifted laser with a high enough intensity, excited electrons undergo stimulated emission instead and emit two identical photons while relaxing to a high vibrational level (Figure 2.2, left). Photons that underwent stimulated emission have a longer wavelength than fluorescence photons and can be filtered using a dichroic filter. If the depletion laser exhibits a central intensity minimum (for instance if it is ring-shaped), only photons emitted in the centre of the focus are collected, while photons emitted elsewhere undergo stimulated emission and are discarded. This results in a fluorescence emission area effectively smaller than the diffraction limit (Figure 2.2).

In practice, the size of the effective area where fluorescent photons can be emitted depends on the intensity of the STED laser. Indeed, the probability of photon emission under depletion by the (pulsed) STED laser at a given position in space r writes as [19]:

$$\eta(r) = exp\left(-\sigma\tau I_{STED}(r)\right) \tag{2.4}$$

where σ is the cross-section for stimulated emission, τ the STED pulse duration and $I_{STED}(r)$ the spatially-varying STED laser intensity. Assuming a parabolic distribution of the STED intensity around its central intensity minimum, the full width at half maximum (FWHM) of the STED emission area scales as [20]:

$$d = \frac{d_c}{\sqrt{1 + d_c^2 a^2 I_{STED}/I_S}} \tag{2.5}$$

where d_c is the confocal FWHM, a is a constant that depends on the width of the depletion pattern and I_S is the saturation intensity, defined as the STED intensity reducing by half the probability of fluorescence emission.

2.3 STED imaging in 3D

2.3.1 Different STED confinement modes

The depletion beam is a crucial component of a STED microscope. Its shape determines the mode of confinement of the STED focus, e.g. the direction along which resolution is increased. The most common STED depletion beam is a ring-shaped focus (sometimes referred to as "doughnut-shaped" beam) generated with a vortex phase mask which increases the lateral resolution but leaves unchanged the axial resolution (Figure 2.3(a)). This depletion beam was already used in early STED implementations [19, 21, 22] and is conveniently used thanks to its relative simplicity of operation and resistance against

spherical aberrations [23–25]. Several variations of the ring-shaped focus exist, generally designed to increase its size to allow for a better axial overlap between excitation and depletion beams. This was performed by slightly underfilling the NA of the objective [26], or by using a second order vortex phase mask [27] (with a phase ranging from 0 to 4π instead of 0 to 2π). A different STED depletion pattern can be created with a phase mask made of an inner phase disk with a constant phase value of 0 rad and an outer ring with a phase value of π (the "top-hat" phase mask). This depletion pattern was also used in the early days of STED microscopy to increase mostly the axial resolution (z-STED) [28] (Figure 2.3(b)). To increase resolution along all three dimensions, a combination of 2D- and z-STED depletion patterns was proposed [26] (3D-STED, Figure 2.3(c)).

As being crucial parts of STED microscopes, the design of depletion patterns has drawn considerable attention. Simulations showed that when generated as phase holograms, optimal lateral and axial confinements could be obtained with respectively helicoidal and top-hat phase masks and Gaussian illumination [17]. Interestingly, it was found later that using annular instead of Gaussian excitation together with a helicoidal phase mask was shown to improve performance of 2D STED microscopy [29]. Recently, using the simplicity of SLMs to generate any phase mask, a new confinement mode called coherent-hybrid (CH) STED, created by means of a bi-vortex phase mask, was shown to offer an excellent trade-off between image contrast and lateral and axial resolution [30] (Figure 2.3(d) and chapter 7).

To increase the acquisition speed of STED images, STED microscopy could be parallelised by means of optical lattices of excitation and depletion patterns and camera-based detection [31]. This requires however an extremely high depletion laser power, which scales linearly with the number of depletion patterns created. For this reason, parallelisation of the depletion patterns was more frequently employed for RESOLFT microscopy

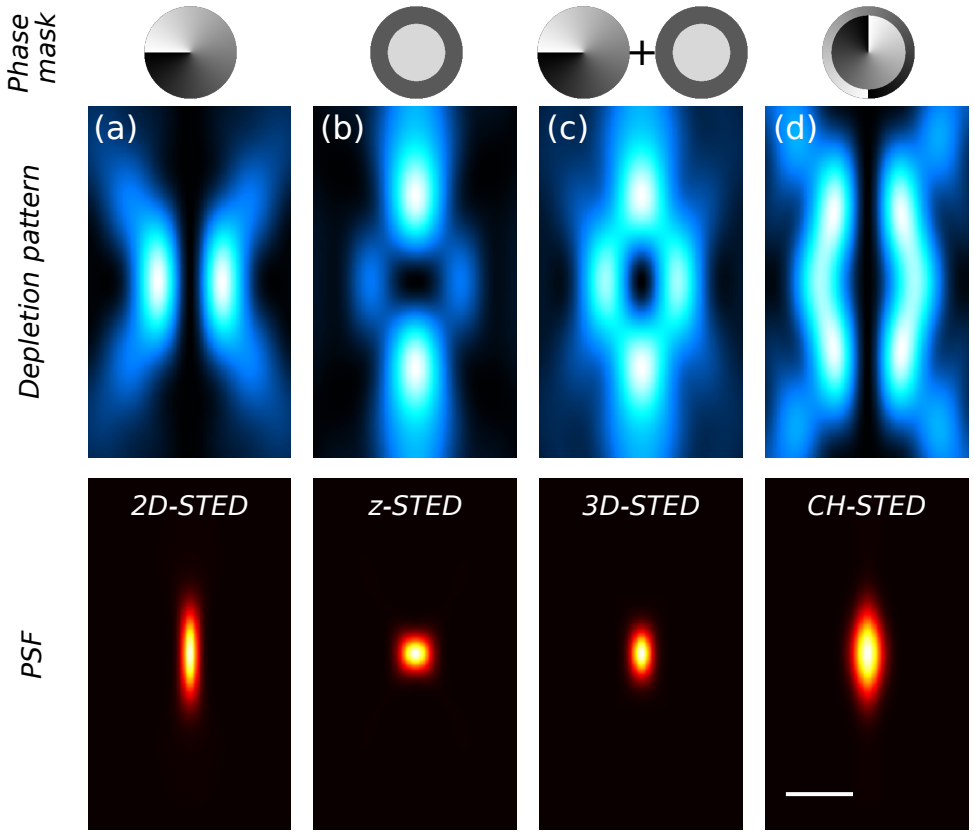

Figure 2.3: Available confinement modes for STED microscopy, simulated using vectorial diffraction theory. Phase masks (top) used to create the depletion pattern (middle) and effective PSF (bottom) for (a) 2D-STED, (b) z-STED, (c) 3D-STED and (d) CH-STED. Scalebar: 500 nm.

with reversibly photoswitchable proteins, requiring order of magnitude less light for fluorescence quenching [2, 32, 33].

Three-dimensional resolution improvements could be obtained in STED by a combination of 2D-STED with total internal reflection (TIRF) illumination [34] or supercritical angle fluorescence detection [35] to increase spatial resolution along all three dimensions, however only at the surface of a coverslip. The best axial resolution in STED microscopy could be obtained by means of two opposite objectives in a 4pi configuration [36–39]. This approach came at the cost of a much higher experimental complexity and suffered

from specific artefacts due to fluorescence emitted in undepleted areas, which had to be removed using either postprocessing or optically by adding aberrations to the depletion beam [40].

2.3.2 3D applications of STED microscopy

Many applications of STED microscopy were found in flat samples, using 2D-STED. This STED confinement mode was widely used, thanks to its relative simplicity and robustness as compared with other STED confinement modes. This approach did not however have a sufficient axial resolution and optical sectioning for all applications in dense, three-dimensional samples and different confinement modes were then used. z-STED was used in such circumstances, despite it being more scarcely used than 2D-STED [28, 41, 42]. Using 3D-STED to increase the spatial resolution along all three dimensions, more applications were found [26, 43–46]. 3D-STED was generally considered to be more prone to photobleaching than 2D-STED, for several reasons. First, due to the exacerbated experimental complexity (requiring among other things a precise coalignement between the 2D- and z-STED depletion patterns), 3D-STED is likely to exhibit an imperfect central intensity minimum. Besides, the fluorescence emission volume being by design smaller than in 2D-STED, less fluorophores are able to emit light at a time and thus higher excitation powers or longer exposure times are necessary to reach similar signal levels. Finally, imaging 3D samples often necessitates the acquisition of entire volumes instead of single frames, thus leading to an increased photoexposure. For these reasons, many 3D-STED applications were developed together with methods to reduce the impact of photobleaching [47–49]. In dense samples where background noise can become a problem, 3D-STED was successfully used with background substraction methods [27, 50, 51].

2.4 Fluorescence correlation spectroscopy

2.4.1 Principle

FCS is a technique used to measure properties like diffusion speed or molecular concentration of fluorescent molecules in motion. In FCS, the fluctuations of the fluorescence intensity within a given confocal observation volume are recorded. These fluctuations can be caused by either molecular diffusion through the confocal volume (Figure 2.4(a)), molecular blinking caused by triplet state kinetics or molecular binding and unbinding [52]. For instance, a fluorescent molecule diffusing in and out of an observation volume induces a burst in intensity which duration is equal to the transit time of the molecule in the observation volume.

When more than one molecule is present in the observation volume at once, single bursts cannot be separated and intensity fluctuations are recorded instead (Figure 2.4(b)). Information about the underlying molecular properties can be accessed by calculating the autocorrelation function (ACF) of these fluctuations (Figure 2.4(c)). Fitting the resulting FCS curve with a biophysical model, it is possible to extract parameters such as average transit time in the observation volume (as a characteristic decay time of the FCS curve) or average number of molecules in the focal volume (as inverse of the amplitude of the ACF).

2.4.2 Mathematical framework

Autocorrelation function

Given a lag time τ, FCS measures the similarity between the fluorescence signal $I(t)$ and the signal shifted in time $I(t+\tau)$. If the characteristic time of the dynamic observed is smaller than τ, there is no correlation between $I\,(t)$ and $I\,(t+\tau)$. On the other hand,

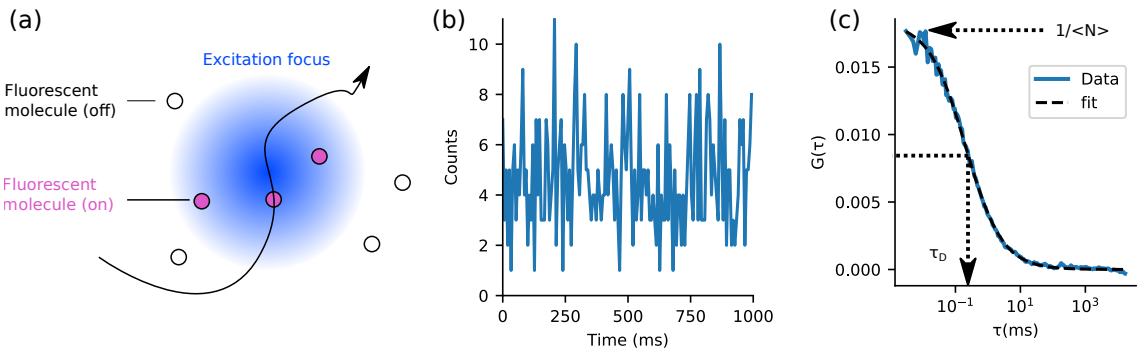

Figure 2.4: Principle of FCS. (a) Fluorescent molecules (small black circles), emit photons (magenta) when located inside an excitation focus (blue circle). Diffusion of these fluorescent molecules in and out of the excitation focus create intensity fluctuations (b) containing information about the underlying molecular diffusion speed and concentration, which can be accessed using the corresponding FCS curve (c), calculated as the autocorrelation function of the signal. Fitting the curve with a biophysical model allows retrieving parameters such as average number of molecules in the observation volume ⟨N⟩ and average molecular transit time τ_D

if τ is smaller than the characteristic time of the dynamic observed, $I\,(t)$ and $I\,(t+\tau)$ are strongly correlated. This can be numerically calculated using the ACF $G(\tau)$:

$$G(\tau) = \frac{\langle \delta I(t) \delta I(t+\tau) \rangle}{\langle I(t) \rangle^2} \tag{2.6}$$

where $\langle . \rangle$ is the time-averaging operator and $\delta I(t) = I(t) - \langle I(t) \rangle$. For a given intensity timetrace I, the autocorrelation function is calculated for a range of lag times τ that typically vary between a lower bound τ_{min} equal to the sampling rate and a higher bound τ_{max} equal to the total acquisition time. The resulting curve (Figure 2.4(c)) is named FCS curve. Quantitative parameters can be measured by fitting the FCS curve with a biophysical model, which depends on the shape of the observation volume [53] and on the process observed. In this thesis, we used FCS essentially to measure molecular diffusion. The simpler and most common model for molecular diffusion is the brownian motion, in which

the mean square displacement (MSD) is described as:

$$MSD\,(t) = 6Dt \tag{2.7}$$

where t is the time and D the diffusion coefficient. In this case, if the observation volume is Gaussian, the theoretical FCS curve is described as [52]:

$$G_D(\tau) = \frac{1}{N}\frac{1}{1+\tau/\tau_{xy}}\frac{1}{\sqrt{1+\frac{1}{K^2}\frac{\tau}{\tau_{xy}}}} + \delta \tag{2.8}$$

where N is the apparent average number of molecules in the observation volume, δ is an offset, τ_{xy} is the average lateral molecular transit time in the observation volume, K is the aspect ratio of the Gaussian effective observation volume (or effective optical point-spread function (PSF)) defined as $K = \omega_z/\omega_{xy}$, where ω_z is the axial and ω_{xy} the lateral $1/e^2$ radius. The transit time τ_{xy} depends on the diffusion coefficient and the size of the observation volume:

$$\tau_{xy} = \frac{\omega_{xy}^2}{4D} \tag{2.9}$$

Diffusion through certain fluids however does not follow a Brownian diffusion, but an anomalous diffusion instead:

$$MSD\,(t) = 6At^{\alpha} \tag{2.10}$$

Where A is a pseudo-diffusion coefficient. The exponent α defines the diffusion modality: if $\alpha < 1$, the diffusion is said to be subdiffusive, while the specific case $\alpha = 1$ corresponds to Brownian diffusion (equation 2.7). In case of anomalous diffusion, the theoretical FCS curve follows:

$$G_D(\tau) = \frac{1}{N}\frac{1}{1+(\tau/\tau_{xy})^{\alpha}}\frac{1}{\sqrt{1+\frac{1}{K^2}\left(\frac{\tau}{\tau_{xy}}\right)^{\alpha}}} + \delta \tag{2.11}$$

and the transit time can be expressed as

$$\tau_{xy} = \left(\frac{\omega_{xy}^2}{4A}\right)^{\frac{1}{\alpha}} \tag{2.12}$$

Intensity fluctuations can be caused not only by molecular diffusion, but also by blinking caused by molecules entering and leaving a dark triplet state. The corresponding FCS curve is the following:

$$G_T(\tau) = 1 + \frac{T}{1-T}\exp^{-\tau/\tau_T} \tag{2.13}$$

where T is the average triplet amplitude and τ_T is the triplet correlation time. The theoretical FCS curve obtained for molecular diffusion in presence of a triplet state is the product of both models (equations 2.7 and 2.13)

$$G(\tau) = G_D(\tau)\, G_T(\tau) \tag{2.14}$$

Moment analysis

Some information about the properties of the sample can readily be accessed without correlating the intensity timetraces. It can be shown that the average number of molecules in the observation volume can be calculated as [54]:

$$N = \frac{\langle I \rangle^2}{\left\langle (\Delta I)^2 \right\rangle - \langle I \rangle} \tag{2.15}$$

where $\left\langle (\Delta I)^2 \right\rangle$ is the variance of the fluorescence intensity signal. The substraction of the average of the intensity signal to its variance in the term $\left\langle (\Delta I)^2 \right\rangle - \langle I \rangle$ accounts for Poisson noise. The intensity signal I is a dimensionless quantity and as such equation 2.15 is homogeneous. From this expression, the average molecular brightness (number of photons emitted per unit of time per molecule) can be expressed as:

$$\epsilon = \frac{\left\langle (\Delta I)^2 \right\rangle - \langle I \rangle}{\langle I \rangle} \tag{2.16}$$

2.4.3 STED-FCS

Conventional implementations of FCS make use of confocal optics and are thereby limited in resolution by diffraction. This prevents measurement of diffusion speeds at lengthscales below 200 nm. Fortunately, FCS can be used in a STED microscope to remediate to this (STED-FCS) [55–57]. One of the most important features of STED-FCS is its ability to measure diffusion speeds at different scales, which enables to observe different diffusion modes. One of the first applications of STED-FCS consisted in measuring the diffusion speed of fluorescent lipid analogues in the plasma membranes [56], revealing that certain lipids transiently assemble in nanodomains. STED-FCS was later used in a wealth of studies involving the plasma membrane [58–61].

When doing STED-FCS in 3D environments, issues caused by out-of-focus non correlating background occur [57, 62]. This background could be limited by confining the fluorescence emission volume using TIRF illumination [63], but is fundamentally limited to experiments close to the coverslip. STED-FCS in 3D environments could also be performed thanks to background substraction methods, either with continuous-wave STED and filtering photons based on their lifetime [64], or by using a double depletion scheme [27].

2.5 Adaptive Optics in microscopy

2.5.1 Principles

Propagation of light through tissues with an inhomogeneous refractive index induces wavefront distortions called optical aberrations. Using adaptive optics, sample-induced distortions can be compensated to recover an ideal measurement quality (Figure 2.5). To

achieve this, three elements are needed:

1. An adaptive element
2. A method of aberration measurement
3. A control system

One of the simplest and most common forms of adaptive optics in microscopy consists of using the correction collar of an objective to correct for spherical aberrations. In this case, the adaptive element is the collar, the aberration measurement is indirectly performed by the user who deems an image as 'good' or 'bad' and the control system is again the user, who chooses the collar position yielding the best image quality. This simple adaptive optics system is useful in many situations, but is limited to systems exhibiting only spherical aberrations. As common biological specimens are prone to more complex aberrations [65–67], more elaborate methods are necessary.

Two different kinds of adaptive elements are commonly used in AO for microscopy, called deformable mirror (DM) and SLM. DMs are made of a reflective surface that can be mechanically deformed using a certain number of actuators; they have the advantage to modulate phase irrespective to wavelength and polarisation, but have a limited number of actuators (and so of degrees of freedom) relatively to SLMs. SLMs are arrays of liquid crystals that can be controlled with an electric field, changing their apparent refractive index to change the phase of incident light. Unlike DMs, SLMs modulate only polarised light and the phase shift induced by the liquid crystals is wavelength-dependant. For these reasons, SLMs are usually found in excitation paths and do not modulate the phase of any fluorescence light, while DMs can be used in any optical path.

The aberration measurement system is usually the most sensitive part of an AO

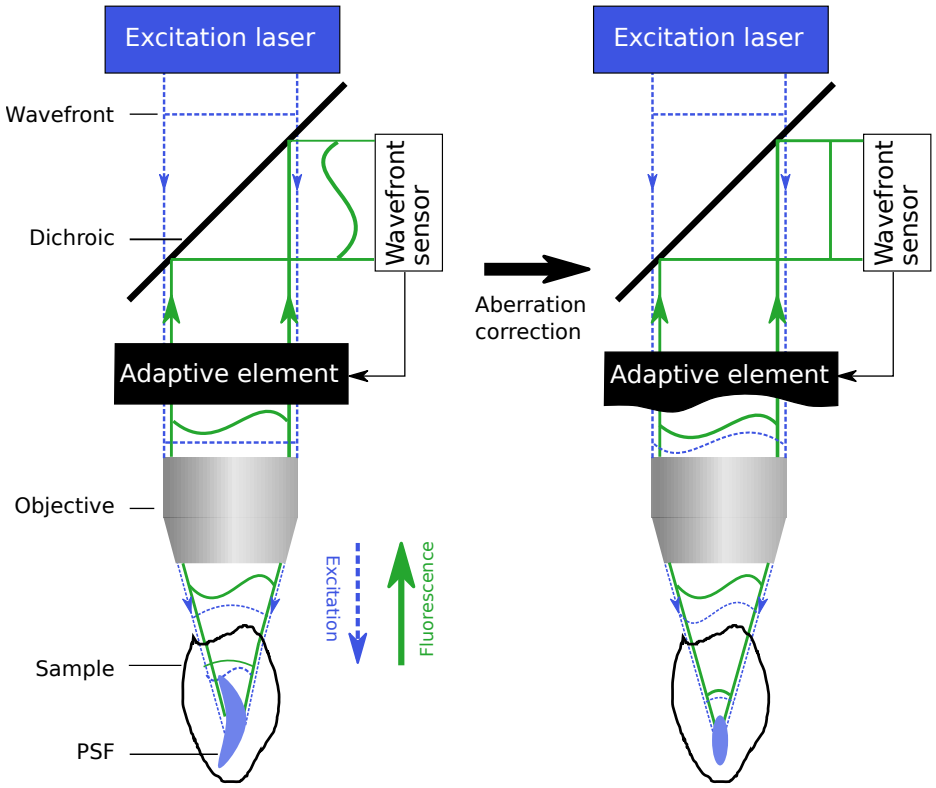

Figure 2.5: Principle of adaptive optics for fluorescence microscopy: example of a point-scanning microscope. Left: An aberrating specimen (black blob) distorts the wavefront of the excitation laser, leading to an enlarged PSF. Using the fluorescence signal, a wavefront sensor or detector measures the wavefront deformations and drives the shape of the adaptive element accordingly. Right: The adaptive element compensates the aberrations introduced by the sample, recovering a diffraction-limited PSF.

scheme in microscopy. Indeed, it is impossible to directly measure phase and all phase-measurement techniques rely on encoding phase information into intensity variations. As a result, different wavefront sensing methods were developed, each with advantages and drawbacks.

2.5.2 Wavefront sensing methods

Wavefront description

The wavefront is a 3D surface with equal optical path length which is orthogonal to light rays at every point. In an ideal optical setup, in absence of any aberrations, the wavefront in the back focal plane of the objective is flat. Aberrations distort it. These distortions and can be conveniently represented as a sum of Zernike polynomials, a family of polynomials orthogonal on the unit disk. Zernike polynomials are usually represented in polar coordinates and separated into a product of a radial polynomial and of an angular function [68]. Both these radial polynomial and angular function can be uniquely defined with a single positive integer named the radial and angular *order* of a Zernike mode. For a given radial and angular order m and n, it is possible to define an even and an odd polynomial as:

$$\begin{cases} Z_n^m(\rho,\phi) = \sqrt{2n+1}R_n^{|m|}(\rho)\cos(m\phi) & even \\ Z_n^{-m}(\rho,\phi) = \sqrt{2n+1}R_n^{|m|}(\rho)\sin(m\phi) & odd \\ Z_n^0(\rho,\phi) = \sqrt{n+1}R_n^0 & m=0 \end{cases} \tag{2.17}$$

where m and n are positive integers and verify $n \geqslant m$ and $R_n^m(\rho)$ is a polynomial of degree n, the exact definition of which can be found for instance in [68]. ρ and ϕ are the radial and angular coordinates and vary respectively between 0 and 1 and 0 and 2π.

It is convenient to refer to a specific Zernike mode using a single number instead of two and several ordering conventions exist. We chose to use the standard defined by Noll in [68]. The indices of the first ten modes Z_i as well as higher order spherical modes, together with their usual names, are presented in table 2.1.

Zernike polynomials can conveniently represent common aberrations as a single, or a

Index i	Z_n^m	Name	Formula Z_i
1	Z_0^0	Piston	1
2	Z_1^1	Tip	$2\rho\cos(\theta)$
3	Z_1^{-1}	Tilt	$2\rho\sin(\theta)$
4	Z_2^0	Defocus	$\sqrt{3}(2\rho^2-1)$
5	Z_2^{-2}	Oblique Astigmatism	$\sqrt{6}\rho^2\sin(2\theta)$
6	Z_2^2	Vertical Astigmatism	$\sqrt{6}\rho^2\cos(2\theta)$
7	Z_3^{-1}	Vertical coma	$\sqrt{8}(3\rho^3-2\rho)\sin(\theta)$
8	Z_3^1	Horizontal coma	$\sqrt{8}(3\rho^3-2\rho)\cos(\theta)$
9	Z_3^{-3}	Vertical trefoil	$\sqrt{8}\rho^3\sin(3\theta)$
10	Z_3^3	Oblique trefoil	$\sqrt{8}\rho^3\cos(3\theta)$
11	Z_4^0	Primary spherical	$\sqrt{5}(6\rho^4-6\rho^2+1)$
22	Z_6^0	Secondary spherical	$\sqrt{7}(20\rho^6-30\rho^4+12\rho^2-1)$
37	Z_8^0	Tertiary spherical	$3(70\rho^8-140\rho^6+90\rho^4-20\rho^2+1)$

Table 2.1: First eleven Zernike polynomials and higher order spherical modes

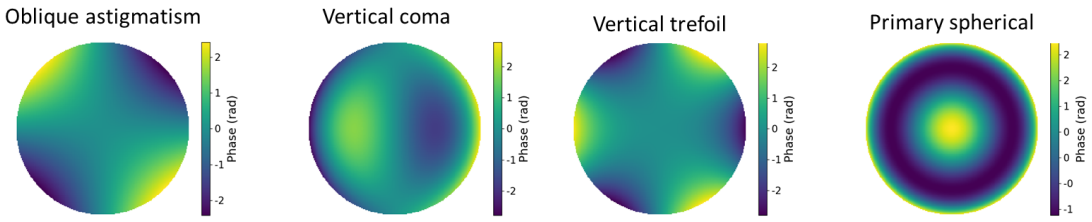

Figure 2.6: Representation of four different Zernike polynomials

sum of a small number of modes. For instance, a lens tilted with respect to its optical axis introduces Zernike coma, a refractive index mismatch induces a combination of Zernike spherical modes and certain optical elements like dichroic filters can induce Zernike astigmatism.

Direct wavefront sensing

Direct wavefront sensing (DWS) consists in measuring the phase of a reference point-like source which theoretical wavefront is known. In astronomy, the reference is chosen

to be a bright single star called the ”guide star”, that in non-aberrating conditions has a flat wavefront. The phase of this reference is measured using a wavefront sensor, typically a Shack-Hartmann. The principle of a Shack-Hartmann wavefront sensor is to measure the local wavefront deformations by dividing the incident beam into sub-regions with a microlens array. Each microlens focusses a part of the incident beam on a camera chip and local wavefront deformations that can be approximated as a linear combination of tip and tilt induce a shift of the focal point. This shift is porportional to the gradient of the wavefront and given this information over different points of the pupil, it is possible to reconstruct the wavefront. DWS was achieved in a widefield fluorescence microscope using fluorescent beads inserted in the sample as guidestars [66, 69], with a shack-hartmann wavefront sensor in a separate color channel. This approach was also used succesfully deployed in a confocal microscope [70]. The need for fluorescent guidestars artificially inserted into the sample however limits the number of fluorescent channels available (as one has to be dedicated to the wavefront sensing) and complicates the sample preparation, especially for living specimens. For these reasons, DWS with a shack-hartmann wavefront sensor was developed using the fluorescence light emitted by the structures of interest [71] or using back-scattered light [72, 73]. Both these approaches required the use of an aperture to reject out-of-focus light, which also act as a low-pass filter and thus reduce the efficiency of the aberration measurement.

For this reason, the most spectacular results obtained with DWS were obtained with multiphoton microscopes, in which the excitation intensity is strong enough to induce two-photon excitation only in the vicinity of the focal plane and thus no pinhole is required to remove out-of-focus light [74, 75]. This approach is limited in scattering samples, where scattered light limits the ability of a shack-hartmann to measure aberrations. This can be compensated by measuring aberrations in smaller areas [75], or by removing scattered

light by means of an interferometer using coherence gating [76, 77].

Phase retrieval

If a point-like object can be imaged but no wavefront sensing device is available, phase retrieval[78] can be used. With phase retrieval, the wavefront of a point-like source is reconstructed from the intensity distribution of its image. It necessitates the acquisition of multiple images aberrated with a user-induced phase variation called phase diversity, to then calculate the phase and intensity distributions that are most likely to produce the observed data. In its original implementation, two images were used, one with no bias applied and the other with defocus. Phase retrieval was used to estimate aberrations in wide-field fluorescence microscopes [79] and found significant applications in SMLM, where by design only single emitters are present within a field of view [80–82]. Other applications include calibration of optical systems [83, 84], where the sparsity of the sample can easily be controlled.

Sensorless adaptive optics

In most cases, in microscopy, a guide star is not available. Aberrations can nevertheless be determined in these circumstances, using sensorless adaptive optics. Sensorless wavefront sensing is an indirect wavefront measurement that relies on the introduction in the systems of given amounts of aberrations and the assessment of their effect on an image quality metric [85–87]. Sensorless adaptive optics thus requires that the wavefront is described as a sum of different modes which can be independently corrected. Zernike polynomials are usually chosen for this purpose, even though different modes like binary masks have been used successfully [88]. For each mode, a series of bias values are introduced, an image quality metric is calculated and the bias that maximises this image

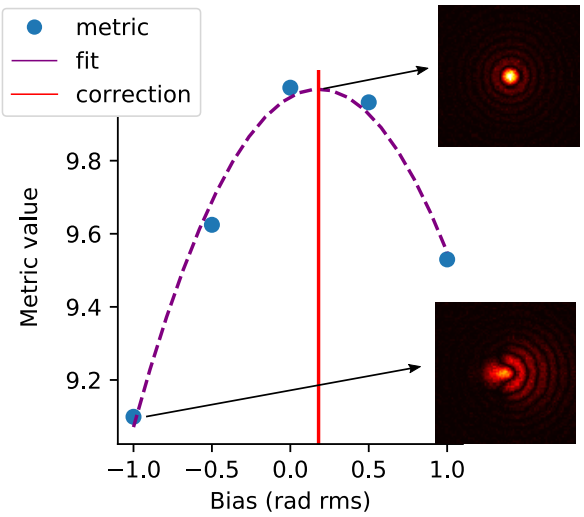

Figure 2.7: Principle of sensorless adaptive optics. A series of predetermined bias aberrations (x axis) are introduced in the system and the corresponding images are acquired (insets). An image quality is calculated for each of them (y axis). Fitting this curve with a quadratic function (purple) allows determination of the position of the extremum (red), which can be defined as the correction.

quality metric is defined as the correction. In practice, the bias vs quality metric curve is usually fitted with a simple function like a parabola to determine the correction with great precision (Figure 2.7). The sensorless method has several advantages when compared with other wavefront sensing methods: it is relatively simple as it does not need a different optical path for wavefront sensing, does not require a guidestar and in general does not necessitate any specific specimen structure. It is also less sensible to scattering than DWS. For these reasons, sensorless adaptive optics has been deployed in a variety of microscopes: confocal [87], two-photon [89] and widefield microscopes [90], as well as super-resolution microscopes like SIM [91, 92], SMLM [93] and STED [94].

2.5.3 AO for FCS

Precise knowledge of the shape and size of the observation volume in FCS is necessary to extract meaningful information from FCS experiments and minor distortions can bias experimental results [95]. Aberration correction is therefore of great value for FCS. Sensorless AO was used to correct aberrations in homogeneous solutions [96] as well as wavefront deformations induced by cells [97] or by tissues [98]. The choice of quality metric, a key sensorless parameter, was extensively studied and it was found that the optimal metric depends on the molecular brightness and concentration of the fluorescent molecules [99].

2.5.4 AO for STED microscopy

STED microscopes are extremely sensitive to optical aberrations and as such AO for STED has attracted considerable attention over the past years. One of the simplest methods of aberration correction consists in simply moving the correction collar of the objective to correct for spherical aberration. This simple approach allowed STED imaging in brain slices at depths larger than 100 µm [100, 101]. A similar approach using a SLM instead of a correction collar to correct spherical aberrations could also successfully improve image quality [42, 102], however at lower depths. In most cases, though, correction of more complex aberrations is necessary. This is particularly challenging as different aberration modes have different effects on the STED depletion pattern. The effects of aberrations on the shapes of depletion patterns [23, 103, 104] as well on the quality of the central intensity minimum of the depletion pattern [25] were investigated using simulations. Simulations and experimental measurements showed that coma aberrations induce lateral shifts of the central intensity minimum of the 2D- and z-STED depletion patterns

in opposite directions [25]. The effect of low-order Zernike modes on the effective STED PSF was also investigated [24]. The effect of phase mask misalignment on the depletion patterns has been both theoretically and experimentally investigated and the similarity between misalignment and coma aberration discussed[105]. It was found that coma and mask misalignment induced similar deformations in the 2D depletion patterns but not in the z-STED depletion pattern.

The first step of AO for STED microscopy consists in removing system aberrations affecting the depletion pattern. Aberrations affecting a ring-shaped focus for 2D-STED could be measured using phase retrieval [84] and later using a machine learning approach [106]. For SLM-based depletion beams, it was found that binary phase masks designed to be sensitive to only one specific Zernike mode could greatly simplify the measurement, and later suppression, of system aberrations [107].

Specimen-induced aberrations are much harder to measure than system aberrations. Most implementations reported so far achieving sample aberration correction used sensorless adaptive optics. In this case, the key component is the image quality metric, which must be able to account for all the potential distortions caused by aberrations to the depletion pattern. In a first implementation, a metric combining image brightness and sharpness was used [94], requiring empirical tuning of several parameters. The setup, including two SLMs, one in the excitation path and one in the depletion path, was used to image fluorescent beads through an aberrating medium. This approach was later adapted to automatically align the excitation and depletion beams of a 2D-STED microscope [108], where Zernike tip and tilt were applied to the depletion pattern and varied to maximise the image quality metric as for any other aberration mode. Using two SLMs in the system allowed correction of aberrations in the excitation and depletion paths, but not in the detection. Full aberration correction of all three beam paths could be achieved using a different opti-

cal system including a DM [109]. Together with a different image quality metric, based on the Fourier ring correlation (FRC), aberrations occuring upon imaging a *Drosophila* brain sample could be corrected.

Instead of directly maximising the quality of the STED image, another approach instead consists in removing the STED phase pattern and use the sensorless approach to maximise total light suppression. In practice, the STED focus is Gaussian during the optimisation process and has a highest peak intensity during the optimisation process leading to a better depletion of fluorescence light. Once the aberration correction process is complete, the STED phase mask can be displayed again. This approach led to image improvements in single cells [110] and in brain tissue [111]. Imaging directly the gaussian shape of the STED focus (with no phase mask on) was also used together with a coherent optical adaptive technique [112] or with a genetic optimisation algorithm [113] to improve the quality of STED images in aberrating samples.

Sensorless AO is the most widely used, but not the only technique for AO STED. Using a two-photon excitation laser, a STED setup including a Shack-Hartmann wavefront sensor was proven capable of correcting aberrations in the brain of a living mouse [114, 115]. This approach allowed simultaneous correction of more than 40 Zernike modes in a living animal, at the price however of a complexity even greater than for setups designed for sensorless AO.

Chapter 3

Set-up of a SLM-based STED microscope

Using a SLM in the depletion beam of a STED system presents several advantages. It allows easy switching between depletion patterns, for either 2D, z-STED or even less common confinement modes [30]. Certain phase masks, like the top-hat phase mask used to create the z-STED depletion pattern, require the tuning of an empirical parameter (the inner radius) which requires a complicated optimisation protocol with a static phase plate but can be straightforwardly addressed with a SLM [42]. Finally, a SLM is an optical element that can be used to correct optical aberrations [94, 102, 109]. For these reasons, SLMs are becoming increasingly common in STED setups, in both bespoke and commercial systems. The great potential of SLM-based STED setups comes however with specific challenges for their alignment and calibration. First, SLMs themselves need to be calibrated [116]. Besides, the usual implementation of STED with a SLM creates the depletion pattern on an off-axis hologram used to physically separate and filter unmodulated light. As a result, moving the position of the depletion pattern on the SLM also moves the position of the depletion laser (unlike in the case of a phase plate, where only the phase and not the position of the depletion laser is affected upon moving the phase plate). Besides, it

was shown that the effects of phase mask misalignments can be easily confused with those of coma aberrations [105]. In systems with a phase plate, this has only a limited importance because only the position of the phase plate can be optimised, but in a SLM-based system both phase mask position and aberrations can be tuned separately. To account for these effects and to maximise the potential of our custom SLM-based setup we developed a step-by-step protocol to calibrate the depletion beam of a SLM-based STED microscope. This protocol was also made available online and *via* Zenodo [117]. In this chapter, we leave out more general considerations like alignment of a confocal microscope or setting up its polarisation. These are addressed thoroughly elsewhere [118].

3.1 Setup

3.1.1 Design considerations

The main choice that one has to face when designing a SLM-based STED microscope is to decide whether the STED laser undergoes a single [94] or two passes [102] on the SLM. While the latter offers the highest possible modularity, enabling multiple combinations between different STED confinement modes, it is also technically more challenging as it requires careful coalignment and conjugation of both pupils on the SLM and adding extra polarisation optics which may create detrimental polarisation aberrations. Besides, since most applications require only one depletion pattern at a time, we opted throughout this thesis to use instead a simpler, single-pass design. The STED setup used throughout this study was located in the NanoImmunology lab, located in the Weatherall Institute of Molecular Medicine (WIMM). The setup was designed, built and maintained by other members of the Eggeling Lab, and this work focusses on the alignment and calibration

of the SLM-based depletion beam. This setup was not only used to develop and use AO methods for STED imaging and spectroscopy, but also on a day-to-day basis by end users. This required the SLM to be placed on a separate optical path that could be easily be bypassed using a polarisation beam splitter (PBS) and half-wave plate (see Figure 3.1). Because of this optical path shared with other users, the microscope had to be realigned before every utilisation. This made it even more important to develop a fast and reliable calibration protocol.

3.1.2 Optical layout

The setup was a custom STED microscope built around a RESOLFT microscope from Abberior instruments (Germany) (Figure 3.1). The system was equipped with a 100×/1.4 oil immersion objective (Olympus UPLSAPO). Depletion was ensured by a pulsed Ti:Sapphire laser (Spectra Physics) with a repetition frequency of 80 MHz and a tunable wavelength, which we set to 755 nm. Laser pulses were stretched using a 40-cm glass rod and a 100-m single-mode fibre. The depletion laser was split between two arms using a PBS, and the amount of light going through each arm was tuned by rotating the direction of the polarisation using a half-wave plate. In the first arm, the phase of the depletion laser was modulated by a vortex phase plate (VPP1a, Rochester Photonics, USA) to create a 2D-STED depletion pattern. This arm was mainly used by other users to bypass the SLM arm, but was also used in combination with the second arm to overlap two different STED depletion patterns (see chapter 7).

The second arm included a SLM (LCOS X10468-02, Hamamatsu, Japan) used to generate the depletion patterns and correct aberrations. An optical delay line (ODL) was used to ensure that depletion laser pulses from both arms arrived at the same time in the focus

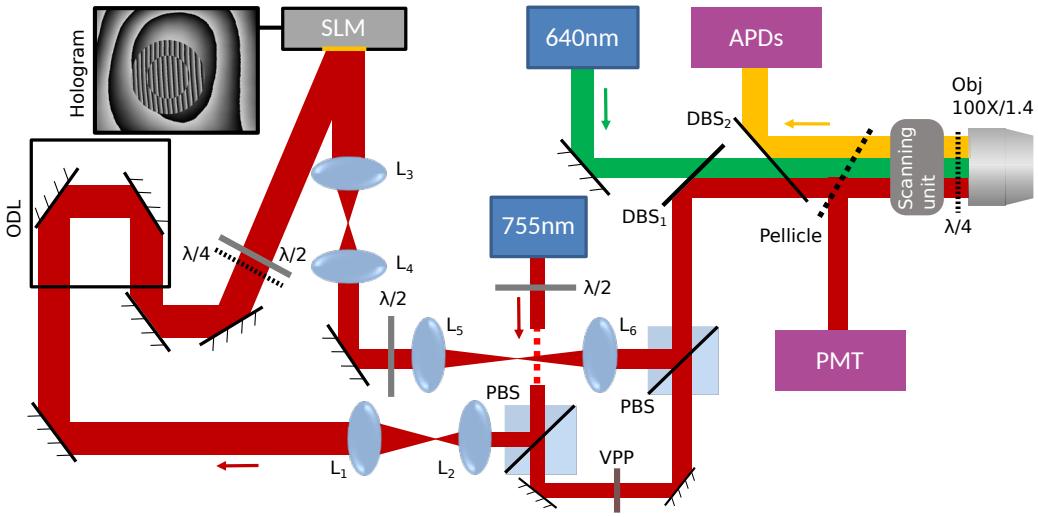

Figure 3.1: SLM-based STED setup used throughout this thesis. It includes 640 nm and 755 nm excitation and depletion lasers (blue boxes), SLM (gray box) and a representative hologram (insert), an optical delay line (ODL), polarisation beam splitters (PBS, blue squares), lenses (L_1-L_6), dichroic beam splitters (DBS_1-DBS_2), quarter- and half-wave plates ($\lambda/4$ and $\lambda/2$), a removable pellicle beamsplitter (dotted black line), APD and PMT (pink boxes).

of the objective, thus enabling the simultaneous use of both depletion paths. The pupil of the SLM was imaged on the back focal plane (BFP) of the objective using a set of relay lenses (Thorlabs, see Table 3.1) and aligned according to the procedure described in section 3.2.1. Excitation was performed by a 640 nm pulsed diode laser (LDH-D-C-640, PicoQuant, Germany) triggered by the STED laser. Detected light was collected back by the objective, filtered by a pinhole of a size of 1 Airy unit and measured using an avalanche photodiode (APD) (Excelitas SPCM-AQRH-13). Direct imaging of the depletion focus was made possible by scanning a sample of scattering gold beads and collecting approximately half of the scattered light with a photomultiplier tube (PMT) using a pellicle beam splitter. The pellicle was removed when imaging fluorescent samples.

Scanning was performed laterally using galvanometric scanners, and axially using a piezo stage (Physik Instrumente) moving the objective lens along the axial direction. Mov-

ing the objective along the optical axis with the piezo stage can cause aberrations and a loss of conjugation if the scanning range is larger than the depth of field of the system of relay lenses used to image the SLM on the BFP of the objective. To estimate this, we calculated the axial resolution of the lens L_6 (Figure 3.1) used to image the BFP of the objective, using equation 2.2 in chapter 2. Given a lens diameter of ½ inch and a focal length of 500 mm (table 3.1), we found an axial focus size of 9.3 mm, much larger than the axial scanning range used throughout this thesis (2-20 µm) and therefore no misconjugation was expected from scanning the objective along the optical axis with a piezo stage.

Lens	L_1	L_2	L_3	L_4	L_5	L_6
f (mm)	40	80	300	35	250	500

Table 3.1: Focal length f of lenses used in the depletion path shown in Figure 3.1

3.2 Alignment and calibration

The SLM was controlled with a Python program developed previously in our lab [119]. To correct for the non-flatness of the back surface of the SLM, every phase pattern generated by the SLM was added to a flatness correction file provided by the manufacturer.

3.2.1 Conjugation between the SLM and back focal plane of the objective

Conjugation between the SLM and the BFP of the objective was particularly important. Indeed, in case of misconjugation, changes in phase lead to a shift of the pupil with respect to the back focal plane of the objective, which in turn lead to unwanted deformations of the focus. This is particularly expected when inducing tip and tilt with the SLM (Figure

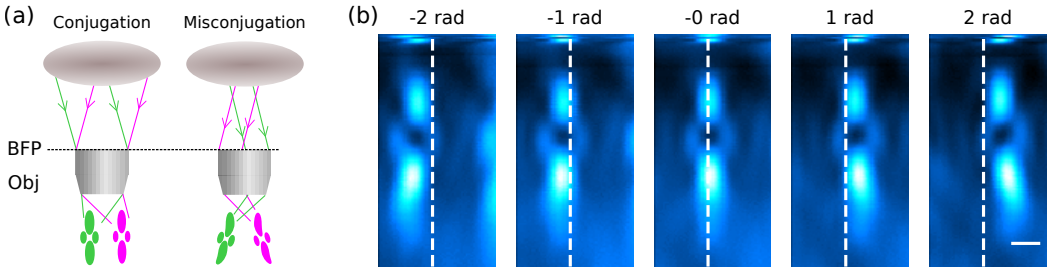

Figure 3.2: Effect of misconjugation between SLM and BFP of the objective. (a) If the SLM and the BFP of the objective (dotted black line) are conjugated (left), different tilt values (green and magenta) change the angle of incidence of the beam in the BFP and shift the focus. In case of misconjugation (right), the angle and the position of the beam in the BFP change, leading to a deformation of the focus. (b) STED depletion pattern imaged with scattering gold beads, in presence of a misconjugation while various amounts of tip were applied. Dashed white lines: position of focus with 0 tilt, scalebar: 500 nm.

3.2(a)).

We used this phenomenon to assess the conjugation in our setup. For this, we inspected the z-STED depletion pattern using a sample of scattering gold beads upon introduction of various amounts of tip with the SLM. Subsequent deformations of the depletion pattern revealed a misconjugation (Figure 3.2(b)). We corrected for this effect by moving one of the intermediary lenses (lens L_5 , see Figure 3.1) until no deformations of the depletion pattern occurred upon introduction of tip or tilt. Another, more common solution to assess conjugation consists in imaging together the back focal plane of the objective and the pupil of the SLM using a relay lens, a beam splitter and a camera. Despite being more direct, this method has the disadvantage of relying on external optical elements which may be hard to insert in the optical path. Besides, the precision of the conjugation obtained with this method depends on the NA of the lens used to image the pupils on the camera, while direct observation of the effects of tilt on the PSF allows conjugation of pupils with the tolerance needed.

3.2.2 Creation of an off-axis hologram

We used a SLM with a high modulation efficiency ($> 90\%$ according to the manufacturer). Despite this excellent modulation efficiency, a fraction of the light incident on the SLM remains unmodulated. Here, we intended to create a ring-shaped pattern with a central intensity minimum (for either 2D or z-STED), the quality of which is critical to STED experiments. In the case of imperfect phase modulation, indeed, the central intensity minimum fills up, and the photons in the centre of the focus are quenched, leading to a loss of signal and resolution. To get rid of this unmodulated light, we created the depletion pattern on an off-axis hologram [120]. A blazed grating was added to the pupil of the SLM, with the effect of shifting all modulated light spatially. Unmodulated light, on the contrary, remained unaffected and could be blocked with a pinhole in the Fourier plane of one of the intermediary telescopes (Figure 3.3, (a)).

3.2.3 Positioning the hologram on the SLM

The strategy to align a conventional, phase-plate based depletion pattern usually consists in first removing the phase plate and aligning the depletion laser as any other beam. The phase plate is then reintroduced in the optical path, and the lateral position of the phase plate is adjusted to ensure an optimum quality of the depletion pattern. In SLM-based STED systems, this procedure is not directly applicable. Because the modulated light is spatially shifted with a blazed grating, moving the phase pattern on the SLM also leads to a shift of the position of the depletion laser. To change only one parameter at a time, it is preferable to settle the position of the hologram on the SLM beforehand, to ensure it is aligned with that of the illumination profile. Several methods can be used for this. A simple one consists in displaying an alignment target exhibiting steep phase steps

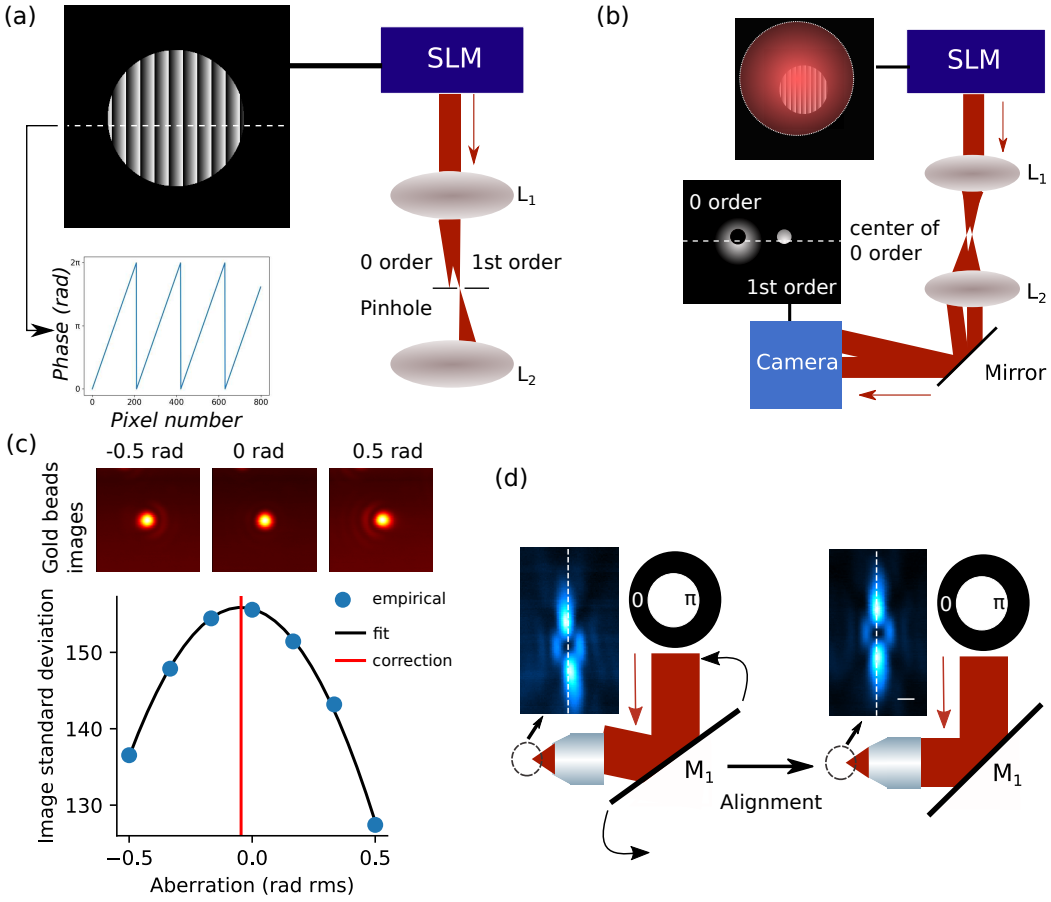

Figure 3.3: Calibration protocol of a SLM-based depletion path. (a) A blazed grating (left) was used to create an off-axis hologram. The unmodulated light was separated in the Fourier plane of a lens (L_1) of an intermediary telescope and was blocked by a pinhole. (b) Positioning the hologram on the SLM. Using a blazed grating displayed on the SLM pupil and a webcam imaging the positions of both 0 and 1^{st} orders . The hologram was centred by aligning 0 and 1^{st} orders. (c) System aberration correction using the sensorless method. Top: Images of scattering gold beads with various amounts of coma introduced by the SLM. The curve of image standard deviation versus applied aberration (bottom, blue circles) was fitted with a quadratic function (black) to determine the optimum correction (red vertical line). (d) Misalignments of the top and bottom lobes of the z-STED depletion pattern along the optical axis (left) reveal lateral misalignment between the pupil of the SLM and the BFP of the objective, which can be corrected by rotating an intermediary mirror M_1 (right)

on the SLM. Phase steps induce light diffraction due to the limited capacity of the SLM to create sharp phase transitions and can thus be imaged on a camera. As an alternative to this method, we compared the relative positions of the modulated and unmodulated laser beams and ensured they were concentric. In practice, we displayed a pupil with a blazed grating smaller than the illumination profile and removed the intermediary pinhole that blocks the 0^{th} diffraction order. Using the chip of a webcam inserted in the optical path, we imaged both diffraction orders (Figure 3.3(b)). Using the position of the 0^{th} order as a reference, we moved the position of the hologram on the SLM to centre the 1^{st} order. The hologram was aligned in two dimensions (x and y), therefore requiring two separate measurements with two orthogonal blazed gratings displayed on the SLM pupil.

3.2.4 Wrap value calibration

Our SLM was controlled on a pixel-wise manner, where each pixel was individually addressed with a digital signal varying between 0 and 255. The relationship between command and output phase modulation was calibrated by the manufacturer to be linear. The exact value of the digital signal needed to induce a phase shift of 2π, even though generally provided by the manufacturer, is wavelength-dependent and is better recalibrated. This value is referred to as wrap value, since phase patterns with an amplitude larger than 2π are wrapped between 0 and the wrap value. We calibrated the wrap value by displaying a blazed grating on the SLM and blocking the 0^{th} order, as described in section 3.2.2. We then measured the intensity in the 1^{st} order for different values of the wrap value. Maximum diffraction efficiency was reached for the wrap value corresponding to a phase modulation of 2π.

3.2.5 System aberration correction

All optical systems contain a certain amount of optical aberrations. If their amplitude is too high, they damage the PSF of the microscope and deteriorate measurement quality, and they must therefore be minimised. In conventional setups, this is achieved by a careful system design and alignment. In the extremely sensitive depletion path of a STED microscope, however, this may not be sufficient and further correction of aberrations with a SLM is beneficial. We therefore developed a method to correct for system aberrations in our system. We used for this the sensorless method: while imaging the Gaussian shape of the depletion focus with no phase mask on and using a sample of scattering gold beads, we introduced known amount of aberrations with the SLM. We used a pixel size typically equal to 30 nm, well below the diffraction limit, and therefore deformations of the depletion focus caused by aberrations were clearly visible (Figure 3.3(c), top). As aberrations were introduced in the system, the size of the focus tended to increase (the signal was spread across more pixels) while the relative intensity of each pixel decreased. Therefore, we found that a good metric to evaluate image quality was image standard deviation, defined as:

$$std = \frac{1}{mn} \sum_{i=1}^{n} \sum_{j=1}^{m} \left(x\left(i,j\right) - \langle x \rangle \right)^2 \tag{3.1}$$

where $x\left(i,j\right)$ are the pixel values of an image defined as an m by n array of pixels and $\langle . \rangle$ refers to the averaging operator. This metric was sensitive to even small changes in aberrations and as expected was maximum when no aberrations were present in the depletion beam (Figure 3.3(c), bottom). Using this metric allowed us to correct system aberrations. The whole procedure was quick (a couple of minutes) and could be performed prior to each experiment if necessary. Predictably, however, system aberrations were stable in time and once initially calibrated, were measured only occasionally.

3.2.6 Ensure coalignment between SLM pupil and objective back aperture

Misalignment between the STED laser and the back aperture of the objective can lead to distortion of the focus (Figure 3.2). In many microscopes, it is sufficient to remove the objective lens and replace it with a system of two pinholes to ensure that the incident laser beam is centred and straight (and adjust it if not). This approach may however not be precise enough to align the depletion pattern of a STED microscope. In the case of the 2D STED depletion pattern, distortions caused by a misalignment between the STED laser and the back aperture of the objective are very similar to those induced by coma aberration [105]. On the contrary, such misalignments have a very specific effect on the z-STED depletion pattern: they induce a tilt of the axis that goes through the centroids of the upper and lower lobes. Precise alignment of the STED laser into the back aperture of the objective can thus be achieved by tilting a mirror in the optical path (away from a Fourier plane) to ensure that the upper and lower lobes of the z-STED depletion pattern are aligned along the optical axis (Figure 3.3(d)).

3.3 Results

3.3.1 Improvement of depletion focus quality

This step-by-step protocol allowed us to improve the quality of the STED depletion pattern (Figure 3.4(a)). We found relatively low aberration amplitudes (in the range of 0.1-0.2 rad rms) spread across multiple aberration modes (Figure 3.4(b)). These small amounts of aberrations alone would not be expected to severely disrupt the performance of z-STED, however in systems which are not carefully calibrated these effects are entangled with

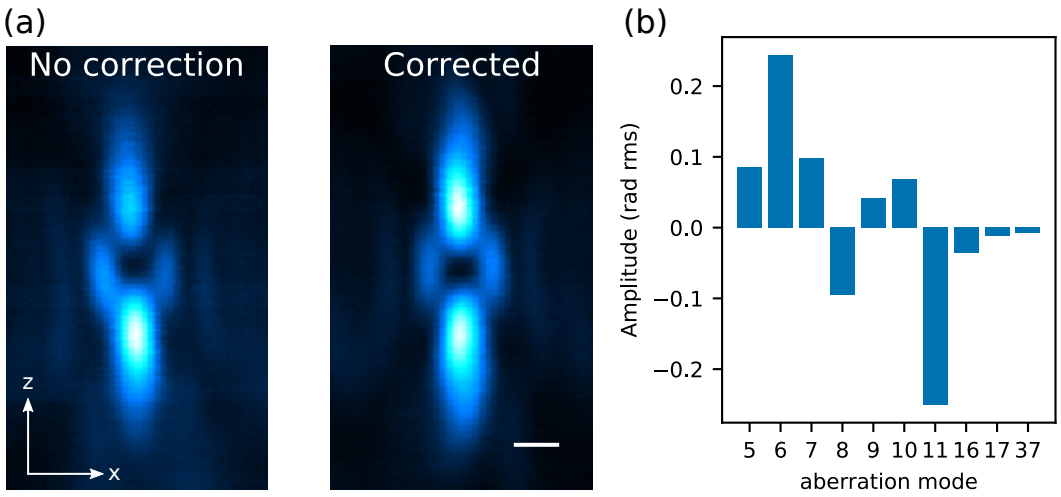

Figure 3.4: Improving depletion pattern quality with calibration. (a) Left: the depletion pattern, imaged by scanning a sample of scattering gold beads, without aberration correction and pupils coalignment (sections 3.2.5 and 3.2.6). Right: depletion pattern imaged with aberration correction. Scalebar: 500 nm. (b) Amplitude of system aberrations, numbered following the convention defined by Noll [68] and recalled in Table 2.1.

other defects caused by imperfect positioning of the hologram on the SLM and coalignment of objective back aperture and image of the SLM pupil, thus leading to a further degraded performance.

3.3.2 2D and z-STED imaging of immobilised fluorescent beads

A major advantage of using a SLM rather than a phase plate in the depletion beam of a STED microscope is, besides aberration correction, the ability to switch phase masks without moving any optical component. Once calibrated, our setup was capable of faithfully creating both z-STED and 2D-STED depletion patterns (Figure 3.5(a)). To verify and illustrate the super-resolution capabilities of our microscope, we imaged a sample of immobilised 40 nm fluorescent beads (Abberior, Germany), in confocal and with both STED confinement modes. Lateral (xy) imaging revealed that as expected, z-STED increased the

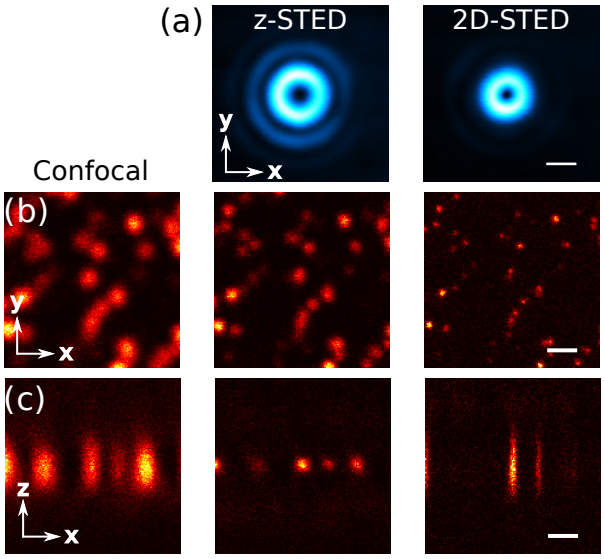

Figure 3.5: STED imaging of fluorescent beads with different confinement modes generated by the SLM. (a) Lateral images of z- (middle) and 2D-STED (right) depletion patterns, imaged using scattering gold beads. (b-c) Lateral (b) and axial (c) images of immobilised fluorescent beads, in confocal (left), z-STED (middle) and 2D-STED (right). STED laser power: 115 mW, Scale bar: 500 nm.

lateral resolution slightly with respect to confocal, while it was massively increased with 2D-STED (Figure 3.5(b)). Axial (xz) imaging on the other hand revealed significant improvements obtained with z-STED, while 2D-STED left axial resolution unchanged. Overall, these results showed that our STED microscope worked as expected. Resolution improvements obtained with the different confinement modes were quantified in chapter 7.

3.3.3 Imaging a biological sample

Finally, we tested the capability of our z-STED microscope to image biological samples. For this, we imaged a sample of fixed cells in which mitochondria were labelled (kindly provided by Dr Silvia Galiani). We acquired three-dimensional image stacks,

both in confocal and z-STED modes. Inspection of single axial slices showed that z-

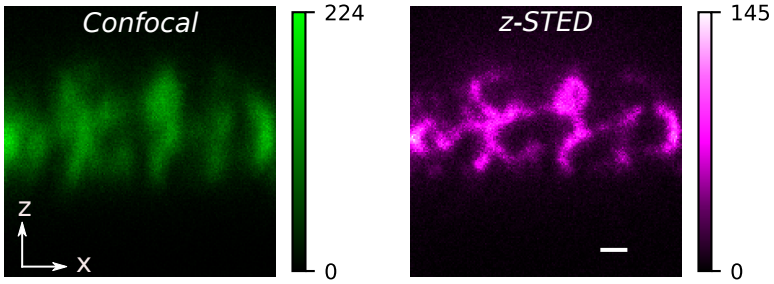

Figure 3.6: Confocal (left) and z-STED (right) imaging of mitochondria in a fixed sample of human fibroblasts. STED laser power: 30 mW, scale bar: 500 nm

STED improved axial resolution significantly (Figure 3.6), revealing details inaccessible to diffraction-limited confocal imaging.

3.4 Discussion

We developed a detailed protocol to calibrate the depletion beam of a STED microscope including a SLM. We developed this protocol specifically for z-STED, but once calibrated we could also use the system in 2D-STED mode. The protocol we developed is iterative, and particularly the last steps (3.2.5 and 3.2.6) needed to be repeated several times in order to reach a stable, optimum alignment. Over the timescale of this project (approximately 2.5 years), we did not observe a significant change in the system aberration correction. On a day-to-day basis, we found that it was only necessary to ensure coalignment between SLM pupil and objective BFP (section 3.2.6). This was expected because another depletion path was used on a daily basis by microscope users, meaning that the optical alignment changed daily. More surprisingly, this alignment step needed occasionally repeating several times a day, as the system frequently drifted. We assumed that this was caused by elasticity in one of the screws used to position mirrors, causing the system to quickly return towards

its previous position after alignment. Another potential source of drift was mechanical expansion and contractions caused by varying temperatures across the day.

Thanks to this calibration protocol, we could obtain an excellent STED performance, especially with the z-STED axial confinement mode. Having shown the applicability of z-STED in fixed biological samples, we then sought to extend the scope of applications of z-STED to physiologically more relevant and more interesting living specimens.

Chapter 4

z-STED imaging and spectroscopy to investigate nanoscale membrane structure and dynamics

One of the main advantages of STED with respect to SMLM is its speed which makes it compatible both with live cells imaging and with a fast spectroscopic technique like FCS. This has made STED microscopy a tool of choice in many fields of biological research and particularly for the study of the plasma membrane. Indeed, the unique spatiotemporal resolution of STED-FCS allows the observation of transient, nanoscale heterogeneities in the plasma membrane (called lipid rafts [121]) which are thought to play crucial roles in membrane protein segregation and function, yet which exact nature, composition and function are still widely unknown. An important drawback of STED microscopy is the high rates of photobleaching which come with the high intensity of the depletion laser. In most specimens, this photobleaching is problematic: it precludes long measurements and limits the maximum achievable signal levels. Photobleaching is however not an issue

when exchangeable fluorophores are used: in this case, bleached fluorophores are quickly replaced with intact ones during the imaging process. This was achieved for STED imaging using DNA-paint fluorophores [49]. Self-replenishing fluorophores happen to be also commonly used in membrane studies, not directly for their replenishing capabilities but because fluorescent lipid analogues are inserted in the plasma membrane and serve as probes for lipids behaviour in the membranes of living cells.

STED is therefore well suited to membrane investigations. However, STED was so far only used with the 2D-STED confinement mode in this context, in order to probe the lateral organisation of the plasma membrane and measurements in systems of closely spaced membranes were prevented by the poor axial resolution of 2D-STED. Thanks to the procedure described in chapter 3, we had at our disposition a well calibrated z-STED microscope with an excellent axial resolution, which we used to perform such measurements. We used z-STED to investigate the axial structure of synthetic and cellular membranes and coupled z-STED with two spectroscopic techniques (FCS and spectral detection coupled with polarity-sensitive dyes) to measure the nanoscale dynamics and organisation of axially close-by membranes which could not be resolved otherwise. We published the results presented in this chapter in an eponymous article [122]. The figures shown in this chapter were adapted from this article.

4.1 Material and Methods

Bead sample: Microscope slides of 40 nm far-red fluorescent beads were purchased from Abberior Instruments (Germany).

Preparation of supported lipid bilayers: Supported lipid bilayers (SLBs) were prepared with a spin-coater [123]. The cover slips were cleaned with piranha solution (3:1 sul-

furic acid and hydrogen peroxide) beforehand. 1 mg/mL DOPC in chloroform/methanol (with 0.01 mol% of Abberior Star Red-labelled phosphatidylethanolamine (PE, Abberior Labels, Germany)) was spin-coated on to a clean coverslip at 3,200 rpm for 30 seconds. The lipid film was rehydrated with SLB buffer (10 mM HEPES and 150 mM NaCl pH 7.4).

Cells and Maintenance and staining: All cells were maintained at 37 °C and 5% CO2. PtK2 Cells were grown in DMEM (Sigma Aldrich) supplemented with 15% FBS (Sigma Aldrich) and 1% L-glutamine (Sigma Aldrich). NIH-3T3 cells were grown in DMEM (Sigma Aldrich) supplemented with 10% FBS (Sigma Aldrich) and 1% L-glutamine (Sigma Aldrich). Red blood cells were obtained from mouse blood. Cells were labelled with the fluorescent lipid Abberior Star Red-PEG-Cholesterol (Abberior Labels, Germany) in phenol-red free L15 medium (Sigma Aldrich) at concentration of 0.2 µg/mL for 3-5 min at room temperature. After washing twice with L15, measurements were performed also in L15 medium at room temperature. Each slide was imaged not longer than 30 minutes.

Imaging parameters. We used the microscope described in chapter 3. Excitation power was typically set to 15 µW and STED laser power was set to 110 mW unless specified otherwise. Both were measured in the back focal plane of the objective. Polarity-sensitive dyes for spectral imaging were excited with a 485 nm pulsed diode laser (PicoQuant). Images were acquired with a pixel size of typically 40 nm in the lateral direction and 20 nm in the axial direction and were later resized using python or ImageJ. Pixel dwell times varied between 40 and 160 µs.

FCS measurements and fitting: The STED microscope was equipped with a hardware correlator from correlator.com (Flex02-08D) operated by the Flex software. Abberior Star Red dyes were excited with a 640 nm laser at an excitation power of 2-5 µW. The excitation beam was focussed on membranes by varying its axial position to maximise the signal. In cells, acquisition time of FCS curves was set to 5 seconds to limit the im-

pact of membrane motion through the observation focus. The resulting signal levels were sufficient to obtain good FCS curves. This was not a problem in SLBs, where acquisition times were set to 10 seconds. FCS curves were fitted using a custom python script. The observation area (defined as the area in which fluorophores emit light contributing to the correlating signal) was assumed to be Gaussian. A 2D diffusion model including a triplet state was used to fit the data [124].

$$G(\tau) = \frac{1}{N}\left(1 + \frac{T}{1-T}e^{-\tau/\tau_T}\right)\frac{1}{1+\tau/\tau_{xy}} \tag{4.1}$$

Where N is the average number of molecules in the observation area, T is the average triplet amplitude, τ_T is the triplet correlation time set to 5 µs, τ_{xy} is the average lateral transit time in the observation area. Diffusion coefficients (D) were determined from FCS transit times [52]:

$$D = \frac{\omega^2}{8\log(2)\,\tau} \tag{4.2}$$

Where ω is the full width at half maximum (FWHM) of the Gaussian observation area and τ is the average molecular transit time in the observation area determined with FCS. The FWHM of the confocal observation area was determined from images of immobilized fluorescent beads and set to 240 nm. To reliably compare FCS measurements obtained with confocal and STED, we estimated the increase in lateral STED resolution with FCS using supported lipid bilayers (SLBs). Assuming free diffusion, the same diffusion coefficient is expected in both STED (D_s) and confocal (D_c):

$$D_s = D_c \tag{4.3}$$

Given equations 4.2 and 4.3, the Gaussian lateral FWHM ws of the STED focus can be estimated as:

$$\omega_s = \omega_c\sqrt{\frac{\tau_s}{\tau_c}} \tag{4.4}$$

Average number of molecules in the observation area N determined from fitting of individual FCS curves were divided by the measured size of the observation area, to fairly compare confocal and STED recordings. Finally, number of molecules in the observation area were normalised with the confocal value:

$$N_{norm} = \frac{N/\omega}{N_c/\omega_c} \tag{4.5}$$

In SLBs, N_c was set to the average value of all confocal recordings. In cells, average number of molecules were normalized separately in each cell to account for variations in label concentrations between different cells.

Spectral Imaging: We stained the cells with 0.5 µM NR12S in L15 media for 5 minutes at room temperature. Then the cells were washed twice. Imaging was performed in L15 media at room temperature. Each slide was imaged not longer than 30 minutes. The green channel signal was filtered with a 510-590 nm filter (IG) and red channel with a 650-730 nm filter (IR). Images were analysed with the Fiji general polarization (GP) plugin using the equation 4.6 [125].

$$\frac{I_G - I_R}{I_G + I_R} \tag{4.6}$$

4.2 Results

4.2.1 z-STED imaging of supported lipid bilayers

We first assessed the feasibility and performance of membrane studies with z-STED by imaging an SLB. An SLB is a simple membrane model commonly used in lipids studies, made of a double layer of lipids on a glass substrate (Figure 4.1(a)). This membrane was approximately 5-8 nm thick, which was well below the expected axial resolution of

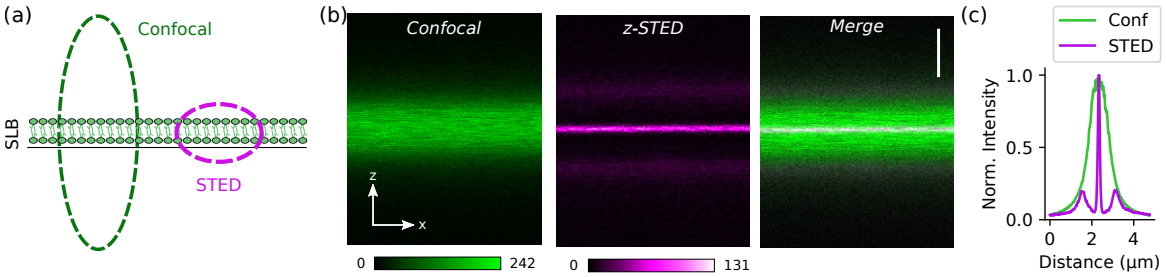

Figure 4.1: z-STED imaging of supported lipid bilayers (SLB). (a) Scheme of the experiment: an SLB is imaged with different modalities, in confocal (left) and z-STED (right). (b) Experimental axial images of SLBs, imaged with confocal (left), z-STED (middle) and merged (right). (c): Axial intensity profiles of the images shown in (b). Scale bar: 1 µm.

the z-STED microscope and was therefore an excellent sample to estimate the axial resolution. Fluorescent lipid analogues (fluorescent molecules with a similar structure as lipids, exhibiting a hydrophilic head and a hydrophobic tail) were incorporated in the SLB mix, effectively allowing fluorescent imaging of the membrane. Comparing SLB images in confocal and z-STED showed a large resolution improvement (Figure 4.1(b)). This was confirmed by axial intensity profiles (Figure 4.1(c)), which exhibited a FWHM of approximately 900 nm for confocal and 110 nm for z-STED. Confocal profiles were larger than expected from a confocal microscope with a 1.4 NA, which could be explained by aberrations remaining in the excitation path of the microscope leading to distortions to the PSF. When imaging an extended object like an SLB, this led to an increase of the apparent axial size of the image. In z-STED, analysis of axial intensity profiles showed sidelobes located at a distance of +/- 800 nm of the focus. These sidelobes were caused by undepleted fluorescence light in areas of poor overlap between the excitation and depletion pattern.

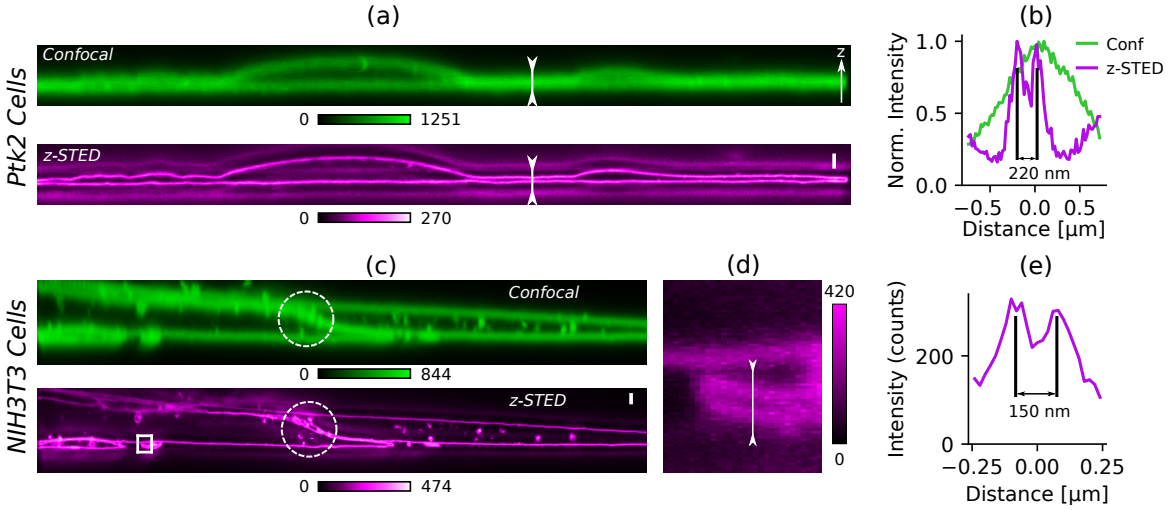

Figure 4.2: Resolving axially close-by membranes with z-STED. (a) Confocal (top) and z-STED (bottom) axial images of a Ptk2 cell. (b) Intensity profiles along the lines drawn in panel (a). (c) Confocal (top) and z-STED (bottom) images of NIH3T3 cells on top of each other. z-STED revealed gaps between layers of membranes (white circle). (d) Zoom on the rectangular area highlighted in (c) and (e) line profile along the line drawn in (e). Scale bars are 1 µm and oriented along the optical axis (z direction).

4.2.2 Resolving adjacent membranes with z-STED

Having demonstrated the capability of our microscope to image lipid bilayers, we tested its capability to resolve axially close-by membranes.

Axially close-by membranes are commonly found in biological specimens, a typical example being the bottom and top membranes of cells. In certain cell types, like Ptk2 cells, they are separated by a distance less than the diffraction limit and could therefore not be individually resolved with a confocal microscope. z-STED on the other hand allowed a clear visualisation of each membrane (Figure 4.2(a)), at distances as close as 220 nm along the optical axis(Figure 4.2(b)). To verify the capability of our technique to image different cell types and topologies, we also imaged NIH3T3 cells. Cells were grown on top of each other and the point of contact between membranes could be visualised as areas of higher

intensity but their exact structures could not be determined. This was made possible by z-STED, which revealed among other things gaps between the two membranes (Figure 4.2(c)). Structures separated by distances as small as 150 nm could be unambiguously resolved (Figure 4.2(d-e)), thus setting a higher bound to the axial resolution.

4.2.3 Impact of undepleted sidelobes on imaging

Undepleted sidelobes observed on SLBs (Figure 4.1) were also observed when imaging cells (Figure 4.2). Because these sidelobes were located far from the actual signal and because their relative intensity was much smaller than that of the signal, they did not cause any ambiguities in image interpretation. In certain applications however, for instance in dense specimens, these sidelobes could significantly decrease image quality and they would be better removed, for instance via image deconvolution.

We therefore developed a deconvolution method specific to z-STED. To do this, we first estimated the shape of the z-STED PSF at the STED laser power we used throughout this chapter (110 mW). The z-STED axial intensity profile was measured using a flat SLB sample (Figure 4.1(c)), while its lateral intensity profile was approximated as a Gaussian with a FWHM of 150 nm, as measured using immobilised fluorescent beads. We approximated the z-STED PSF as a convolution between these two axial and lateral intensity profiles, disregarding fine spatial variations in the intensity of the undepleted sidelobes (Figure 4.3(a)). This approximation was good enough to deconvolve images laterally homogeneous with the Richardson-Lucy algorithm (Figure 4.3(b)) but could be refined in denser, more heterogeneous samples if necessary. As expected, the deconvolution process further increased the image contrast and efficiently reduced the intensity of undepleted sidelobes (Figure 4.3(c)). Used in a sample with a more complex structure, our deconvolu-

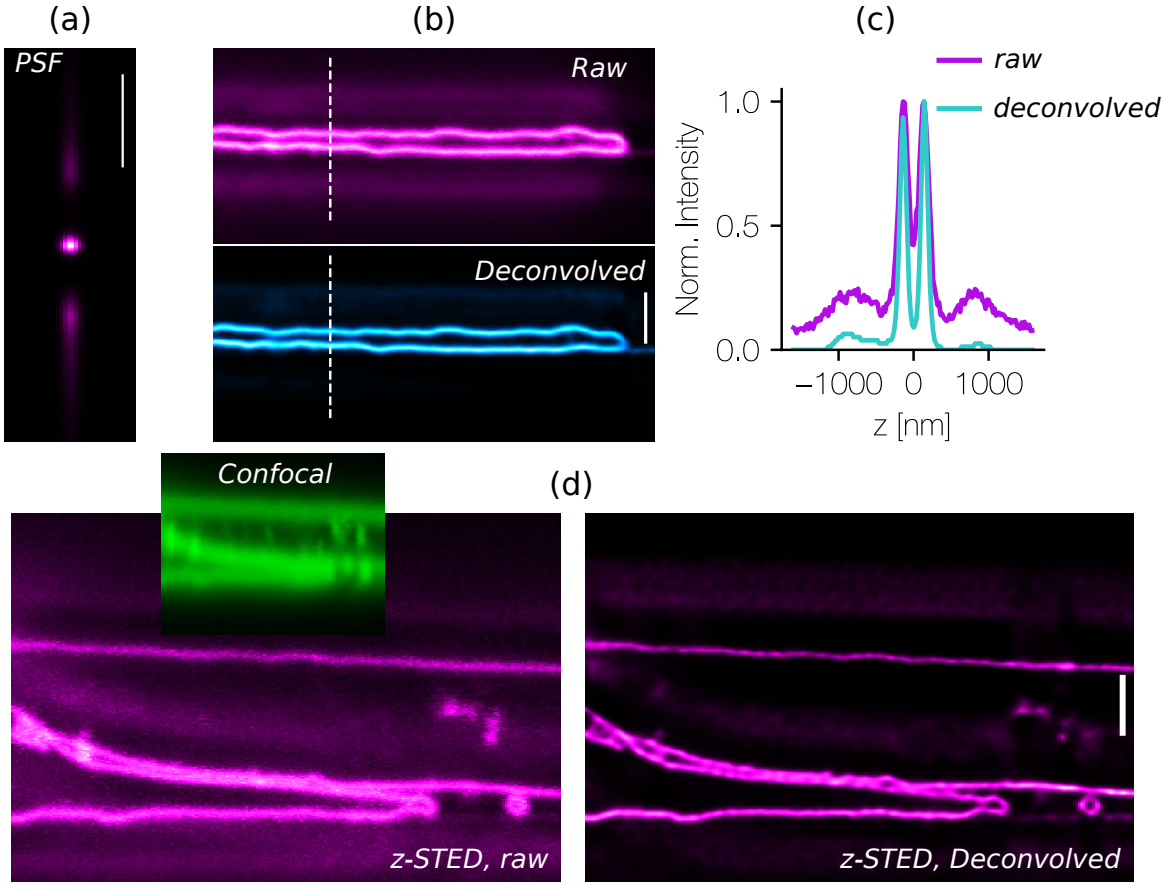

Figure 4.3: Attenuation of undepleted sidelobes in z-STED imaging using deconvolution. (a) PSF estimated from images of SLBs and of fluorescent beads. (b) Deconvolution of a z-STED image of Ptk2 cells membranes using the Richardson-Lucy algorithm and the PSF estimated in (a). (c) Axial intensity profiles along the line in (b), without (magenta) and with (cyan) deconvolution. (d) Axial images of NIH3T3 cells, in confocal (green, inset), raw z-STED (left) and deconvolved z-STED (right). Scale bars: 1 µm, oriented along the axial direction.

tion algorithm performed equally well and significantly improved image contrast (Figure 4.3(d)).

4.2.4 Resolving submicron structures with z-STED

Submicron structures with all sorts of topologies are commonplace in biology and fulfil many different roles. For instance, submicron-sized tubes were found to be critical for cellular communications [126]. These structures can however not be studied with conventional microscopes due to an insufficient spatial resolution. We explored here the opportunities offered by z-STED to image such structures. As a first example, we imaged a SLB which exhibited locally multiple lipid layers, revealed in confocal by a higher fluorescence intensity (Figure 4.4(a)). The conformation of such multiple layers on its edge was unclear, as repulsion between the hydrophobic lipid tails and the aqueous environment would make a straight border energetically disadvantageous. No specific conformation could be observed in confocal, while z-STED imaging revealed that the tubes were formed at the border of patches to reduce the hydrophobic repulsion. In networks of smaller patches, z-STED revealed tubes to be the dominant structures (Figure 4.4(b)). To easily grasp the extent and structure of tubular networks in SLBs, we acquired lateral (xy) images (Figure 4.4(c)). The hollowness of tubular structures could not be determined from confocal or 2D-STED images because of out-of-focus light from the top and bottom of the tubes, while z-STED suppressed these out-of-focus contributions effectively and largely increased image contrast (Figure 4.4(d)). Similarly, imaging red blood cells with a toroidal shape, we found that image contrast was deteriorated by out-of-focus light from the top and bottom membranes when imaging with confocal and 2D-STED, while contrast was maximised with z-STED (Figure 4.4(e-f)). Finally, we investigated the possibility offered

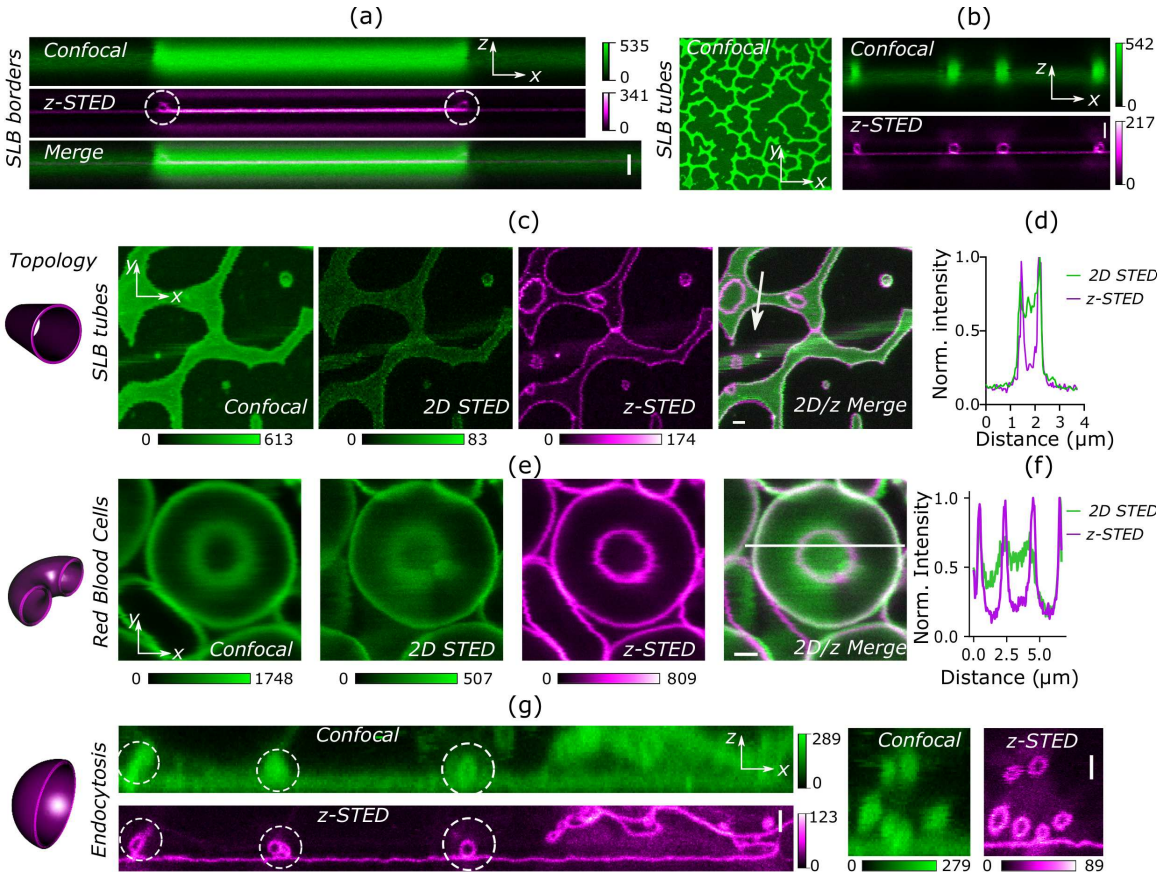

Figure 4.4: Imaging submicron membrane structures with z-STED. (a-b) Tubular structures in SLB patches: (a) Confocal (top, green), z-STED (middle, magenta) and merged (bottom) xz images of a multilayer structure with tubes at its edges (white circles). (b) Left: lateral (xy) confocal images of a network of SLB patches. Right: confocal (top, green) and z-STED (bottom, magenta) axial images of networks of SLB patches. (c-d) Lateral images of membrane tubes in SLBs: (c) From left to right: confocal, 2D, z-STED and 2D/z-STED merged images of SLB patches and (d) intensity profiles along the line shown in (c). (e-f) Lateral imaging of red blood cells with a toroidal shape: (e) confocal, 2D, z-STED and merged images and (f) intensity profiles along the line shown in panel (e). (g) Confocal and z-STED axial images of early endocytic vesicles (white circles). Scalebars are 1 μm. SLBs are labelled with Abberior Star Red-PE, cells are labelled with Abberior Star Red-cholesterol.

by z-STED to image spherical topologies which are ubiquitous in cells. Endocytic vesicles are a characteristic and important example of such topologies, which ensure a significant part of cellular trafficking. Early endocytic vesicles were smaller than the diffraction limit and could not be resolved in confocal, while z-STED allowed fine observation of their structure (Figure 4.4(g)).

4.2.5 Volumetric imaging with z-STED

Axial (xz) images can reveal a wealth of information, but can not fully describe a three-dimensional specimen and volumetric imaging is a must in many applications. To demonstrate the capability of our z-STED microscope to perform volumetric imaging, we imaged a SLB patch similar to those observed in section 4.2.4. Volumetric measurement offered an image quality comparable to that of axial imaging (Figure 4.5(a)) and allowed to finely reveal the structure of the patch. To facilitate visualisation of the structure, we performed a three-dimensional image reconstruction using the software Napari [127]. Median filtering was used to reduce noise, yet undepleted sidelobes and perhaps a structure moving above the SLB patch slightly distorted the final reconstruction. This did not fundamentally prevent the image reconstruction, and could be improved using further image processing (for instance deconvolution) if necessary. To further demonstrate the capability of our system to image living specimens, we acquired a 3D stack of a red blood cell (Figure 4.5(b)). The acquisition time of this stack was of approximately 2 mins ($125\times125\times160$ pixels, with a pixel dwell time of 40 µs) and was sufficiently fast to allow measurement without noticeable motion blur. Acquisition time could be further reduced if necessary by reducing the field of view or decreasing the pixel dwell time.

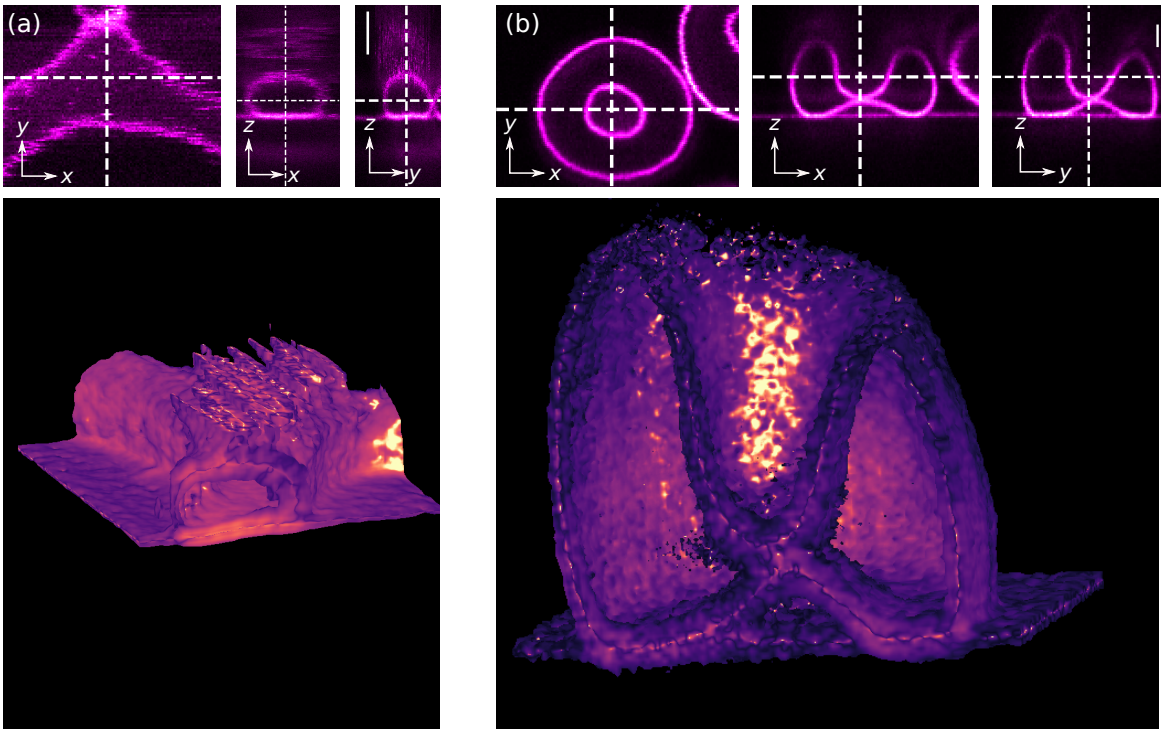

Figure 4.5: Volumetric imaging of a SLB and of a red blood cell using z-STED. Top: Slices of the image volume at the positions marked by the dotted white lines of (a) a SLB patch and (b) a red blood cell. Scale bars: 1 µm. Bottom: three-dimensional image reconstruction.

4.2.6 Monitoring membrane motion with z-STED

Motion can be induced in living cells by multiple factors: endocytic vesicles entering and leaving the cell, cells changing shape in response to external stimuli, or simply cellular movement. It is therefore interesting to acquire timelapses to capture this dynamic information. We demonstrated the capability of our system to gain such information by performing timelapses of axial images of Ptk2 cells imaged with z-STED (Figure 4.6(a-b)). Confocal and STED microscopes are point-scanning microscopes, for which the framerate depends on the number of pixels acquired and on the pixel dwell time. Early experiments revealed a quite slow membrane motion, therefore we preferred the acquisition of a large number of pixels per frame (30000 pixels, imaging a 10$\times$ 3 µm area) with a long pixel dwell

time (100 µs), leading to high signal values, over a high framerate.

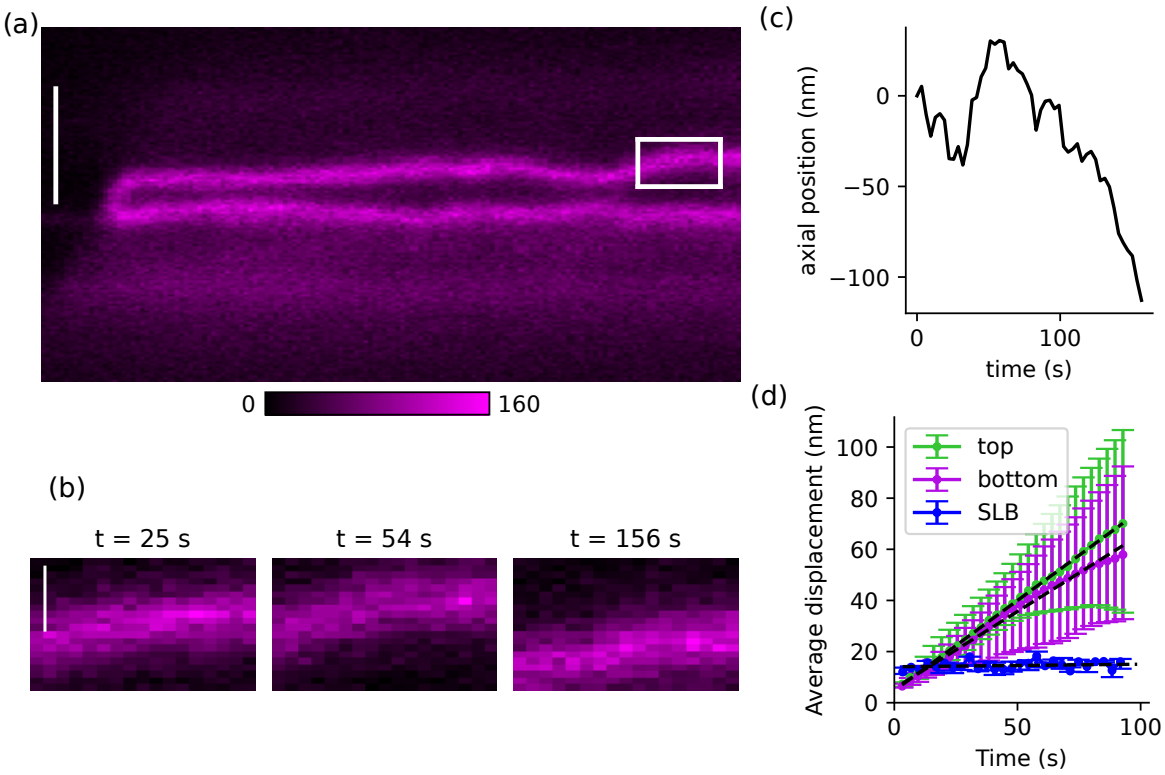

Figure 4.6: Measuring membrane motion with z-STED. (a) Representative frame of a movie of moving membranes in a Ptk2 cell. Scale bar: 1 µm, oriented along the optical axis. (b) Zoom on the area highlighted in (a) at different timepoints. Scale bar: 200 nm (c) Time-dependent position of the membrane shown in (b). (d) Average displacement of top and bottom membranes of cells as well as of SLBs as indicated in the legend, as well as linear fits to these displacements (dotted black lines). Median +/- interquartile range, n=18 points in 6 cells and n=3 points in one SLB. STED laser power: 50 mW.

With these imaging settings, we acquired a series of timelapses (50 frames, 1 frame every 3.2 s) in 6 different cells. In each movie, the membrane position was measured across time at three different positions in the top and bottom membrane. Membrane position was determined by first manually selecting the approximate membrane position and then fitting a Gaussian to the corresponding axial intensity profile to determine its maximum. An exemplary axial trajectory of a cellular membrane can be found in Figure 4.6(c). In order

to quantify membrane motion, we calculated the average displacement as a function of time for each manually labelled membrane position (Figure 4.6(d)). We found that the top and bottom membranes were moving at comparable speed, with the bottom membrane being slightly slower than the top one. As a a non motile control specimen, we acquired a similar timelapse of a SLB, which exhibited little to no motion as expected. To quantify this membrane motion, we used a linear regression to determine the average membrane displacement as a function of time. We found an average displacement 0.7 nm/s for the top membrane, 0.6 nm/s for the bottom membrane and 0.01 nm/s for the SLB. Using this measure of the average membrane displacement speed in the Ptk2 cells we used, we could estimate the importance of axial motion blur in the membrane pictures we acquired previously. With acquisition times in the order of magnitude of 3 s per picture, average motion blur amounts to approximately 2 nm, much smaller than the axial PSF size (approximated to 100 nm from SLB measurements).

4.2.7 z-STED with fluorescence correlation spectroscopy to investigate membrane dynamics

In the previous section, we used the excellent axial resolution of z-STED to investigate the membrane macrostructure, but did not gain any information about the molecular, nanoscale properties of the membrane. Such information can be gained with FCS to measure both molecular diffusion speeds and molecular concentrations, revealing substantial information about the underlying molecular composition and interactions. FCS was successfully combined with STED [56, 128] to measure diffusion speed with a nanoscale precision, but essentially with 2D-STED. In cells with closely spaced membranes, this involved measuring diffusion in two membranes at once, assuming identical diffusion properties

in the top and bottom membranes [58]. However, diffusion hindrances could occur in one or the other membrane, caused for instance by interaction between the plasma membrane and the glass coverslip. To verify this, we used z-STED and its capability to resolve closely spaced membranes to perform STED-FCS measurements in the top and bottom membranes of Ptk2 cells which cannot be resolved with a confocal microscope (Figure 4.2(a)).

Theoretical considerations

We first calculated the expected outcomes of (STED-)FCS measurements in a system of two axially close-by membranes such as the top and bottom membranes of Ptk2 cells (Figure 4.2). We compared the results expected when doing FCS in the top and bottom membranes separately with z-STED with the results expected from confocal FCS experiments on both membranes at the same time. We made for this three assumptions:

1. The intensity fluctuations in the top and bottom membranes are statistically independent.

2. The top and bottom membranes are close enough so that the confocal cross section is identical at both positions.

3. The label concentration and diffusion speed of the top and bottom membranes are strictly identical.

Following these assumptions, the time-dependent intensity recorded in confocal mode by the detector can be written as:

$$I(t) = I_t(t) + I_b(t) \tag{4.7}$$

Where $I(t)$ is the time-dependent intensity recorded by the detector, $I_t(t)$ is the intensity emitted at the top membrane and $I_b(t)$ the intensity emitted at the bottom membrane. The autocorrelation function of the time trace fluctuations writes as:

$$G(\tau) = \frac{\langle \delta I(t)\, \delta I(t+\tau) \rangle}{\langle I(t) \rangle^2} \tag{4.8}$$

where $\langle . \rangle$ denotes the time-averaging operator and $\delta I(t) = I(t) - \langle I(t) \rangle$ represents the temporal intensity fluctuations. Replacing equation 4.7 in equation 4.8 and expanding yields:

$$G(\tau) = \frac{\langle \delta I_b(t)\, \delta I_b(t+\tau) \rangle + \langle \delta I_t(t)\, \delta I_t(t+\tau) \rangle + \langle \delta I_b(t)\, \delta I_t(t+\tau) \rangle + \langle \delta I_t(t)\, \delta I_b(t+\tau) \rangle}{\langle I_t(t) \rangle^2 + \langle I_b(t) \rangle^2 + 2 \langle I_b(t) \rangle \langle I_t(t) \rangle} \tag{4.9}$$

This expression can be greatly simplified using our above assumption. Independence of the fluctuations in the top and bottom membranes (assumption 1) involves that $\langle \delta I_b(t)\, \delta I_t(t+\tau) \rangle = \langle \delta I_t(t)\, \delta I_b(t+\tau) \rangle = 0$. Assumptions 2 and 3 state that the average intensities and intensities fluctuations are identical in top and bottom membranes and we can conclude that $\langle I_t(t) \rangle^2 = \langle I_b(t) \rangle^2$ and $\langle \delta I_b(t)\, \delta I_b(t+\tau) \rangle = \langle \delta I_t(t)\, \delta I_t(t+\tau) \rangle$. As such, equation 4.9 can be simplified as:

$$G(\tau) = \frac{2 \langle \delta I_t(t)\, \delta I_t(t+\tau) \rangle}{4 \langle I_t(t) \rangle^2} = \frac{1}{2} G_t(\tau) \tag{4.10}$$

Where $G_t(\tau)$ is the autocorrelation function obtained if only the top (or bottom) membrane was present. Equation 4.10 thus means that FCS measurements performed on two axially close-by membranes leaves the transit times (and consequently apparent diffusion coefficient) unchanged, but divides the amplitude by a factor two. Consequently, the apparent number of fluorescent molecules is twice higher when measuring two membranes at once than when measuring membranes separately.

Experimental results

We then verified the theoretical predictions in SLBs and Ptk2 cells. We first calibrated our z-STED-FCS measurements on a simple SLB system with confocal and z-STED (Figure 4.7(a-b)). We performed (STED-)FCS measurements and measured the lateral transit time (τ_{xy}) and apparent number of molecules in the observation area (N). From the decrease in lateral transit times (Figure 4.7(c)), we could estimate the size of the observation surface obtained with STED, as explained in the Methods section (equation 4.4). The approximately two-fold reduction in lateral transit time obtained with z-STED was perfectly in line with the 30% increase in lateral resolution readily observed with images of fluorescent beads. Given the size of observation surface and average molecular transit times, we could calculate the diffusion coefficient (Figure 4.7(d)), which we set to the same value to determine the size of observation surface (equations 4.3 and 4.4). Measuring N from the amplitude of FCS curves and knowing the size of observation areas in STED and confocal, we could calculate the number of molecules per surface unit normalised with confocal N_{norm} as shown in equation 4.5 (Figure 4.7(e)). The normalised number of molecules was slightly larger with z-STED, which we attributed to an increase in uncorrelated background in z-STED (caused for instance by residual scattered light from the STED laser collected by the detector) that damped the amplitude of z-STED FCS curves [95]. We then performed measurements in living Ptk2 cells. We used the excellent axial resolution of z-STED to perform STED-FCS measurements in the top and bottom membranes, while confocal measurements were performed in both membranes at the same time (Figure 4.7(f-g)). We limited FCS acquisition time to 5s, to limit the effects of membrane motion. Indeed, we measured a membrane speed of approximately 0.7 nm/s in section 4.2.6, corresponding to an expected 3.5 nm shift (much smaller than the 110 nm axial size of the z-STED PSF)

for a 5 s acquisition time. Longer measurements implied proportionally higher membrane movement values, which combined with an inevitable delay between the positioning of the focus and the start of the acquisition made such acquisitions excessively complicated. Diffusion coefficients calculated from the lateral transit times and calibrated with the data acquired in SLBs were similar for both top and bottom membranes measured with z-STED, as well as in confocal. No measurable diffusion hindrance was caused by interactions with the coverslip. However, the normalised number of molecules per observation surface was twice larger in confocal as it was in both top and bottom membranes as measured with z-STED, as predicted analytically for a system of two identical membranes.

4.2.8 z-STED combined with spectral imaging to investigate membrane structure

FCS measurements gave valuable information about the nanoscale lipid environment of the plasma membrane. This information can be complemented by estimating relative changes in membrane fluidity, a critical parameter for instance for modulation of receptor-ligand interaction [129]. Membrane fluidity can be assessed using polarity-sensitive lipophilic dyes [125], the emission spectrum of which changes with the hydration level of the membrane. This hydration level is linked with lipid packing, with lower hydration levels being associated with higher molecular order. Recently, it was shown that the lipophilic NR12S dye [130] was compatible with STED imaging [131] to gain super-resolved information about membrane fluidity. Here, we sought to use this dye with z-STED. For this, we labelled Ptk2 cells with NR12S and used two-color detection to detect changes in emission spectrum. A green (510-590 nm) and red detection channel (650-730 nm) were used, with fluorescence intensity from more ordered membrane environments

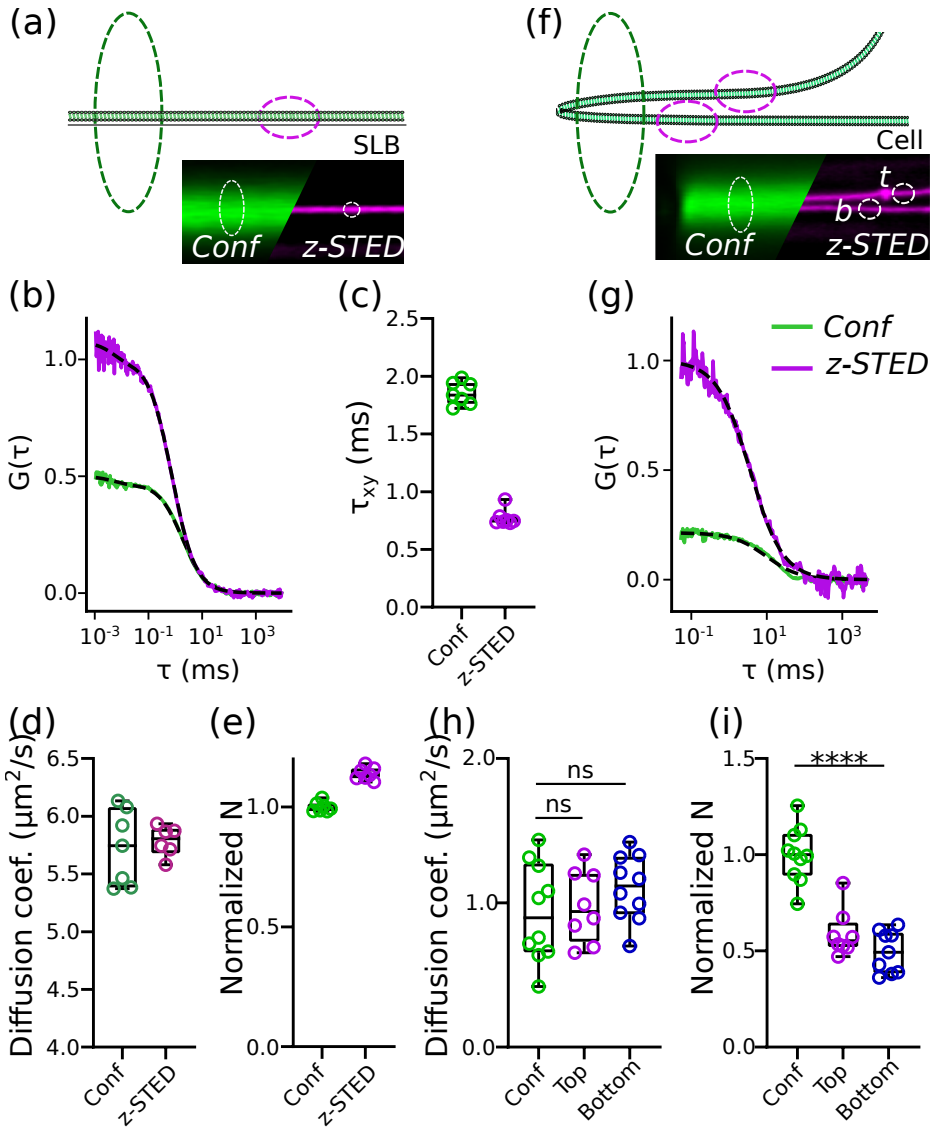

Figure 4.7: z-STED-FCS measurements in membranes. (a-e) FCS measurements in an SLB. (a) Illustration of the experiment: confocal (dotted green ellipsoid) and z-STED-FCS (dotted magenta ellipsoid) measurements were performed on an SLB (lipid bilayer, green). Bottom right: confocal and z-STED pictures of an SLB. (b-e) FCS curves (b), average molecular transit times in the observation surface (c), diffusion coefficients (d) and number of molecules in the observation area normalised with confocal value (e) measured in SLBs, in confocal and z-STED. (f-i) FCS measurements in living cells. (f) Illustration of confocal and z-STED-FCS experiments in axially close-by membranes in cells. (g) z-STED and confocal FCS curves measured in cells. (h) Diffusion coefficient and (i) number of molecules normalized with observation area measured with z-STED in the top and bottom of the cells, measured with confocal FCS in both membranes.

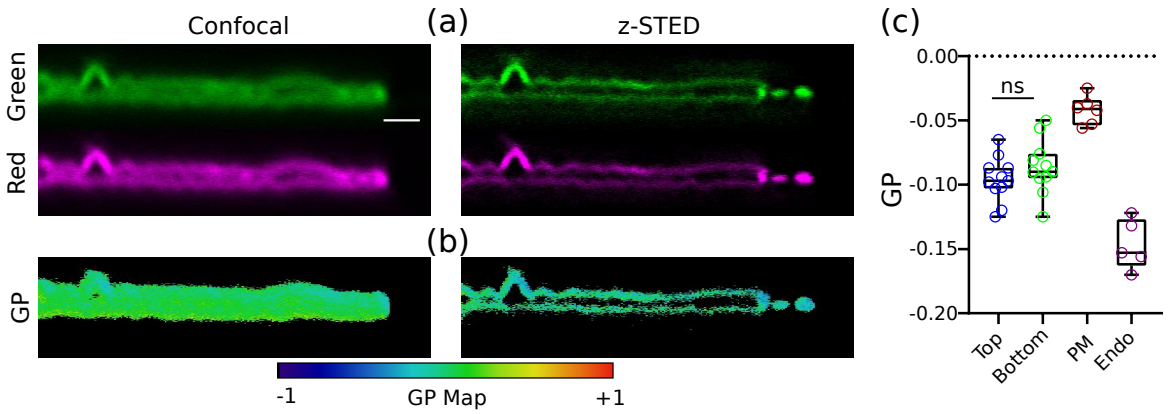

Figure 4.8: z-STED measurements of lipid order on PtK2 cells using the polarity-sensitive dye NR12S and spectral analysis. (a) Confocal (left) and z-STED (right) images of the green (top) and red (bottom) channels used to image a Ptk2 cell labelled with NR12S. (b) General polarization (GP) calculated from the green and red channels of panel (a) using equation 4.6. (c) Average GP measured in cells, in the top and bottom membranes, in the whole plasma membrane and in endocytic vesicles. Early endocytic vesicles were not included in whole plasma measurements. Each data point represents measurement in one cell. Scale bar: 1 µm.

increasing the relative intensity collected in the green channel. To quantify lipid ordering using this information, we calculated the general polarisation (GP), as described in the methods section (equation 4.6). We found that z-STED improved the resolution significantly, allowing separation of closely spaced membranes and distinct measurements of GP in top and bottom membranes which were impossible in confocal only (Figure 4.8(a-b)). A quantitative analysis of GP across multiple cells revealed no differences in fluidity between top and bottom membranes (Figure 4.8(c)), confirming the results obtained with STED-FCS in the previous section. We found however minute differences between the GP of the plasma membrane as a whole and that of endocytic vesicles, suggesting the existence of slightly different lipids compositions.

4.3 Conclusion

We showed that z-STED can be efficiently used in membrane investigations. With STED imaging, we could resolve membranes that were not possible to resolve otherwise, such as the top and bottom membranes of Ptk2 cells. z-STED revealed the precise shape of membranes with different topologies, such as the toroidal shape of red blood cells or the spherical shape of early endocytic vesicles. Combining these measurements with time-lapse imaging of living cells, we could measure membrane motion speed in top and bottom membranes of Ptk2 cells. Most importantly, we could combine z-STED with both FCS and spectral imaging of polarity-sensitive dyes, which are standard tools to probe the nanoscale structure and dynamics of the plasma membrane. Diffusion measurements with z-STED-FCS revealed identical diffusion properties for the top and bottom membranes, showing an absence of interaction between fluorescent markers and the coverslip. This result addressed an issue of importance in membrane research. Studies of the plasma membrane can either be performed on the bottom or top membrane, which can lead to specific biases. Bias by interaction with the coverglass can occur at the bottom of the cells, while light propagation through the cytoplasm and/or nucleus can bias measurements at the top membrane. Here, we measured using z-STED diffusion in extremely close membranes, where the latter bias was unlikely. Therefore these results confirmed that unbiased measurements can be performed in the bottom membrane of Ptk2 cells. Combining z-STED with spectral imaging and the polarity-sensitive dye NR12S, we could obtain complementary information about the membrane fluidity of these membranes. Again, spectral imaging showed identical biophysical properties of the top and bottom membranes, confirming results measured with FCS. Spectral imaging also revealed minute differences in lipid packing between the plasma membrane and endocytic vesicles.

We observed the undepleted sidelobes which are a well known feature of z-STED. These sidelobes did not significantly deteriorate image contrast or hamper image interpretation, thanks to their low intensity relative to signal and large distance (800 nm) to the signal. The intensity of these undepleted sidelobes was high in this study because we imaged flat fluorescent surfaces and at any point undepleted background contributions emanating from all points in the vicinity of the measurement point added up. These contributions were not visible upon imaging point-like fluorescent emitters like fluorescent beads (Figure 3.5). Undepleted background contributions could be reduced here with deconvolution and could if necessary be physically suppressed by overlaying the z-STED depletion focus with a second depletion focus [26] or perhaps with PSF engineering as was previously done in 4pi STED microscopes [40].

The issue of photobleaching usually associated with STED was mitigated here thanks to the self-replenishing lipid dyes use. This is similar in concept to point accumulation for imaging in nanoscale tomography (PAINT), which was previously demonstrated in STED microscopy [49]. The remarkable brightness and photostability of the dye used here (Abberior StarRed) also certainly played a role in mitigating photobleaching, as proven by the good image quality obtained upon imaging small structures like endocytic vesicles (with a very small pool of fluorophores to replenish bleached ones).

We could perform FCS measurements in the top and bottom membranes of Ptk2 cells, permitted only by the excellent axial resolution provided by z-STED. Such a precision implied that even small motion of the plasma membrane induced significant artefacts in FCS, effectively the maximum achievable acquisition time. In 2D, this issue was solved by combining scanning FCS and off-line correction of membrane motion [132]. This required scanning at speeds larger than the characteristic diffusion times, in practice in the kHz range. Fast scanning in the axial direction was unfortunately not achievable with our piezo

stage used for axial scanning. Axial scanning z-STED-FCS could however in principle be achieved using a fast optical element like a TAG lens [133] or a deformable mirror.

Chapter 5

Adaptive optics for SLM-based z-STED imaging

We obtained an excellent z-STED resolution when imaging cellular membranes close to the coverslip, however image quality can be severely limited by aberrations in deeper specimens. Correction of these specimen-induced aberrations with the sensorless method is much more challenging than the correction of system aberrations developed in chapter 3 because of limited signal levels, unknown specimen structure and, in most cases, photobleaching. Besides, different aberration modes have different effects on the depletion pattern of a STED microscope [23, 25, 103, 134], which induce in turn complex effects in the resulting fluorescence images [24]. This complicates the quantification of image quality and therefore sensorless aberration measurement in STED. Particularly, image brightness, the simplest image quality metric for sensorless adaptive optics, was found to be unsuited to measure image quality in STED microscopy. Indeed, certain aberration modes fill up the central intensity minimum, leading to an exacerbated depletion of signal, while some others open up the depletion pattern, leading to an overall less efficient depletion

and therefore lower resolution, but higher intensities. The effects of aberrations on image brightness become even more complex in the presence of multiple aberration modes, as is generally the case in experiments. Besides, photobleaching may significantly change image brightness during a sensorless AO-STED experiment and consequently bias the aberration measurement procedure. For this reason, the first reported sensorless AO method for STED microscopy made use instead of a hybrid metric combining image brightness and contrast [94]. This approach, however functional, had the disadvantage to require tuning of three experimental parameters and was thus highly microscope- and sample-dependent. Another approach consisted in removing the phase masks that shape the depletion patterns and minimise instead of maximise image brightness [110, 111]. It can be expected however that this method caused increased photobleaching, as fluorescent probes were simultaneously exposed to high excitation and depletion laser powers. To assess the quality of STED images, instead, Fourier-based methods like FRC were used successfully [109]. Fourier-based approaches are however unsuited to detect localised variations in resolution, as is the case of microscopy images. Besides, the optical transfer function (OTF) of the microscope attenuates high-frequency components which contain the information useful for sensorless AO. For these reasons, we propose here to use instead a novel image quality metric based on the wavelet transform of an image [119]. This image quality metric can be employed across multiple imaging systems, making it a promising tool to be integrated in multi-modal platforms which are becoming increasingly needed in many applications [135].

5.1 Methods

5.1.1 Sample preparation

NIH3T3 cells: were grown and prepared as described in chapter 4.

Cells in gel: The protein tom20 in a sample of fixed human fibroblasts were antibody-labelled following the immunolabelling protocol described in details in [59]. Cells were added on top of a polymer gel which was prepared following the protocol described in [136]. Gel thickness was set to 10 µm.

Mouse brain slices: A fixed mouse brain slice, in which the protein homer was antibody-labelled with STAR635P was kindly provided by collaborators at the Institute of Biochemistry in Jena. Detailed sample preparation protocol can be found in ref [137].

Mouse liver: samples of fixed, uncleared mouse liver tissue were kindly provided by Dr Pablo Pablo Hernandez-Varas. They were labelled using the immunolabelling protocol described in [59].

5.1.2 Simulations

The intensity distributions of the excitation and depletion lasers were calculated using the vectorial diffraction theory, as described for instance in ref [134]. We integrated the Debye-Wolf integral in the vicinity of the focal point of the objective:

$$E(x,y,z) = \int_0^{\alpha}\int_0^{2\pi} \vec{e}(\theta\phi)\, T(\theta,\phi)\, exp\left[i\Phi(\theta,\phi)\right] \\ exp\left[ik\left(x\sin\theta\cos\phi + y\sin\theta\sin\phi\right)\right] \times exp\left[ikz\cos\theta\right]\sin\theta d\phi d\theta \tag{5.1}$$

where E describes the electric field at the point x, y, z (the focal point corresponds to the point where x, y and z are equal to 0), $k = n2\pi/\lambda$ with n is the refractive index of the immersion medium and λ is the wavelength. α is the semi-aperture angle used to define

the numerical aperture $NA = n \sin \alpha$. $\Phi(\theta, \phi)$ is the aberration function, defined here as a sum of Zernike polynomials. $T(\theta, \phi)$ describes the phase function of the STED phase mask (set to 1 to model the excitation focus). In the case of the z-STED depletion pattern, it corresponds to phase modulation with a top-hat phase mask and can be written as:

$$T(\theta, \phi) = \begin{cases} 1, & r < \rho \\ -1, & r \geqslant \rho \end{cases} \tag{5.2}$$

where r is the radius in the unit disk of the pupil plane (figure 5.1), equal to $r = n \sin \theta / NA$. In the case of circularly polarised light (as is the case in STED microscopy), $\vec{e}(\theta, \phi)$ can be explicited as:

$$\vec{e}(\theta, \phi) = A(\theta) \sqrt{\cos \theta} \begin{bmatrix} \cos \theta + 1 + (\cos \theta - 1) e^{i2\phi} \\ i\left(\cos \theta + 1 - (\cos \theta - 1) e^{i2\phi}\right) \\ -2 \sin \theta e^{i\phi} \end{bmatrix} \tag{5.3}$$

$A(\theta)$ describes a Gaussian illumination profile, expressed as:

$$A(\theta) = exp\left(-\frac{r^2}{2\sigma^2}\right) \tag{5.4}$$

Depletion patterns were simulated at a wavelength of 755 nm, and excitation was calculated at 640 nm, both wavelengths used in our system. The refractive index was set to 1.518 (oil) and NA to 1.4. The detection profile was defined as a convolution of the excitation profile with a pinhole with a size of 1 Airy unit. Pixel size was set to 10 nm. To minimise computing time, only 2-dimensional (xz) profiles were calculated. Integration was performed in cylindrical coordinates, using the invariance of the calculated foci along the azimuthal coordinate to calculate three-dimensional integrals from two-dimensional simulation data.

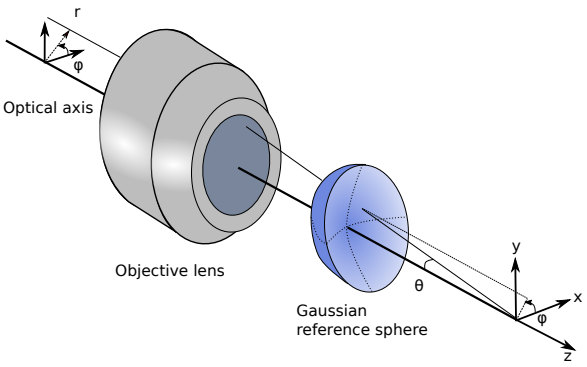

Figure 5.1: Coordinate system used for calculation of Debye-Wolff integral

5.2 Aberration correction procedure

5.2.1 Choice of aberration modes

We used Zernike polynomials to represent wavefronts, as explained in section 2.5.2. Wavefronts were described as a finite sum of Zernike modes and as such, the accuracy of the wavefront representation depended on the number of modes used. In a sensorless AO scheme, unfortunately, the aberration correction time, phototoxicity in living samples and photobleaching scale linearly with the number of aberration modes. The latter was particularly problematic in the case of STED microscopy and it was critical to use only the minimum number of aberration modes. We therefore corrected only low-order Zernike modes, which were found to be predominant in common biological samples [65]. We decided to correct aberration modes 5-11 (coma, astigmatism, trefoil and spherical as defined in table 2.1 in chapter 2), as well as higher order spherical aberrations when focussing deeper in specimens. In most sensorless AO schemes, geometric aberrations (tip, tilt and defocus) do not impact image quality, as they simply shift the position of images. In our case, however, these aberration modes could cause shifts of the depletion pattern, inducing misalignments between excitation and depletion foci. We therefore treated the

first Zernike modes as aberration modes which were corrected alongside others using the sensorless method.

5.2.2 Displacement-free Zernike polynomials

Motivation

In a low NA configuration, the Zernike modes which induce PSF deformations (all modes except tip, tilt and defocus) do not change the PSF position. However, when using a high NA objective, coupling between modes appear: defocus induces PSF distortions along with axial shifts [138], and similarly spherical modes do not only distort the PSF but also shift it [139]. In the case of STED depletion patterns, another effect comes in play: the deformations of the depletion pattern can induce a displacement of the central intensity minimum, without global shift of the depletion pattern. This explains for instance why coma aberrations induce displacements of the central intensity minima of the 2D and z-STED depletion patterns in opposite directions [134]. When performing sensorless AO, it is critical to decouple effects of spatial shifts and pattern deformations which might have opposite effects on image quality. This was achieved in previous work by experimentally measuring the shifts of the depletion pattern induced by coma and spherical aberration modes and compensating them with the appropriate amount of tip, tilt and defocus [94]. We performed a similar calibration here, with two exceptions: we investigated the shifts induced by aberration modes both theoretically and empirically and we used the exact expression of defocus in a high NA system [79] instead of Zernike defocus. The phase function we used to induce axial shift was defined as:

$$Z_4^{'}(r,\phi) = a\sqrt{1-\left(\frac{NA}{n}\rho\right)^2} \tag{5.5}$$

This expression can be directly derived from the diffraction integral (equation 5.1). This aberration mode is not normalised like other Zernike modes, however for convenience and compatibility we will refer to amounts of this mode with rad rms as units. The constant a was set arbitrarily to $a = 4.3$ to ensure that 1 rad rms of the new defocus mode had comparable effect on STED images than 1 rad rms of other modes. In practice, this meant that 1 rad rms of defocus induced a theoretical shift of the PSF of 339 nm (table 5.1).

Dependence on top-hat inner radius

We first simulated the shifts expected for various aberration modes. We calculated axial (for spherical modes) and lateral (for coma) intensity line profiles as described in the methods section (section 5.1.2), with various amounts of aberrations introduced. We measured the relative motion of the pixel of smallest intensity with aberration introduced. For all the aberration modes tested, we found a linear dependency between shift of the central intensity minimum and the amount of introduced aberrations. Measuring the slope of these curve using a linear regression allowed us to calculate the shift in nm/rad. One parameter that needed to be taken into account is the inner radius ρ of the top-hat phase mask. This parameter splits the phase modulation of the top-hat phase mask in two zones: in the inner disk, phase modulation is equal to 0, and in the outer disk, phase modulation is equal to π. Experimentally, the inner radius ρ is set to minimise the central intensity by ensuring destructive interference at the centre of the focus. The value of ρ depends on the shape of the illumination intensity profile, with a flat intensity profile requiring high values of ρ while narrow intensity profiles require smaller values of ρ. As a result, the exact value of this parameter is different in different setups.

We verified whether the value of ρ had an influence on the shift with aberration of the central intensity minimum. For values of ρ ranging from 0.55 and 0.66, we first cal-

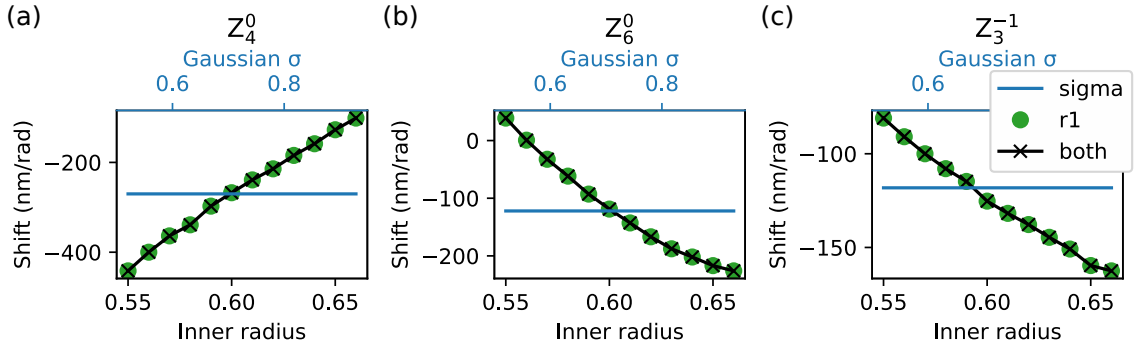

Figure 5.2: Simulation of shifts of the central intensity minimum of the z-STED depletion pattern with aberration modes (a) Primary spherical, (b) secondary spherical and (c) Vertical coma. Shifts were measured along z in (a-b) and along x in (c).

culated the corresponding size of Gaussian intensity profile (equation 5.4, parameter σ) that minimised the central intensity. For pairs of optimised parameters (ρ, σ), we calculated the aberration-dependent shift as described above (figure 5.2, black). We found that different (ρ, σ) pairs led to different shifts. In the case of secondary spherical aberrations (figure 5.2(b)), we even found that depletion patterns with high and low ρ parameter shift in opposite directions. We then verified whether these variations were explained by the different phase profiles corresponding to different radii ρ, or by the different illumination intensity profiles corresponding to different Gaussian sizes σ. To do this, we fixed one of the parameters and measured the aberration-depending shift of the intensity minimum while varying the other (figure 5.2). Our results showed that only the inner radius ρ affects the result.

Experimental measurement of displacement-free Zernike modes

We verified experimentally the results obtained via simulations. We imaged the depletion pattern with a sample of scattering gold beads and introduced various amounts

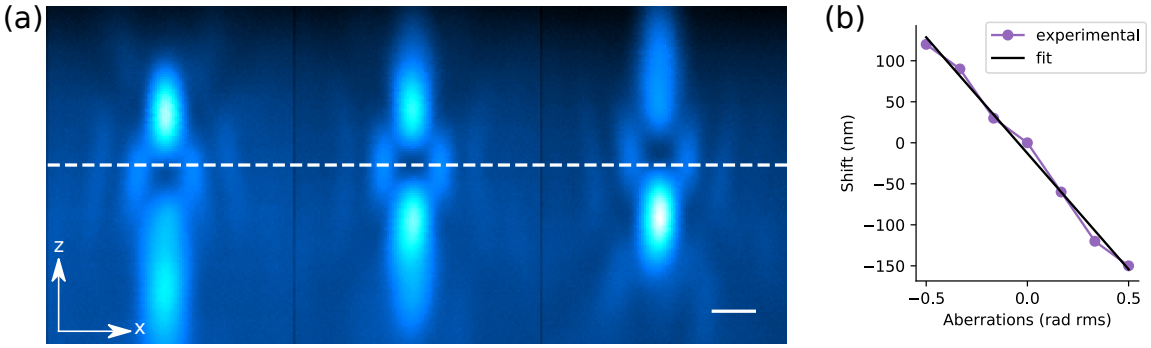

Figure 5.3: Calibration of displacement-free Zernike modes for z-STED microscopy. (a) Effect of -0.5, 0 and 0.5 rad rms of spherical aberration (left, middle and right) on the z-STED depletion pattern imaged with scattering gold beads. Dotted white line: position of the central intensity minimum with no aberrations. Scalebar: 500 nm. (b) Spherical aberration-dependent position of the central intensity minimum (magenta) and linear fit (black).

of aberrations using the SLM (Figure 5.3(a)). The maximum bias value introduced was chosen to ensure distortions small enough to keep a central intensity minimum, which corresponded in practice to 0.35 rad rms for coma and 0.7 rad rms for other modes. For each bias aberration value, we acquired one image of the depletion pattern and localised the position of its central intensity minimum. This was done by first Gaussian smoothing to reduce noise, then a minimum filter was used to find the approximate position of the central intensity minimum, and finally the centre of the pattern was found with maximum accuracy by fitting a 2-dimensional parabola to a 3×3 window centred around the approximate position. As in simulations, we found a linear relationship between the amount of introduced aberrations and the shift of the central intensity minimum. The example of primary spherical aberration can be found in figure 5.3(b). The shift induced by each mode in nanometres per radians was then determined using linear regressions. As determined using simulations, the inner radius ρ of the depletion pattern was expected to have an effect on the values recovered. If it is straightforward to set this parameter in simulations,

Mode	Experimental Shift (nm/rad)	Theoretical shift (nm/rad)
2	184 +/- 26	172
3	174 +/- 24	172
4	361 +/- 16	339
5	139 +/- 45	132-145
6	171 +/- 60	132-145
11	267 +/- 31	184-239
22	146 +/- 21	143-188

Table 5.1: Shifts induced by aberration modes. Standard deviation was used as error for experimental shifts (estimated from 7 to 21 measurements). Theoretical shifts were either directly calculated from equation 5.1 (modes 1-3), or numerically calculated with simulations. In the latter case, a range of values corresponding to shifts with an inner radius of 0.61-0.63 are given.

in experimental systems uncertainties arise, caused for instance by differences between the theoretical and experimental magnification of the relay lenses system used to image the SLM pupil on the BFP of the objective. Besides, ρ was experimentally determined by optimising the brightness of STED pictures of fluorescent beads, and we found that values of ρ comprised between 0.61 and 0.63 yielded comparably good images. For these reasons we repeated the measurements of shift with respect to aberrations for values of ρ within these bounds (much smaller than the total range of possible values, see figure 5.2) and averaged the results. Results can be found in table 5.1, and revealed a good agreement between theoretical and experimental measurements.

We found that measuring the displacement induced by coma was much harder than measuring that of spherical modes for several reasons: first, as these measurements were performed in xy mode, even a small drift along the optical axis could lead to either top or bottom lobes to appear in the centre of the focus. Second, the absolute value of the shifts was smaller than for spherical and finally, the maximum bias allowing conservation of a central intensity minimum was smaller. This led to higher standard deviations in the

measurement of shifts in coma aberrations.

Using both theoretical and experimental data about aberration-induced shifts of the central intensity minimum, we designed the following displacement-free Zernike modes:

$$Z'_7 = Z_7 - 0.8Z_3 \qquad Z'_{11} = Z_{11} - 0.8Z'_4$$
$$Z'_8 = Z_8 - 0.8Z_2 \qquad Z'_{22} = Z_{22} - 0.41Z'_4$$

Throughout this thesis, and unless specified otherwise, it is these displacement-free Zernike modes that are used. Zernike polynomials are normalised so that 1 unit of a mode has a root-mean-square value of 1 rad, and as such the amplitude of Zernike coefficients is indicated in rad rms. We did not normalise the displacement-free Zernike modes and, for instance, 1 unit of the mode Z'_6 did not have an amplitude of 1 rad rms. The amplitude of displacement-free Zernike modes will nevertheless be improperly expressed in rad rms to keep consistent notations. As a result, an amount of 1 rad rms of Z'_6 mentioned in the text actually corresponds to the difference $Z_6 - 0.8Z_2$, with Z_6 having an amplitude of 1 rad rms.

5.2.3 Wavelets-based image quality metric

Part of a sensorless AO scheme consists of quantitatively assessing image quality. In STED microscopy, aberrations were expected to essentially induce changes in resolution. To monitor such variations, we chose to use a wavelet-based image quality metric previously described in [119]. We will provide here a brief description of the principles and implementation of this image quality metric. Consider an $m \times n$ image containing N pixels. The wavelet transform decomposes this image in a set of coefficients $(d_j)_{j=1...J}$, where j is the decomposition level and J the maximum decomposition level. Each of the coefficients d_j is an image containing information at the scale $2^{j-1}\delta_P$, where δ_P is the pixel size.

When using the stationary wavelet transform, as we did throughout this thesis, each coefficient has the same size as the original image. There are many different wavelet functions available in the literature, each optimised to detect specific features, for instance edges. We chose in this thesis to use the starlet wavelet [140], a wavelet well suited to describe isotropic objects which are frequently encountered in microscopic images. We empirically set the maximum decomposition level J to 5 (Figure 5.4(a)). As such, the coarsest coefficient had a resolution equal to $16\delta_P$, corresponding to a scale of 480 nm with the usual 30 nm pixel size we used, a scale well above any expected changes in resolution due to aberrations. We noticed that the first coefficient, containing the highest frequency information, was dominated by shot noise so we chose to discard it. We estimated the amount of information in each coefficient as the sum squared of the pixels of this coefficient. As a result, each image was described by a vector $\vec{m'}$ of dimensions J-1 (4 in our case):

$$\vec{m'} = \left[\sum_{k=1}^{N^2} (d_j)_k\right]_{j=2...J} \tag{5.6}$$

As aberrations are introduced in the system, the energy of high resolution coefficients is transferred in the low resolution ones. The absolute value of the sum squared of the pixels of the wavelet coefficients can vary not only because of changes of frequency content, but also because of variations of intensity of the original images. Indeed, if the brightness of the original image increases, so does that of all the wavelets coefficients. In STED, this can be problematic, as certain aberration modes increase image brightness while deteriorating image quality [94]. To remediate this, we normalised the vector $\vec{m'}$:

$$\vec{m} = \frac{\vec{m'}}{\sqrt{\sum_{j=1}^{J} m_j'^2}} \tag{5.7}$$

To illustrate the sensitivity of the different elements of the vector $\vec{m}$ to aberrations, we imaged the mitochondria of a fixed cell. The mitochondria were imaged close (1-3 µm) to

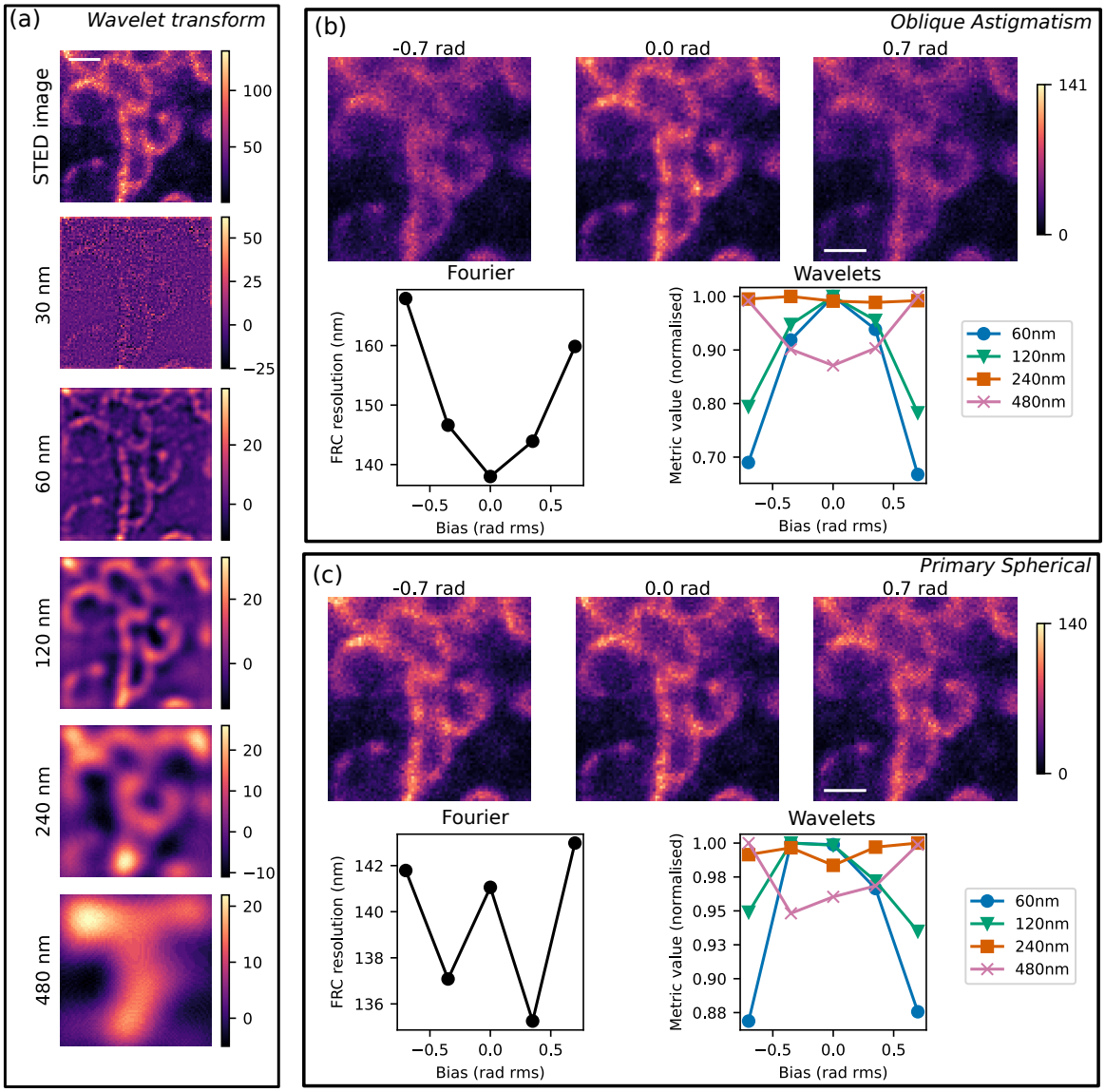

Figure 5.4: Wavelet transform for sensorless AO STED microscopy. (a) z-STED microscopy image of mitochondria (top) and detailed coefficients of its starlet transform, at scales specified on the left. (b)-(c) Introducing aberrations in the specimen using the SLM (oblique astigmatism (b) and primary spherical (c)). Top: images with -0.7 (left), 0 (middle) and 0.7 rad rms of aberrations introduced in the system. Bottom: variation of Fourier-based (left) and wavelet-based image quality metrics with bias. Scalebars: 500 nm. STED laser power: 16 mW.

the coverslip, so no sample-induced aberrations were expected. Thanks to the calibration procedure described in chapter 3, we had also removed system aberrations and as such expected no aberrations to be present. Using the SLM, we introduced various amounts of astigmatism in the system and acquired the corresponding images (Figure 5.4(b)). As expected, wavelets coefficients exhibited an extremum for a bias of 0 rad rms, suggesting that indeed no astigmatism was present in the system. This could be verified by visual inspection of the corresponding images, as well as calculation of another metric based on the FRC method on single images [141]. Applying primary spherical aberration instead of oblique astigmatism in the system led to substantially lower image degradation (Figure 5.4(c)), which could still be measured using the wavelet metric but not with the FRC metric.

5.2.4 Finding the correction from the wavelet vectors

In sensorless experiments using the wavelet quality metric described in the previous section, we calculated four image quality curves instead of one. To derive a correction, we first fitted each curve individually using a parabola. We could then find a set of 4 distinct maxima $c_i = c_1 \dots c_4$. A simple approach to merge these four maxima in one could consist of defining the average of c_i as the correction. However, this would disregard the different sensitivity to aberrations of different coefficients: for instance, in Figure 5.4(b-c), one can see that the curve corresponding to the finest wavelet coefficient (resolution 60 nm) varies a lot with aberrations, while the coarser curve corresponding to a resolution of 240 nm contains very little information. The sensitivity to aberrations of one wavelet scale or another depends on STED laser power, amounts of aberration present as well as specimen structure, and as such cannot be predicted. To avoid biasing the calculation of the correction, we weighted each extremum with a function defined heuristically. We

made two assumptions to define these weights: first, that lower fitting residuals were indicative of a more informative curve. Second, we assumed that a higher curve amplitude was related to a higher information content. Using these two assumptions, we defined the weights as:

$$w\left(j\right) = \left(m_{j,max} - m_{j,min}\right)/\epsilon_j \tag{5.8}$$

where $m_{j,max}$ and $m_{j,min}$ are respectively the maximum and minimum of the j^{th} coefficient of the vector $\vec{m}$ across all bias values. ϵ_j represents the fitting residuals normalised to the maximum curve amplitude, defined as:

$$\epsilon_j = \frac{\sum_b \left[\left(m_j\right)_b - \left(\hat{m}_j\right)_b\right]^2}{\left(m_{j,max} - m_{j,min}\right)^2} \tag{5.9}$$

where $\left(\hat{m}_j\right)_b$ is the value of the parabola fitted to the curve at a bias value b. Using these weights, the correction was defined as:

$$c = \frac{\sum_{j=1}^{J} w\left(j\right) c_j}{\sum_{j=1}^{J} w\left(j\right)} \tag{5.10}$$

5.2.5 Sensorless and imaging parameters

The number of measurements in sensorless AO experiments is an important parameter that has a significant influence on the accuracy of correction [142]. A low number of measurements per sensorless AO experiment leads to a reduced photodamage, but also reduces the correction accuracy. In practice, we used between 5 and 9 measurements per aberration mode. The STED laser power used for sensorless AO loops was another important parameter. Low STED laser power corresponds to an expected lower sensitivity (with the extreme case of no STED power leading to no wavefront sensing at all) while high STED laser power would lead to enhanced photobleaching. The effective STED laser power we used throughout this chapter for sensorless correction was thus determined as

a tradeoff between these two effects and set to 11 mW. For imaging, STED laser power was set to values ranging from 25 to 110 mW. Excitation power was set to 8-20 µW.

5.2.6 Practical implementation

There are many reasons that can lead a sensorless loop to fail. For instance, no variations in image quality can be measured if the depletion pattern is too aberrated in the first place. Sensorless AO loops can also diverge if significant photobleaching occurs during acquisition, in which case certain imaging parameters like excitation power or pixel dwell time need to be reduced. A sensible implementation of sensorless AO in STED therefore needs to take these caveats into account by allowing quick inspection of sensorless AO results, and manual correction of these when necessary. We designed and implemented a custom graphical user interface (GUI) to achieve this. This GUI was implemented in Python using the library PyQt5 and communicated with Imspector using the Imspector Python interface. To run a sensorless AO loop, the imaging parameters (laser powers, imaging area, scanning parameters etc.) were first defined by the user using Imspector as for any imaging experiment. The parameters of the sensorless experiments were then defined using the bespoke AO GUI and the sensorless AO loop could start. This GUI was developed to work with Imspector specifically, however it could be easily adopted to any microscope acting like a server (e.g the acquisition of which can be triggered by another program) if necessary.

5.3 Results

5.3.1 Imaging the top membrane of a thick cell

We validated our aberration correction first by correcting spherical aberrations in the top membrane of a NIH3T3 cell (Figure 5.8). The bottom membrane, close to the coverslip

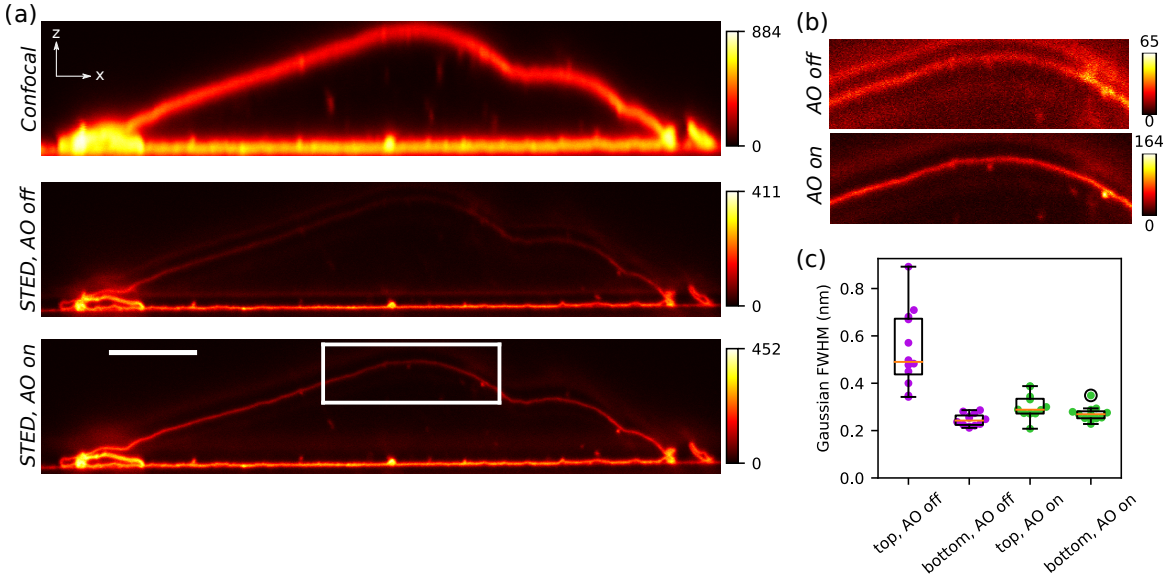

Figure 5.5: Aberration correction to image membranes of a thick cell. (a) Imaging the plasma membrane of a whole NIH3T3 cell in confocal (top) z-STED without aberration correction (middle) and z-STED with aberration correction (bottom). (b) Zoom on the area highlighted by a white square in (a), for z-STED without (top) and with (bottom) AO. (c) Measurement of axial Gaussian FWHM of z-STED images of the top and bottom membranes of 3 cells, with (green) and without (magenta) aberration correction. Scalebar: 5 µm

did not suffer from optical aberrations (Figure 5.8(a)). However, the top membrane exhibited significantly reduced intensity and exacerbated undepleted lobes, indicating that aberrations had caused the top lobe of the depletion pattern to shrink. This was characteristic of spherical aberrations (as shown in Figure 5.3), which were expected because of the refractive index mismatch between the refractive index of the immersion oil and

that of the cytoplasm. We therefore attempted to correct only primary spherical aberrations. Because we used lateral (xy) images of the membrane, it was impractical to run the sensorless routine when imaging the flat top membrane which contained no lateral information. Instead we ran the sensorless routine while imaging one of the side membranes located approximately at half the total axial size of the cell. Correction of primary spherical aberration led to a drastic improvement in image resolution and brightness in the top membrane (Figure 5.8(b)), where AO almost tripled the fluorescent count. We quantified the resolution improvements brought by AO by imaging different cells with and without AO, and measuring the Gaussian FWHM of the top and bottom membrane in each condition. We found that as expected, the top membrane appeared much larger than the bottom one when no aberration correction was applied (Figure 5.8(c)), and that AO remediated this issue. We also found that the FWHM of both membranes was slightly larger with AO. This was expected since the aberration correction procedure was performed in the middle of the cell, thus the correction found was optimal for neither membrane.

5.3.2 Imaging cells through a layer of aqueous gel

We then attempted to correct aberrations in a deeper specimen. We created an artificially aberrating specimen by placing a sample of human cells in which we labelled mitochondria on top of an aqueous gel. This configuration had two advantages: first, it induced controllable aberrations, as we expected spherical aberrations to be caused by the refractive index mismatch between the gel and the immersion oil. Secondly, this configuration is commonly used for experiments of traction force microscopy [136], where the forces exerted by cells on their environment are quantified by measuring the displacements they induce on an aqueous gel of known stiffness. In order to measure the gel

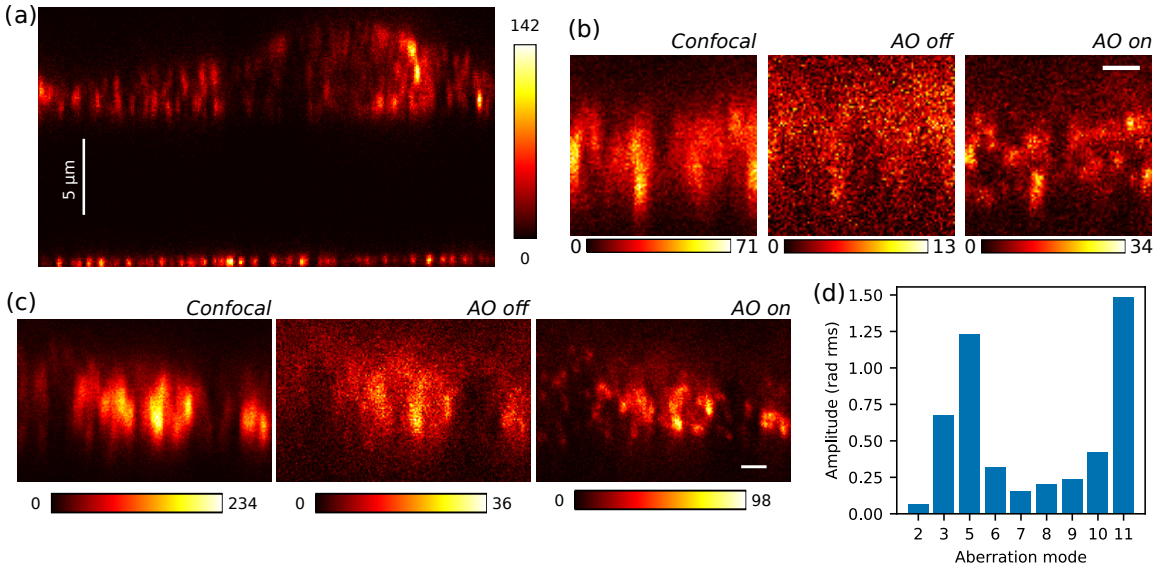

Figure 5.6: Aberration correction in fixed cells on a layer of gel. (a) Overview (confocal) of a cell on top of gel with fluorescent beads (bottom) at the coverslip. (b)-(c) Aberration correction results in two different regions of interest. Comparison of confocal (left) STED without AO (middle) and STED with AO (right). Scalebars: 1 µm. (d) Aberrations corrected in (b) and (c). Mode were numbered following the convention defined by Noll [68], as indicated in table 2.1

thickness experimentally, we coated the coverslip with fluorescent beads (Figure 5.6(a)). The distance between the coverslip and the first labelled features in cells was approximately equal to 10 µm. A first inspection of the sample in confocal mode revealed that the labelling was imperfect: we observed pointillist instead of the expected continuous structures (as in Figure 3.6). This did not however alter the optical relevance of this experiment. The quality of z-STED images was significantly deteriorated by optical aberrations and could be improved with sensorless aberration correction (Figure 5.6(b-c)). As expected, we found large amounts of spherical aberrations present in the system (5.6(d)). We also found a large amount of tilt, indicating a misalignment between the excitation and depletion beams. This misalignment could be caused either by coma aberrations or by thermal and mechanical drift. Finally, we also measured large amounts of astigmatism which were

unexpected. This could have been caused for instance by an anisotropic strain appearing during the gel preparation.

5.3.3 Aberration correction in tissues

Correction of aberration in a rat brain tissue with prior spherical aberration compensation

Having consistently found spherical aberrations caused by high focusing depth, we attempted to pre-correct spherical aberrations in a sample of mouse brain tissue to facilitate the aberration correction. We therefore selected a region of interest (ROI) at moderate depth, where z-STED imaging was still possible, yet deteriorated (Figure 5.7(a)). Our previous results suggested that this corresponded to an amplitude of primary spherical aberrations of less than 1 rad rms, therefore we chose to induce 0.75 rad rms of primary spherical aberrations. A refractive index mismatch inducing not only primary but also secondary spherical aberrations, we introduced in our system the corresponding amount of -0.2 rad rms of secondary spherical aberration (the ratio between primary and secondary spherical was calibrated in STED-FCS, using results described in the Figure 6.4 in the next chapter). We then performed one round of aberration correction for the low-order Zernike modes (defocus, coma, astigmatism, primary and secondary spherical).

Aberration correction significantly improved image quality (Figure 5.7(b)), which was confirmed by comparing intensity profiles in the same areas with and without correction (Figure 5.7(c-d)). Image registration was used to correct for a 5 pixel shift between the two images. The total aberration measured (Figure 5.7(e)) confirmed that spherical aberrations were predominant and that therefore precorrecting them yielded significant improvements.

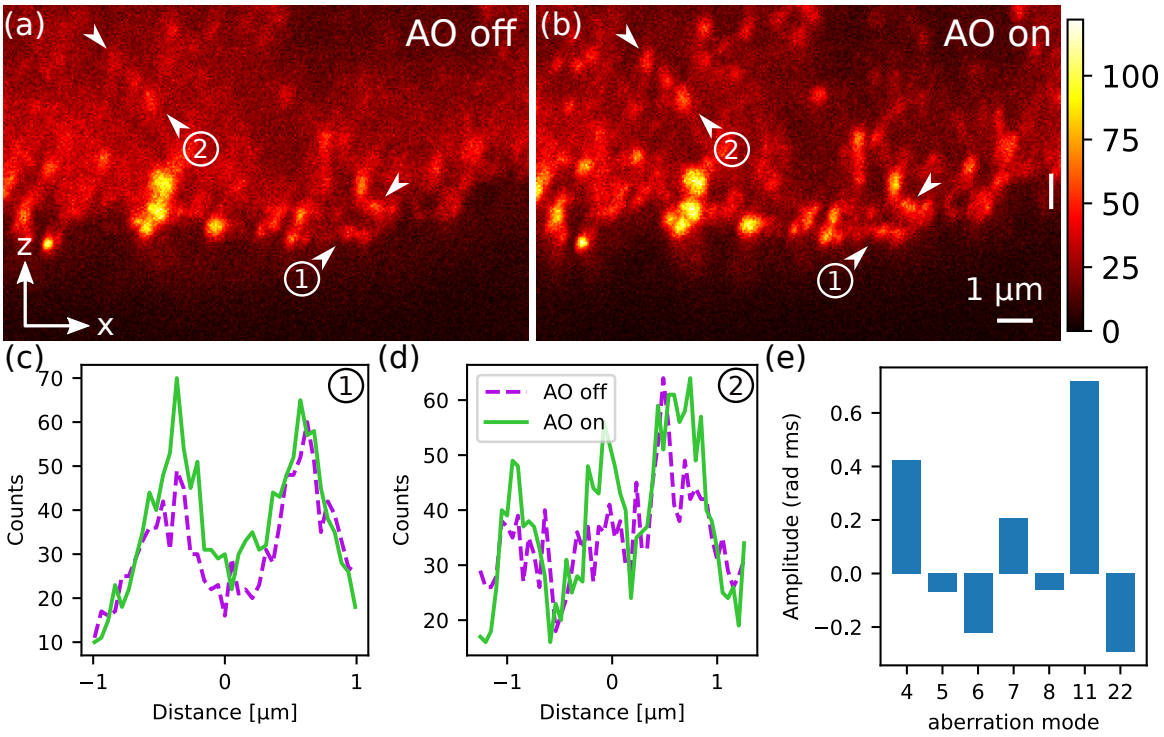

Figure 5.7: Aberration correction in a rat brain with precorrection of spherical aberration. (a-b) Axial z-STED image of a rat brain slice, without (a) and with (b) aberration correction. Scale bars: 1 µm. (c-d) intensity profiles along the lines indicated in panels (a-b), without (dotted magenta lines) and with (green plain lines) aberration correction. (e) Measured aberrations.

Correction of aberration in a mouse liver tissue without prior aberration compensation

Finally, we demonstrated the potential of our technique to correct aberrations in tissue samples without prior assumptions on the structure of aberrations. We first used for this an uncleared sample of mouse liver (courtesy of Dr Pablo Hernández-Varas) in which we labelled keratin. We imaged the sample first close to the coverslip, while progressively increasing the penetration depth. To facilitate the aberration correction process, we started the aberration correction process at each depth using the correction found at the previous depth. We found spherical aberrations to be the main aberration mode, even though

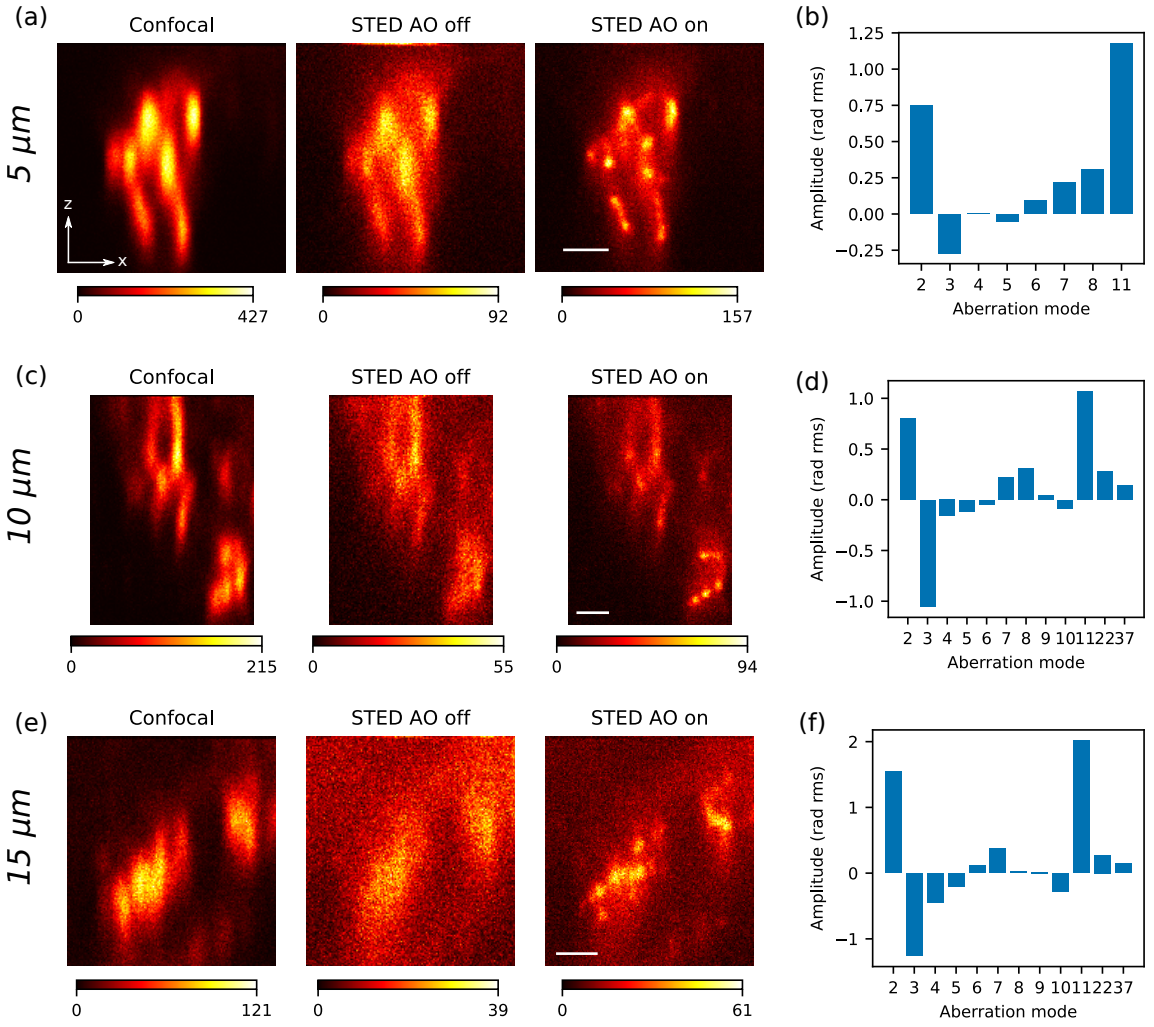

Figure 5.8: Results of aberration correction for z-STED imaging in mouse liver tissues, at focussing depths of 5 ((a)-(b)), 10 ((c)-(d)) and 15 ((e)-(f)) µm. Scalebars: 1 µm

as previously noted we found relatively high values of tip and tilt caused by either drift or coma aberration. At the lower depth of 5 µm, we deemed that correcting only one spherical mode (primary spherical) would be sufficient to recover an optimal image quality (Figure 5.8(a-b)). At larger depths (10-15 µm), expecting further spherical aberrations, we also corrected secondary and tertiary spherical aberrations (Figure 5.8(c-d)). AO led in every case to significant improvements in image quality, which were more pronounced at increased depth (Figure 5.8(e)) where a higher amount of aberrations were present (Figure 5.8(f)).

5.4 Discussion

Previous implementations of adaptive optics for STED microscopy either corrected excitation first with a second SLM in the excitation path [94, 110] or corrected all three beam paths using a deformable mirror [109, 115, 119]. Here, instead, we performed for the first time sensorless aberration correction in a STED microscope with a SLM in the depletion path as a sole adaptive element. This was made possible among other things by a novel and robust image quality metric based on the wavelet transform of an image [119]. Using this new sensorless AO scheme, we could correct aberrations in a wide range of conditions, in both living and dead specimens, paving the way for many potential applications. We used for this a bespoke microscope, however SLMs are already available in commercial implementations of STED, so we believe our technique has the potential to be used widely. Using a single SLM in the depletion beam only has the advantage of increased simplicity, but reduces the maximum amount of aberrations that can be corrected. Too many aberrations can significantly deteriorate the excitation and detection PSFs, making even confocal imaging impossible. Besides, if the depletion focus is initially so aberrated that no

resolution improvement via STED is possible, the sensorless algorithm is deemed to fail. In this case, indeed, introducing aberrations with the SLM during the SLM process does not lead to a change in resolution, as mostly noise can be measured. This technique therefore requires that the initial aberrations are low enough when a sensorless measurement starts. This last effect can however be bypassed by performing the aberration correction layer by layer as we did in tissue samples: we started the AO procedure at each depth with a level of aberrations small enough to perform sensorless AO correction. In other samples where the structure of aberrations is known, a precompensation can be calculated [42, 102] before performing the full correction, as we showed in mouse brain samples (Figure 5.7). Most of the aberrations we measured were spherical aberrations, which could be expected as we used an oil immersion objective lens. We found also consequent amounts of other modes, like astigmatism. Perhaps more surprisingly, we also measured significant amounts of tip and tilt, which could not be caused by solely coma aberrations and which we attributed to thermal and mechanical drift in the system that misaligned excitation and depletion beams. In this sense, we used AO as a means of in-sample autocalibration, in an approach which was previously used on calibration samples [108].

Chapter 6

Adaptive optics for STED-FCS

The combination of super-resolution STED with FCS allows the measurement of diffusion speeds with increased resolution. In chapter 4, we used this technique to study the plasma membrane, which is the main field of application of STED-FCS [56, 61]. In membrane studies, two-dimensional (2D) diffusion is measured. Most commonly (and unlike in chapter 4), the lateral diffusion of a single membrane is measured at different scales, comparing the diffusion speeds measured within a confocal observation area (with a diameter in the range of between 200 and 400 nm) and within a STED observation area (diameter comprised between 20 and 50 nm). The comparison of diffusion speeds measured at each scale allows the measurement of different diffusion modes [61]. FCS was also used to measure diffusion in three-dimensional (3D) environments like the cell cytoplasm [143, 144]. STED-FCS however suffers from major setbacks in 3D. When performed with 2D-STED, the most commonly used confinement mode, the measurement of average number of molecules in the observation volume and average transit time in the observation volume with STED-FCS are biased by out-of-focus background [57, 62]. These can be addressed by means of elaborate background substraction methods [27, 64, 145] or using

custom fitting methods that account for distortions caused by background [62, 146]. This comes however at the cost of either higher experimental complexity or extra hypotheses on the observed system (for instance on the dye's lifetime). For these reasons, it can be preferable to physically suppress this background using a more suited depletion pattern. The other commonly used depletion pattern, z-STED, was only scarcely used for STED-FCS in 3D and did not reduce background effectively [55, 57]. This low performance could have been caused by optical aberrations, to which z-STED is very sensitive [23, 25, 103]. In order to obtain maximum performance of z-STED-FCS in 3D, we therefore developed an aberration correction routine for z-STED-FCS. To do this, we modified the procedure we developed for STED imaging in chapter 5, to include among other things a quality metric specific to FCS. We used this method to correct multiple aberration modes in solution and in biological specimens. Using this method, we could investigate cytoplasmic diffusion modes as part of a wider biological investigation. We published the results presented in this chapter [147], and the figures shown here were adapted from this publication.

6.1 Materials and methods

6.1.1 FCS

For each FCS measurement, the FCS curve was obtained by correlating the fluorescence intensity time trace $I(t)$ using the python package *multipletau* [148]. A detailed description of the fitting model can be found in section 2.4.2). In short, FCS curves were fitted using a general FCS model assuming a Gaussian observation volume:

$$G_D(\tau) = \left(1 + \frac{T}{1-T}\exp^{-\tau/\tau_T}\right)\frac{1}{N}\frac{1}{1+(\tau/\tau_{xy})^{\alpha}}\frac{1}{\sqrt{1+\frac{1}{K^2}\left(\frac{\tau}{\tau_{xy}}\right)^{\alpha}}} + \delta \qquad (6.1)$$

Where T refers to the triplet correlation amplitude, τ_T is the triplet correlation time, N is the average number of molecules in the observation volume, τ_{xy} is the average lateral molecular transit time in the observation volume, K is the aspect ratio and α is a correction factor to account for non-Brownian diffusion ($\alpha < 1$ corresponds to subdiffusion, $\alpha = 1$ to Brownian diffusion). α was set to 1 in solution, and to 0.75 in cells to account for subdiffusion in the cytoplasm [149]. As a measure of noise in FCS curves, we calculated the root-mean-square difference between the FCS curve and its fit normalised to the curve amplitude (nRMSD)[150], calculated between 12 µs (above triplet correlation time) and 100 µs (below most transit times). Excitation power was set to 8.6 µW in solution and to 6 µW in cells.

6.1.2 Samples

Dye samples: A solution of freely diffusing dye molecules was prepared by diluting Abberior Star Red NHS dyes (Abberior) in a 1:1 water:glycerol solution to a concentration of 50 nM. Glycerol was used to increase the viscosity of the medium and decrease the diffusion speed of the dyes, which otherwise diffuse too fast for reliable assessment of average number of molecules in the observation volume and transit times with STED-FCS.

Cells: Human fibroblasts (GM5756T, Moser, Baltimore, USA) and HEK KO PEX5 were maintained in a culture medium consisting of DMEM with 4500 mg glucose/L, 110 mg sodium pyruvate/L supplemented with 10% fetal calf serum, glutamine (2 mM) and penicillin-streptomycin (1%). The cells were cultured at 37 °C/ 5% CO_2. Cells were grown

in a 35 mm imaging dish with an ibidi glass coverslip bottom (ibidi GmbH, Germany), and transfected with a plasmid expressing a fusion protein of GFP and SNAP-tag using Lipofectamine 3000 transfection reagent (Invitrogene, Carlsbad, USA). 24 hours after transfection, the cells were incubated together with SNAP-Cell 647-SiR (New England Biolabs (UK) Ltd., Hitchin, UK) or SNAP-Cell505 to label the SNAP-tagged PEX5L and washed twice in culture medium after 40 min incubation, with a waiting time between washings of 20 min. Finally, the culture medium was substituted with L-15 medium (Sigma-Aldrich, Dorset, UK) and each sample was visualized at 37°C for no longer than 2 hours.

6.2 Data fitting

An important step when performing STED-FCS consists of fitting the FCS curves to a known model (section 6.1.1) to extract parameters such as the average number of molecules in the observation volume N or average molecular transit time τ_{xy}. Up to 7 parameters can vary at the same time when fitting a FCS curve to equation 6.1. Unfortunately, the molecular brightness of conventional fluorophores is not high enough to fit all these parameters at the same time [55], thus requiring hypotheses to reduce the number of variables. In previous implementations of z-STED-FCS, it was assumed that the lateral transit time τ_{xy} was constant because z-STED increases predominantly the axial resolution [55, 57]. To verify this, we acquired 3D image stacks of immobilised fluorescent beads at different STED laser powers, from which we extracted 2D axial images of single beads. Fitting axial images with a Gaussian function, we measured the variations in axial and lateral Gaussian FWHM with STED laser power (Figure 6.1(a)). We observed in our system that the lateral size of the z-STED focus decreased by up to 30% , which would correspond in STED-FCS to a two-fold reduction in lateral transit time. The approximation that τ_{xy}

was constant would therefore not be verified in our system.

To account for this effect, we developed a new fitting method in which we fitted lateral and axial transit times jointly using prior information on the possible shape of the observation volume. In absence of aberrations, indeed, the lateral and axial dimensions of the observation volume depend only on the STED laser power (Figure 6.1(a)). It is thus possible to describe the shape of the observation volume with a single parameter instead of two. In practice, we plotted the variations of the aspect ratio $K = \omega_z/\omega_{xy}$ with respect to the lateral size ω_{xy}, both obtained my measuring Gaussian intensity profiles in images of fluorescent beads. We then fitted this curve with a heuristic (exponential) function (Figure 6.1(b)):

$$K\left(\frac{\omega_{xy}}{\omega_{xy,confocal}}\right) = a\exp\left(b\frac{\omega_{xy}}{\omega_{xy,confocal}}\right) + c \tag{6.2}$$

With the empirical parameters determined equal to $a = 0.067$, $b = 3.81$ and $c = -0.39$. During the fitting process, we calculated the ratio $\frac{\omega_{xy}}{\omega_{xy,confocal}}$ from the ratios of lateral transit times:

$$\frac{\omega_{xy}}{\omega_{xy,confocal}} = \sqrt{\frac{\tau_{xy}}{\tau_{xy,confocal}}} \tag{6.3}$$

We verified the performance of this new fitting method, by comparing the results obtained with this and the former method on STED-FCS data acquired in solution as well as in cells (Figure 6.7 in Annex A). Observation volumes estimated with both methods were very similar, while our new fitting method had the advantage of being physically more realistic (taking into account increase in lateral resolution) and more robust against artefacts that commonly occur in more challenging datasets (in cells). The aspect ratio K was set to 4 for confocal FCS curves. This value was higher than the aspect ratio determined from imaging (Figure 6.1(b)) to account for aberrations affecting the excitation beam, as previously in STED-FCS ([55]). Triplet correlation times were fixed to 12 µs in solution (determined by

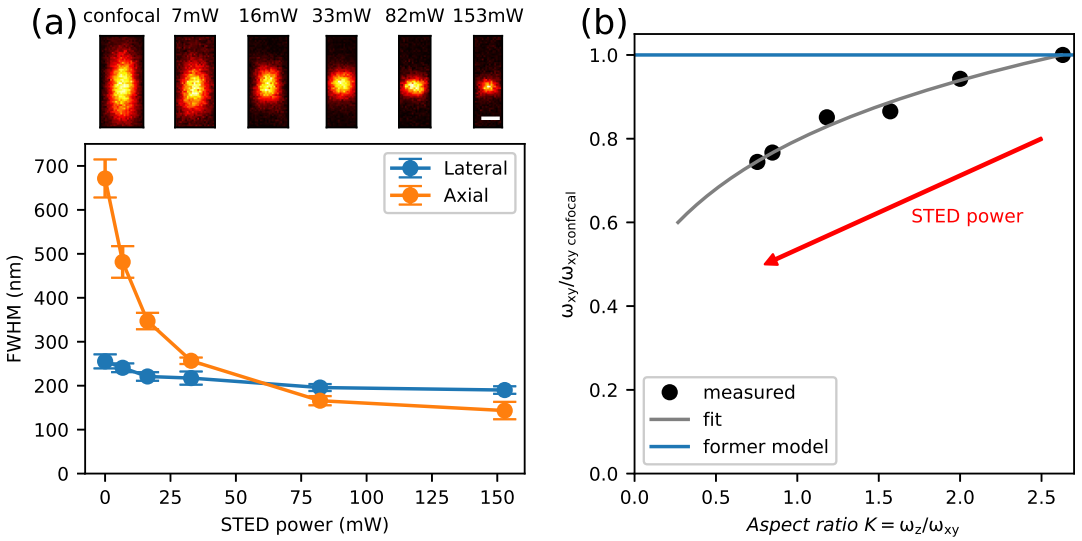

Figure 6.1: Variations in the shape of the effective observation volume with STED laser power. (a) Determination of lateral and axial dimensions (full-width-at-half-maximum, FWHM) of the effective observation spot at different STED laser powers using images of fluorescent beads. Top: xz images of fluorescent beads acquired at different STED laser powers (scale bar 200 nm). Bottom: Values of axial and lateral FWHM from gaussian fits to intensity profiles over images of individual beads returning axial and lateral resolution variations with STED laser power (mean +/- s.d., n = 10 beads). (b) Values of the lateral beam waist ω_{xy} (normalized to the value $\omega_{xy,confocal}$) as a function of the aspect ratio $K = \omega_z/\omega_{xy}$ as determined from the bead images of (a) (black dots) were fitted with an exponential function (grey curve) describing the variations of the shape of the observation volume with STED laser power to design a novel STED-FCS fitting model. The previous model neglecting the reduction in lateral dimension (blue line) is also plotted for comparison.

fitting confocal FCS curves with long integration times) and 5 µs in cells (corresponding to the triplet correlation time usually reported in the literature for this dye).

6.3 Sensorless AO scheme

6.3.1 Quality metric for STED-FCS

An appropriate quality metric is the key to a successful sensorless AO implementation. In AO-STED imaging, this was done using a wavelet-based image quality metric that optimised the high-resolution content within images. This approach could potentially be used to correct aberrations first and perform FCS experiments later, for instance when imaging membranes (Chapter 4). However, this strategy could not be deployed in most STED-FCS experiments in 3D, for instance to study the diffusion of fluorescent proteins in the cytoplasm, as the label is evenly distributed in the environment and no spatial frequency can be optimised to assess image quality. Instead, we expected metrics based on FCS measurements to be suited to assess measurement quality. One solution would consist of acquiring intensity timetraces, correlate them, fit the curves to extract average number of molecules and transit time in the observation volume and assess the quality of the focus. For instance, aberrations are expected to increase average transit times by increasing the size of the effective observation volume. However, this approach would have several drawbacks: firstly, it is computationally intensive and would slow down the aberration correction process. Secondly, fitting FCS curves usually requires fixing certain parameters like triplet correlation time and aspect ratio. This is impractical, as this requires prior knowledge on the parameters of the experiment, and more importantly as these parameters (like aspect ratio) might change with aberrations. Finally, the fitting process is prone

to diverging, resulting in absurd values that need to be manually discarded and would greatly complicate the aberration correction process.

Instead, moments of the intensity distribution were used as metrics in confocal FCS [96, 99]. The first moment corresponds to the average photon count and was used as a simple metric in confocal FCS [96]. Average molecular brightness and average number of molecules in the observation volume can be calculated directly from the higher moments of the intensity distribution [54], as described in section 2.4.2. The corresponding formulae are recalled here:

$$\epsilon = \frac{\left\langle (\Delta I)^2 \right\rangle - \langle I \rangle}{\langle I \rangle} \tag{6.4}$$

$$N = \frac{\langle I \rangle^2}{\left\langle (\Delta I)^2 \right\rangle - \langle I \rangle} \tag{6.5}$$

where $\langle . \rangle$ is the averaging operator, $\left\langle (\Delta .)^2 \right\rangle$ is the variance operator and I is the intensity timetrace. Average molecular brightness was found to be a suitable quality metric for FCS, even outperforming average intensity in certain situations [99]. These metrics were suited to confocal FCS as they are sensitive to the quality of the focus: when a confocal focus degrades, the average intensity decreases due to more light being rejected by the pinhole, leading to a decrease in average molecular brightness and the resolution degrades, leading to an increase in average number of molecules in the observation volume.

In STED-FCS, however, more complex effects are at play. Aberrations have various effects on the STED beam [25, 94, 134] like filling up the central intensity minimum (leading to a loss of resolution and signal) or opening up the depletion ring (leading to a loss of resolution and increase in signal). For this reason, average intensity was an unsuitable metric for STED-FCS. To determine whether N or ϵ were suitable metrics, we measured

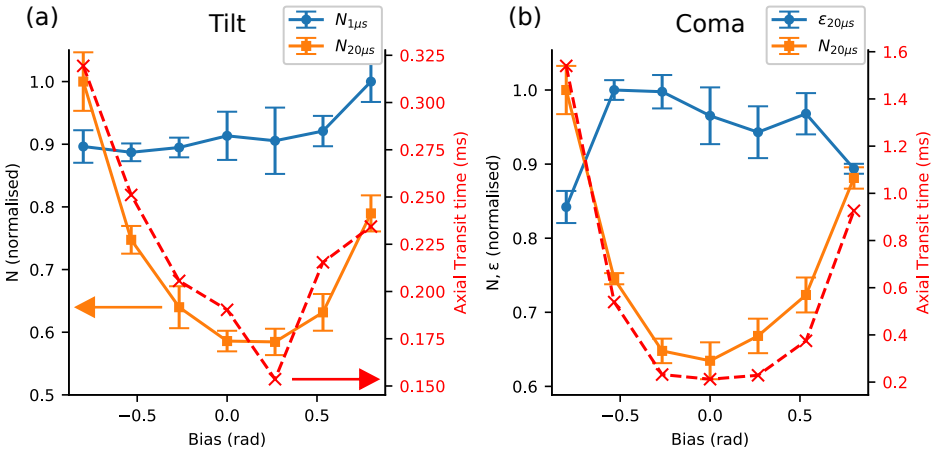

Figure 6.2: Design of STED-FCS quality metric for sensorless aberration scheme. (a-b) Experimental measurements of N and ϵ against aberrations in a solution of Abberior Star Red dyes. (a) Impact of data binning on variations of N with aberrations (left axis) and on the axial transit time (red, right). (b) Comparison of N and ϵ variations with aberrations. STED laser power = 16 mW.

how they were affected by aberrations using a calibration solution of Abberior StarRed dyes diffusing in a water:glycerol mix (Figure 6.2). To design the best quality metric for STED-FCS, we acquired a series of 10s intensity timetraces with various amounts of aberration introduced by the SLM. Intensity timetraces were both correlated to extract average transit times and split in smaller, 2s-long traces to calculate ϵ and N. Photon counts were recorded with a binning time of 1 µs, well below the expected transit times. At these short binning times, intensity fluctuations can be caused not only by diffusion, but also by molecule blinking caused by triplet state fluctuations or by Poisson noise. Besides, detector afterpulsing can induce artificial fluctuations that bias measurements of N and ϵ. This can be alleviated by binning the intensity timetraces after acquisition. To verify this, we compared the quality metric curve obtained with and without 20-fold binning (Figure 6.2(a)). While the non-binned curve contained little information, the binned curve exhibited a clear minimum as expected. The aberration bias minimising the quality metric also

minimised the average axial transit time as expected. The resampling factor was empirical and was chosen to ensure that unwanted fluctuations were averaged out on the one hand and on the other hand that the fluctuations induced by molecular motion were not. In practice, we used binning between 20 and 50 µs throughout this thesis, below the average transit times we measured.

We then compared the performance of N and ϵ as quality metrics. In most cases, both metrics conveyed the same information. However, in certain cases, we found that ϵ did not vary much with aberrations while variations of N allowed determination of a correction, which was confirmed by similar variations in axial transit times (Figure 6.2(b)). We therefore decided to use N as a quality metric for STED-FCS.

6.3.2 Sensorless parameters

Quality curves were fitted with a parabola. 7 measurements were acquired for each aberration mode, with acquisition times ranging from 3 to 12 seconds. We corrected low order Zernike modes: tip, tilt, defocus, astigmatism, coma and primary and secondary spherical. A series of 7 measurements to set the correction of one mode is referred to as a correction round. The maximum bias aberrations applied for a correction round was set to 0.8 rad rms, unless specified otherwise.

6.4 Results

6.4.1 AO improves the performance of STED-FCS in solution

We first corrected aberrations in a solution of freely diffusing Abberior StarRed dyes, at a low depth of 3 µm. We performed one round of aberration correction for coma, astigma-

tism, tip, tilt and defocus. We found relatively high amounts of crosstalk between primary and secondary spherical modes as previously reported [94], therefore we performed in total 5 correction rounds for these modes, the last two ones with a smaller value of the maximum aberration bias (0.6 instead of 0.8 rad rms) for higher sensitivity. Monitoring

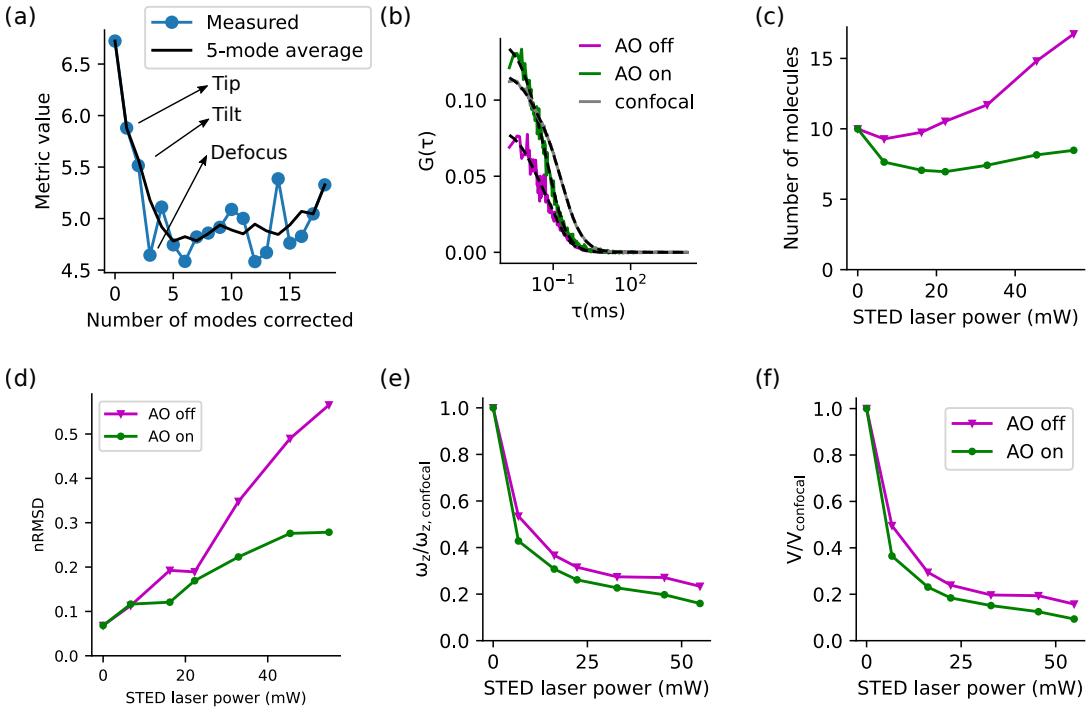

Figure 6.3: Aberration correction for z-STED-FCS diffusion measurements of Abberior Star Red in water:glycerol solution, measured 3 µm above the coverslip. (a) Evolution of the quality metric during aberration correction (blue dots) and rolling average over 5 modes (black line) with number of modes corrected. The name of the first three modes corrected are indicated by arrows. (b) FCS curves obtained in confocal (gray) and at a STED laser power of 55 mW without (magenta) and with (green) aberration correction. Dashed black lines: fits. (c-f) Evolution of (c) average number of molecules in the observation volume, (d) normalised fitting residuals (nRMSD), (e) axial size of the observation volume normalised with confocal value $\omega_z/\omega_{z,confocal}$ and (f) size of the observation volume normalised with confocal value $V/V_{confocal}$ with STED laser power, with (green) and without (magenta) aberration correction.

the decrease in quality metric with number of modes corrected, we found that most of

the improvement came from the correction of the first modes (tip, tilt and defocus: Figure 6.3(a)). In this configuration, we expected only spherical aberrations and it was therefore surprising that the most impactful modes to correct were tip, tilt and defocus. The presence of tip and tilt could be attributed to either initial miscalibrations, perhaps due to the sensitivity to misalignments of STED-FCS being higher than that of STED imaging, or to drift that occured after initial microscope calibration, which we observed in chapter 5. Correction of defocus probably in part accounted for the effects of spherical aberrations, that shift excitation and depletion foci differently [109]. Having removed aberrations with the determination of a stable correction, we could quantify the improvements brought by aberration correction. To do this, we acquired a set of 30s long measurement, with and without aberration correction and at different STED laser powers. Improvements due to AO were readily visible upon inspecting the FCS curves, which exhibited with AO-STED-FCS a higher amplitude than both confocal curves and STED-FCS curves without aberration correction (Figure 6.3(b)). Fitting the curves revealed a spectacular reduction in the average of number of molecules in the observation volume (Figure 6.3(c)), which can be linked to either lower levels of undepleted background [95] or to a smaller size of the observation volume. As a means of measuring background noise in FCS curves, we measured the root-mean-square of the fitting residuals normalized to the amplitude (nRMSD) [150] (Figure 6.3(d)). As expected, residuals were higher in presence of aberrations. Perhaps the most important parameter of all, we could estimate the increase in axial size of the observation focus ω_z from the changes in transit times:

$$\frac{\omega_z}{\omega_{z,confocal}} = \frac{K\left(\tau_{xy}/\tau_{xy,confocal}\right)}{K_{confocal}}\sqrt{\frac{\tau_{xy}}{\tau_{xy,confocal}}} \tag{6.6}$$

where $K\left(\tau_{xy}/\tau_{xy,confocal}\right)$ refers to the aspect ratio calibrated as described in section 6.2. Comparing axial resolution with and without aberration correction, we found improve-

ments with AO (Figure 6.3(e)), however not as important as the improvements in noise or number of molecules. Because z-STED improves not only axial but also lateral resolution, an interesting parameter to compare is the relative variation in observation volume, defined as:

$$\frac{V}{V_{confocal}} = \frac{K\left(\tau_{xy}/\tau_{xy,confocal}\right)}{K_{confocal}} \left(\frac{\tau_{xy}}{\tau_{xy,confocal}}\right)^{\frac{3}{2}} \tag{6.7}$$

This has furthermore the advantage to allow comparison between results obtained with different confinement modes, for instance with 2D-STED. Observation volumes were accordingly smaller with adaptive optics, to reach a 10-fold improvement in observation volume (Figure 6.3(f)), comparable to the maximum resolution improvements obtained with 2D-STED in aqueous solution [57].

6.4.2 AO extends the range of observation depths for STED-FCS in solution

One of the goals of adaptive optics is the correction of depth-induced aberrations to allow measurements in thick samples. To demonstrate this, we performed STED-FCS experiments in the same solution of Abberior StarRed, at increasing focusing depth. We changed the focusing depth from 3 to 15 µm, expecting increasing amounts of spherical aberrations being caused by the refractive index mismatch between the immersion oil of the objective and that of the solution. Correction at each depth was started from the correction at the previous depth: for instance, the correction procedure at 9 µm was started from the correction measured at 6 µm. This facilitated the aberration correction process as it limited the maximum amount of aberrations needed to correct in each round. In our system, we could correct only aberrations in the depletion beam, and the quality of the

excitation and detection paths degraded with focusing depth. To account for this in the aberration correction process, we increased the acquisition time of sensorless measurements from 3s at 3 µm to 12s at 15 µm.

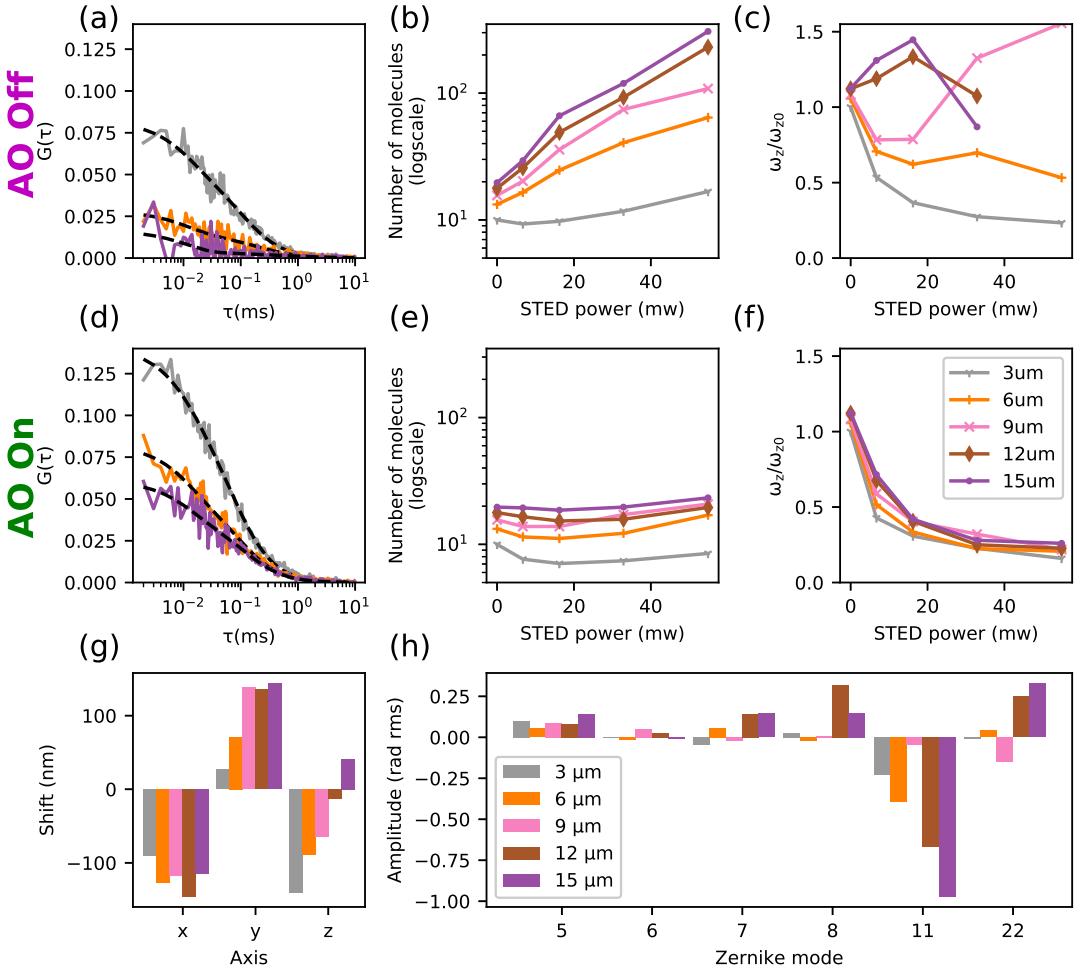

Figure 6.4: AO correction of depth-induced aberrations in z-STED-FCS measurements: diffusion of Abberior Star Red in a water:glycerol solution. (a,d) FCS curves at a STED laser power of 55 mW, (b,e) average number of molecules in the observation volume and (c,f) axial size of the observation volume normalised with confocal value $\omega_z/\omega_{z,confocal}$ without (a-c) and with (d-f) aberration correction, acquired at different depths as indicated in the legend in panel (f). (g-h) Shifts of the depletion pattern (g) and amount of Zernike modes (h) measured during the sensorless procedure at different depths as indicated in panel (h).

After aberration correction, we acquired at each depth 30s-long intensity timetraces at four different STED laser powers, and with the AO correction on and off. The visual inspection of FCS curves (Figure 6.4(a,d)) immediately revealed a spectacular improvement in the quality of FCS curves thanks to AO. This was confirmed by the extraction of the average number of molecules in the observation volumes (Figure 6.4(b,e)), which was up to an order of magnitude larger without AO. This revealed dramatic reductions in signal levels in presence of aberrations. Extracting the axial size of the observation volume from the results of the fits (Figure 6.4(c,f)), we found that the resolution was massively improved thanks to AO. Perhaps more importantly, AO allowed to obtain quantitatively similar results at every depth, while the parameters extracted without AO were severely biased as focusing depth increased. Besides, extraction of transit times from STED-FCS data without AO was impossible at high focusing depth and high STED laser powers due to insufficient signal levels. Analysing the aberrations measured at each depth, we found significant amounts of tip, tilt and defocus (Figure 6.4(g)). The first two were caused by thermal and mechanical drift. In particular, drift along the y axis increased with focusing depth but was actually drifting over time (as we started experiments at 3 µm and progressively increased focusing depth). Changes in defocus (z axis) were likely caused by different shifts between excitation and depletion beams caused by spherical aberrations. The main aberrations we measured were primary and secondary spherical (Figure 6.4) that increased linearly with depth, except at 9µm where the correction routine converged towards a different local extremum. This did not affect the STED-FCS performance (Figure 6.4(e-f)).

6.4.3 Aberration correction in living cells

Having demonstrated aberration correction for STED-FCS in solution, we then further tested our method on a biological system. We measured for this the 3D diffusion of GFP expressed in the cytoplasm of transgenic cells labelled with a 647SiR SNAP tag, as described in the methods section (Figure 6.5(a)). In solution, the pool of fluorophores was large and reduction of the number of available fluorophores due to photobleaching was not an issue. However, cytoplasms had a much lower volume and therefore photobleaching during experiments limited the maximum achievable measurement times. Besides, minimising the overall light dose limits the risks of phototoxicity, therefore we decided to correct less aberration modes than in solution. We found little to no astigmatism in preliminary measurements, so we decided to not correct these modes.

We first performed a set of aberration measurements at depths comprised between 2 and 6 µm in the cytoplasm. As expected, spherical modes were dominant (Figure 6.5(b-c)). We measured relatively low amplitude of aberrations (0.4 rad rms maximum, as opposed to 1 rad rms deep in solution as shown in Figure 6.4(h)). Considering the high amount of crosstalk between primary and secondary spherical modes that complicate the aberration correction process, we further decided to not correct secondary spherical aberrations. With this smaller subset of modes, we could reliably correct aberrations at a depth of approximately 4µm in a living cell and assess the improvements brought by AO (Figure 6.5(d)). We acquired for this a series of FCS curves at different STED laser powers and in confocal mode. FCS curves were acquired alternatively with and without AO to ensure that any effect observed was not due to photobleaching or phototoxicity. Curves were recorded with a 5s acquisition time, and the effects of photobleaching within each acquisition were mitigated using the local averaging method [151]. Due to the crowded

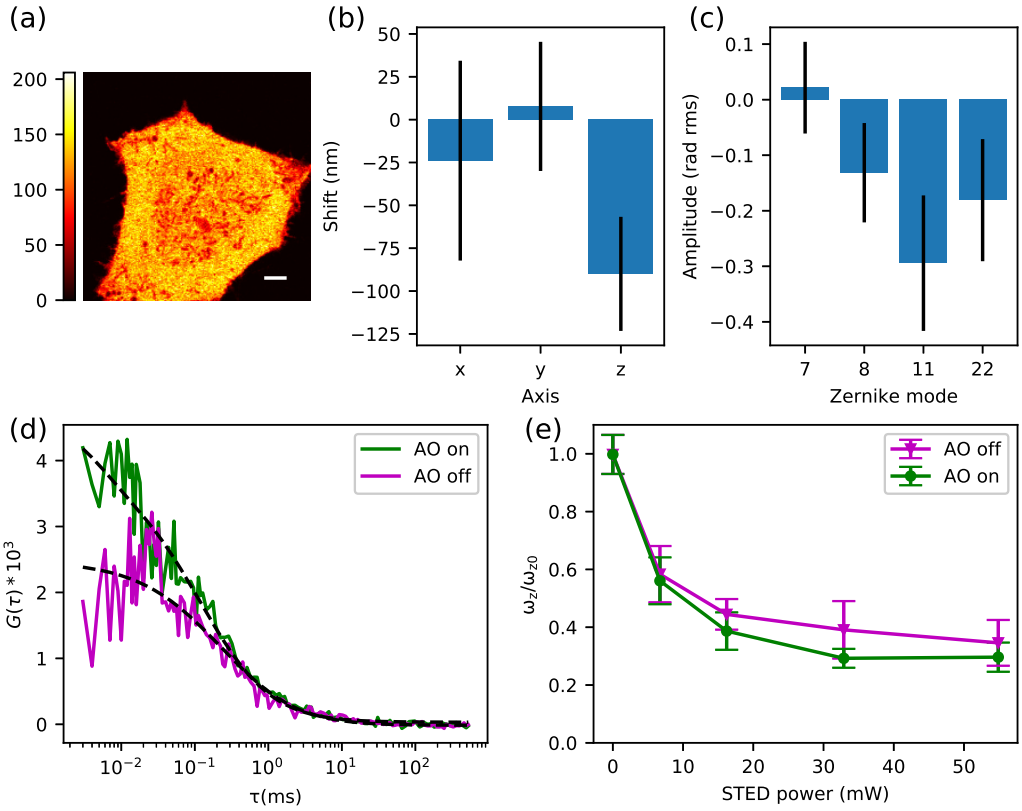

Figure 6.5: Aberration correction for STED-FCS in the cytoplasm of living cells. (a) Lateral picture of a cell where STED-FCS experiments were performed. Scale bar: 5 µm. (b-c) Spatial shifts of the depletion pattern and (c) amount of Zernike modes measured in the cytoplasm of living cells at 2-6 µm depth. Mean +/- s.d, n=17 measurements in 15 cells, 1-2 measurement per cell.

environment of the cell cytoplasm, we found that the resulting FCS curves were best fit with a subdiffusive model, and we set the α parameter in equation 6.1 to $\alpha = 0.75$, a value previously reported in the cytoplasm [149]. As in solution, we found that the axial resolution was improved by AO (Figure 6.5(e)). Using the average number of molecules in the observation volume measured in confocal recordings, we could estimate the label concentration to be approximately 3 µM, comparable to previously measured values of cytoplasmic GFP (equal to 7 µM in ref [152]).

6.4.4 Biological application: measuring diffusion of peroxisomal membrane proteins

We later applied our technique as part of a wider biological investigation led by Dr Silvia Galiani on the diffusion modes of peroxisomal matrix proteins. Peroxisomes are ubiquitous organelles that fulfil many metabolic functions. They heavily rely on protein import from the cytoplasm to fulfil their functions, and as such it is important to understand protein import in peroxisomes. One of the key proteins in this process is the cargo receptor PEX5. To understand what are the interactions ox PEX5 with its environment, we used AO-z-STED-FCS to determine its diffusion properties at different scales. Particularly, previous FCS experiments found an unexpectedly slow diffusion for PEX5, which could have been caused by a transient interaction in the cytoplasm with the peroxisomal targeting signal sequence type 1 (PTS1).

To verify this, we used the capability of AO z-STED-FCS to measure diffusion speed at different lengthscales: in case of free diffusion, the apparent diffusion coefficient should be the same no matter the size of the observation volume, while the apparent diffusion coefficient decreases with observation volume size in case local trapping sites affect the diffusion. We measured the lengthscale-dependent diffusion speed in three samples: first, a control sample expressing cytoplasmic GFP labelled with SiRo, as in previous section. Second, we used a sample expressing a functional version of the protein PEX5, and third a sample expressing a defective version of PEX5, PEX5L S600W that could not interact with PTS1. Both PEX5 and PEX5L S600W samples were fused with eGFP and labelled with SiRo for STED-FCS. We corrected aberrations as described in the previous section. To minimise the aberration correction time and phototoxicity, we corrected aberrations once per microscope slide. The focusing depth was then fixed for all measurements in this slide.

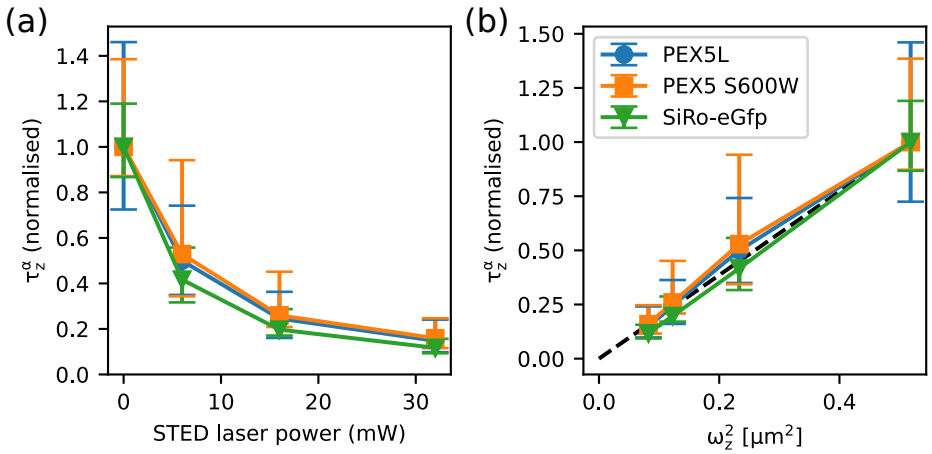

Figure 6.6: Diffusion of peroxisomal cargo receptor studied with STED-FCS. (a) Axial transit time as a function of STED laser power measured by STED-FCS in different samples as explicited in the legend of panel (b). (b) Variation of axial transit time with axial size of the observation volume determined from imaging of immobilised fluorescent beads, and compared with results expected for a free diffusion (black dashed line). Errorbars: mean +/- interquartile range, n=45 measurements in three independent samples.

We first analysed the decrease in axial transit time with STED laser power (Figure 6.6(a)). Axial transit times (set to the power alpha to be proportional to ω_z, see equation 2.12) decreased in all three samples similarly, indicating free diffusion in all cases. To further verify this, we compared the STED-dependent axial transit time with the square of the expected axial size of the observation volume, determined from imaging of immobilised fluorescent beads (Figure 6.6(b)). Proportionality in all three cases between τ_z^α and ω_z^2 once again revealed that the mode of diffusion was similar in all three samples, and that therefore the slow diffusion of PEX5 was not caused by measurable interactions with PTS1 in the cytoplasm.

6.5 Discussion and conclusions

In this chapter, we created a new method to correct aberrations that affect z-STED-FCS measurements. We demonstrated the performance and applicability of this method in a dyes solution as well as in cells, and we used it as part of a wider biological investigation on peroxisomal membrane proteins. This study of the PEX5 cargo receptor was one of the first STED-FCS investigations used to measure diffusion modes in the cytoplasm (see also the study of diffusion modes of tubulin in the cytoplasm in ref [64]) and we believe AO z-STED-FCS will be of use in a wide variety of context, for instance to study diffusion of fluorescent probes in biopolymers [153, 154] which are known to affect diffusion at different scales but which sub-diffraction properties diffusion could not be investigated.

Even at moderate focusing depths, we found that AO increased both signal levels and resolution. AO allowed z-STED-FCS to achieve similar performance at different focusing depth, which is of paramount importance for a quantitative technique. AO therefore increases the confidence obtained in STED-FCS measurements by removing the potential biases induced by aberrations. The improved focus quality obtained with AO allowed us to obtain an excellent 10-fold reduction in the observation volume with STED-FCS, which could be reached in the past only using organic solvents to minimise the refractive index mismatch (Table 6.1).

In previous implementations of z-STED-FCS in solution [55, 57], it was found that the average number of molecules in the observation volume increased with STED laser power due to uncorrelated background. Thanks to adaptive optics, we could substantially reduce these background contributions and observe a reduction in the number of molecules in the observation volume with STED laser power (Figure 6.3). This shows that previous implementations were limited by aberrations.

Medium	Method	Reduction in observation volume size
Aqueous	SPLIT-FLCS [64]	4
	z-STED-FCS [55]	5
	STEDD [27]	5
	2D STED-FCS [57]	10
	AO z-STED-FCS (Figure 6.3)	10
Organic	z-STED-FCS [57]	15
	2D STED-FCS [57]	25

Table 6.1: Reduction in observation volume size obtained from different STED-FCS approaches for 3D diffusion.

Appendix A: Comparison between fitting methods

We validated the new fitting method developed for this study, which fits the entire observation volume with a precalibrated shape, with the previous method in which the lateral transit time was fixed from confocal recordings and only the aspect ratio was varied[55]. To do this, we first compared the outcomes of fitting the same dataset (from section 6.4.1, with adaptative optics on) acquired in solution. In order to fairly compare the two, we calculated for both the measured observation volume, which turned out to be extremely close with both methods (Figure 6.7(a)). Fitting residuals were also extremely similar (Figure 6.7(b)). To verify the increased robustness of our methods against perturbations in the shape of FCS curves, we compared both fitting methods in STED-FCS curves obtained in cells that have a higher variability due to the heterogeneous cellular environment. Comparing once again the observation volumes measured in STED-FCS with each fitting method, we found sensibly similar results, except that outliers with absurd values of observation volume were found when fitting the aspect ratio. These artefacts were caused by divergence of the fitting method, which interestingly did not significantly change the shape of the fit (Figure 6.7(d-e)). This showed that fitting the observation volume with

prescribed shape was a more robust method than fitting the aspect ratio only.

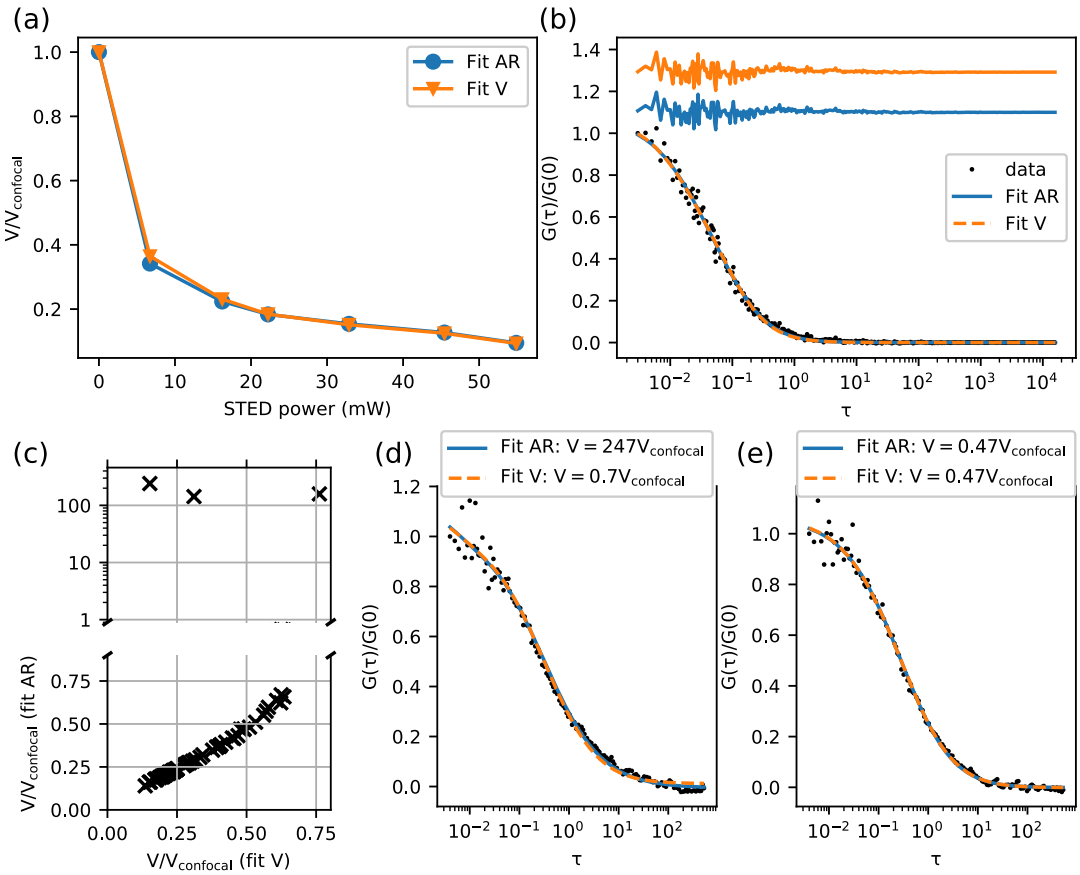

Figure 6.7: Comparison between fitting methods for STED-FCS, in solution (a-b) and in cells (c-e). (a) Effective observation volumes obtained by fitting AO z-STED-FCS data acquired in a solution of Abberior StarRed, by fitting either aspect ratio only ("Fit AR") or by fitting the observation volume with a prescribed shape ("Fit V"). (b) FCS curve obtained in solution with a STED power of 55 mW, and fits with the different methods. (c) Observation volumes measured in cells upon fitting the observation volume (x axis) or the aspect ratio (y axis). Outliers are represented on the top of the graph with a different scale. (d-e) FCS curves obtained in cells and fitted with both methods. (d) Representative curve that leads to divergence of the aspect ratio fitting method. (e) Representative curve that can be fitted with either method.

Chapter 7

Background reduction in STED-FCS using coherent-hybrid STED

Thanks to adaptive optics, we largely improved the resolution and signal levels of z-STED-FCS experiments in 3D, both in solution and in cells. A striking result of these experiments was however that even in absence of aberrations, the average number of molecules in the observation volume did not decrease at the same rate as the observation volume, suggesting that measurements were biased by spurious background contributions. Background in STED-FCS can have multiple origins, for instance collection of scattered STED laser photons by the detector or anti-Stokes excitation by the STED laser [155]. Anti-Stokes excitation occurs when fluorophores excited by the STED laser emit a photon of lower wavelength, allowed by extra energy coming for example from thermal excitation. A likely cause of background in our setup was the imperfect overlap between the excitation focus and the z-STED depletion pattern. Indeed, if the z-STED depletion pattern could efficiently deplete fluorescence in areas immediately around the centre of the observation volume, it did not cover up more distant areas. This effect was

previously observed in different optical setups [155] and we could readily observe it while imaging membranes (see for instance Figure 4.1 in chapter 4). It was also found that this undepleted background caused by imperfect overlap between excitation and depletion beams was the cause of the extremely poor performance of 2D-STED-FCS when measuring 3D diffusion [62]. Background reduction in STED-FCS could be achieved by filtering out undepleted photons based on their different lifetime with techniques such as stimulated emission double depletion (STEDD)[27], background substraction by polarisation switching (psSTED) [50] or separation of photons by lifetime tuning (SPLIT) [64]. Unfortunately, these techniques rely on assumptions on the fluorescence lifetime and are not well suited to samples with varying fluorescence lifetime. Physical suppression of the undepleted background is therefore preferable. This can be achieved using TIRF illumination [63] or supercritical angle detection [35], allowing however measurements only close to the coverslip. A more modular approach would consist of using an optimised depletion pattern that fully overlaps the excitation beam. 3D-STED, as a combination of the 2D- and z-STED depletion patterns, was used in an attempt to create such optimised depletion pattern, yet even in this configuration high background values were found in STED-FCS [57]. Recently, a novel depletion pattern was created using a bivortex phase mask [30]. In this configuration, named coherent-hybrid STED (CH-STED), the resolution was increased along all three dimensions and a substantial increase in contrast was observed when imaging dense three-dimensional samples. Expecting a similar decrease of background in STED-FCS, we tested and characterised the performance of STED-FCS in 3D with CH-STED. We compared the performances of CH-STED-FCS with those of the three most common confinement modes (2D-, z- and 3D-STED). We investigated using both simulations and experiments the spatial origins of background noise in STED-FCS for all four confinement modes and compared their performances in a wide variety of scenarios.

Thanks to the aberration correction procedure elaborated in chapter 6, we could on the one hand perform unbiased measurements and on the other hand measure the impact of aberrations on the performances of different confinement modes. We published the results presented in this chapter in a journal article [156] and the figures shown here were adapted from this publication.

7.1 Materials and methods

7.1.1 Samples

Dyes solution: Freely diffusing dyes in solution were prepared by diluting Abberior Star Red dyes (Abberior, Germany) to a concentration of 50 nM in a 1:1 water:glycerol solution. Glycerol was used to slow down diffusion speeds to facilitate the analysis of FCS data.

Fluorescent beads: Slides of immobilised 40 nm far-red fluorescent nanoparticles used for STED imaging were purchased from Abberior Instruments (Germany).

Supported lipid bilayers: Supported lipid bilayers were prepared as described in chapter 4

Cells: Cells transfected with a plasmid expressing a fusion protein of GFP and SNAP-tag were prepared as described in chapter 6.

7.1.2 FCS

FCS curves were either obtained directly from a correlator card (Flex02-08D, correlator.com) or by acquiring fluorescence intensity timetraces with a frequency comprised between 0.25 and 1 MHz that were correlated offline using the python package multiple-

tau [148]. Acquisition times were set to 10 seconds. Fitting FCS curves was performed using the standard model described in section 2.4.2. This model relies on the assumption that the observation volume is Gaussian, which we verified by imaging samples of fluorescent beads (see section 7.2). We recall here the most important equations. We used the three-dimensional diffusion model:

$$G_D(\tau) = \left(1 + \frac{T}{1-T}\exp^{-\tau/\tau_T}\right)\frac{1}{N}\frac{1}{1+(\tau/\tau_{xy})^{\alpha}}\frac{1}{\sqrt{1+\frac{1}{K^2}\left(\frac{\tau}{\tau_{xy}}\right)^{\alpha}}} \tag{7.1}$$

Where T refers to the triplet correlation amplitude, τ_T is the triplet correlation time, N is the average number of molecules in the observation volume, τ_{xy} is the average lateral molecular transit time in the observation volume, α is a correction factor to account for non-Brownian diffusion ($\alpha < 1$ corresponds to subdiffusion, $\alpha = 1$ to Brownian diffusion) and K is the aspect ratio. The aspect ratio was set to 4 in confocal recordings as discussed in chapter 6. In STED, we expected the value of the STED aspect ratio to change with STED laser power and with confinement modes, as different modalities increase preferentially either lateral or axial resolution. For this reason, we extended the methodology developed in chapter 6: for each confinement mode, we measured using images of immobilised fluorescent beads the relative variations of axial resolution with lateral resolution, approximated this relationship using an analytical expression (either linear or exponential function) and expressed the aspect ratio as a function of the relative decrease in lateral transit time with respect to confocal. The exact procedure is detailed in section 7.2.

We furthermore fixed several parameters in equation 7.1 in order to obtain reliable data fitting. In solution, triplet correlation times were determined by fitting confocal FCS curves acquired with a long (60s) acquisition time. Unlike in chapter 6, we also sought to fix the value of the triplet correlation time, due to the fastest lateral transit times (approx-

imately 50 µs) being close to the triplet correlation times, which in turn could have biased the determination of the lateral transit time. The triplet correlation time τ_T was found to be equal to 11 µs, higher than the usually reported value of 5 µs. We attributed this to interactions of the dye with the water/glycerol mixture we used, as opposed to pure water generally used. We determined the triplet correlation amplitude using the same approach. However, unlike triplet correlation time, triplet correlation amplitude varies with excitation laser power [150]. Therefore, we measured triplet correlation amplitude at the two excitation laser powers we used (8 and 17 µW) and found values of 0.16 and 0.25, respectively. The α parameter was set to 1, corresponding to Brownian diffusion.

In cells, we did not need to fix triplet correlation amplitudes thanks to longer lateral transit times. Triplet correlation time was set to 5 µs as previously used for the Silicon Rhodamine dye. The value of the α parameter was determined to be 0.8 by fitting a batch of confocal FCS curves. A summary of the values of FCS parameters used in this chapter can be found in table 7.1.

Sample	Excitation power	τ_T	T	α
Solution	8 µW	11 µs	0.16	1
	17 µW	11 µs	0.25	1
Cells	6 µW	5 µs	floating	0.8

Table 7.1: Summary of parameters used for FCS data fitting

In cells, we minimised the effects of cell-cell variations on the average number of molecules in the observation by normalising the amplitude of STED-FCS curves with that of confocal curves. In practice, the average number of molecules in the observation of each series of measurements (made of one confocal FCS and three STED curves at different STED laser power) was normalised with the confocal value.

As in chapter 6, we calculated the root-mean-square of the fitting residuals normalized to the amplitude (nRMSD), this time up to a lag time of 50 µs, smaller than most transit times.

7.1.3 Adaptive optics

Aberrations were corrected using the sensorless procedure described in chapter 6. Sample-induced aberrations were corrected prior to every measurement. Zernike modes 1-11 were corrected (including tip, tilt and defocus to optimise the position of the depletion pattern with respect to the excitation focus). The z-STED depletion pattern was systematically used for correction of modes 5-11 (as numbered in Table 2.1), no matter the confinement mode used later. Repositioning modes tip, tilt and defocus (modes 1-3) were corrected for each specific confinement mode, as residual coma aberrations might shift the centre of different depletion foci in opposite directions [134]. STED laser power was set to 16 mW during aberration correction procedures. Aberration amplitudes were measured in radians root mean square (rad rms, see section 2.5.2) and measured at 755 nm.

7.1.4 Simulations

The intensity distributions of the excitation and depletion lasers were calculated using the vectorial diffraction theory, as described in details in chapter 5. Intensity distribution were calculated in a two-dimensional (xz) grid with a 10 nm pixel size. They were integrated in cylindrical coordinates, using invariance along the azimuthal coordinate to calculate three-dimensional integrals. Wavelength was set to 755 nm for the depletion patterns and to 640 nm for excitation. The refractive index was set to 1.518 (oil) and NA to 1.4.

7.1.5 Determination of background in SLB

In section 7.3.2, we estimated the axially-varying background contributions in STED-FCS with different confinement modes using SLBs. To do this, we compared the relative variations in apparent number of molecules in the observation surface N with those of lateral molecular transit times τ_{xy}. Indeed, background noise biases the measurement of N with FCS, as follows [95]:

$$N = N_{real}\left(1 + \left(\frac{1}{SBR}\right)^2\right) \tag{7.2}$$

where N_{real} is the actual average number of molecules in the observation surface and $SBR = I_{signal}/I_{background}$ is the ratios between intensity of correlating photons and that of background photons. N_{real} can also be expressed a function of molecular concentration c and size of the observation surface S as:

$$N_{real} = cS = c\pi\omega_{xy}^2 \tag{7.3}$$

where ω_{xy} is the $1/e^2$ radius of the Gaussian observation area. The concentration c is unknown but does not need to be determined. Indeed, equation 7.3 can be simplified as:

$$\frac{N_{real}}{N_{real,0}} = \left(\frac{\omega_{xy}}{\omega_{xy,0}}\right)^2 \tag{7.4}$$

where $N_{real,0}$ is the average number of molecules in the observation area when the SLB is in focus. Under the reasonable assumption that no undepleted background contributions were present at z=0, $N_0 = N_{real,0}$. ω_{xy} can be indirectly measured with the molecular transit time, as $\tau_{xy} = \dfrac{\omega_{xy}^2}{4D}$. Therefore, equation 7.4 can be rewritten as:

$$N_{real} = N_0\frac{\tau_{xy}}{\tau_{xy,0}} \tag{7.5}$$

Replacing equation 7.5 in equation 7.2, we can calculate the signal-to-background ratio (SBR) at each depth:

$$SBR = \sqrt{\frac{N_0 \tau_{xy}/\tau_{xy,0}}{N - N_0 \tau_{xy}/\tau_{xy,0}}} \tag{7.6}$$

This expression relies on the assumption that $N > N_0 \tau_{xy}/\tau_{xy,0}$, which is in theory verified if no background is present at z=0 (see equation 7.2). However, in presence of low background values, statistical variations could induce values of N to be smaller than $N_0 \tau_{xy}/\tau_{xy,0}$. In these cases, both quantities were set to be equal and the SBR was considered infinite. The absolute size of observation surface was determined using:

$$\omega_{xy} = \omega_{xy,0,confocal} \sqrt{\frac{\tau_{xy}}{\tau_{xy,0,confocal}}} \tag{7.7}$$

where $\omega_{xy,0,confocal}$ is the confocal $1/e^2$ radius at z=0, determined from imaging of immobilised fluorescent beads to be equal to 102 nm (corresponding to a FWHM of 240 nm). The xz profile of observation volumes could then be reconstructed as:

$$g(x, y, z) = I(z) \exp\left(-\left(x^2 + y^2\right)/\omega_{xy}(z)^2\right) \tag{7.8}$$

where $I(z)$ is the depth-dependent average photon counts. Using the numerical value of SBR calculated in equation 7.6, we could calculate the average photon counts contributing to the correlation:

$$I_{signal}(z) = \frac{I(z)}{1 + 1/SBR} \tag{7.9}$$

as well as the average photon counts contributing to background:

$$I_{background}(z) = \frac{I(z)}{1 + SBR} \tag{7.10}$$

7.2 Imaging immobilised fluorescent beads with different STED confinement modes

7.2.1 STED observation volumes are Gaussian for each confinement mode

We investigated the performances of in total 4 confinement modes: 2D-, z-, CH- and 3D-STED. The first three were generated using a phase mask created by the SLM, while 3D-STED was created as an overlay of a SLM-generated z-STED pattern and a phase-plate-generated 2D-STED pattern. We initially set the value of the inner radius of the CH-STED phase mask to 0.8, corresponding to 80% of the pupil radius size. For 3D-STED, 80% of the STED laser power was in the z-STED arm and 20% in the 2D-STED, except for measurements in cells where 50% of the STED laser power was sent through each arm. We first inspected the capability of our SLM to create all three different depletion patterns by scanning the depletion beam through a sample of scattering gold beads and collecting the scattered light with a PMT (Figure 7.1(a)). We found that all four depletion patterns could be created without obvious distortions, thanks to the calibration protocol developed in chapter 3.

We then imaged a sample of immobilised 40nm fluorescent beads to observe the intensity distributions of the different observation volumes. This information is particularly critical for FCS applications, in which assumptions on the shape of these intensity distributions (e.g Gaussian or Lorentzian) have to be made to fit FCS curves. For each STED confinement mode and at four different STED laser power as well as in confocal, we acquired a 3D stack of fluorescent beads, from which 10 single beads were localised. Axial intensity profiles were extracted (Figure 7.1(b)) and used to determine the shape (Gaus-

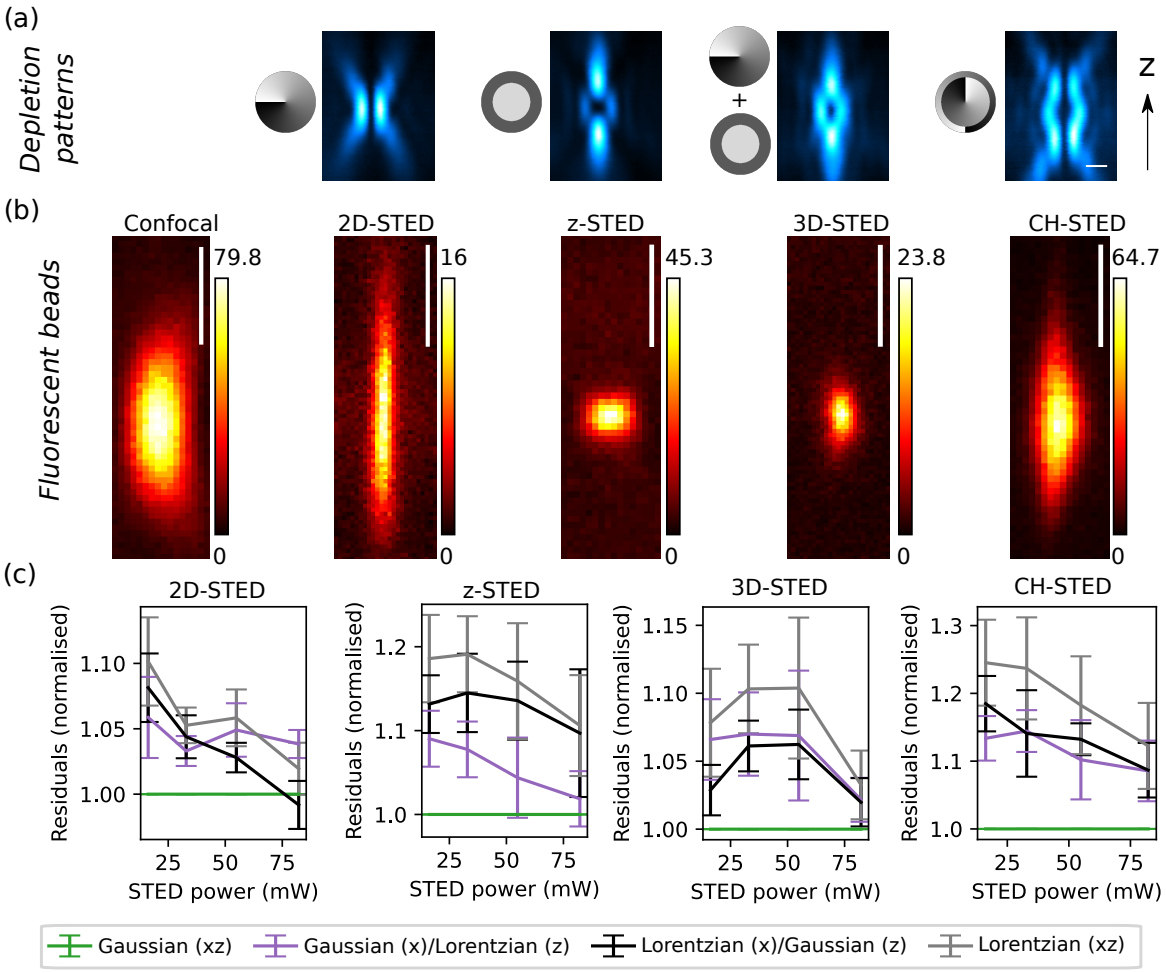

Figure 7.1: Shape of confocal and STED intensity profiles determined from immobilised fluorescent beads. (a) STED depletion patterns used in this chapter imaged using a sample of scattering beads (right) and phase masks used to create them (left, black to white corresponding to 0 to 2πphase modulation). 80% of depletion intensity was in the z-STED arm for 3D-STED. (b) Axial images (average of 10 different images) of immobilised fluorescent beads in confocal and with different STED confinement modes. STED laser power: 82 mW, scale bars: 500 nm. (c) Goodness of fit of two-dimensional fluorescence intensity profiles with Gaussian or Lorentzian distributions, measured as fitting residuals normalised with residuals obtained with Gaussian fits. Axial (z) and lateral (x) intensity profiles were fitted with either Gaussian or Lorentzian models as indicated in the legend below. mean +/- s.d, n=10.

sian or Lorentzian) of the corresponding observation volumes. For this, we fitted the intensity profiles with two-dimensional ellipsoids having either Gaussian or Lorentzian profiles along the lateral and axial dimension. We estimated the goodness of fit of each of these four models as the fitting residuals, normalised with those obtained with a full Gaussian fitting function (Figure 7.1(c)). Results showed that fitting residuals were overwhelmingly lower (denoting a better fit) with the full Gaussian model, with the exception of 2D-STED at highest STED laser power (82 mW). This latter exception was slightly better described with a Lorentzian profile along the lateral direction, as was previously found in 2D-STED. Nevertheless, our results showed that STED observation volumes with each confinement modes were accurately described by a two-dimensional Gaussian function. Besides, looking at the average brightness of beads with each confinement mode (Figure 7.1(b)), we could readily observe that z-STED and CH-STED exhibited better signal levels than 2D-STED and 3D-STED, suggesting that better signal levels could also be obtained in STED-FCS with these confinement modes.

7.2.2 Calibration of STED aspect ratios for different confinement modes

In chapter 6, we calibrated the relationship between the increase in lateral and axial resolution with STED laser power using images of fluorescent beads. In order to reliably fit FCS curves obtained with each confinement mode, we extended this methodology to all four confinement modes. For this, we used the dataset of 3D stacks of fluorescent beads described in the previous section and fitted axial intensity profiles with two-dimensional Gaussian ellipsoids to extract their lateral ω_{xy} and axial ω_z $1/e^2$ radius (Figure 7.2(a)). We fitted the relationship between ω_{xy} and ω_z (both decreasing as the resolution increased

with increasing STED laser power) with a heuristic function, either exponential or linear to obtain an analytical description of aspect ratio of the observation volume. Lateral and axial sizes were normalised with confocal values: confocal images of fluorescent beads had an average lateral FWHM of 225 nm and axial FWHM of 621 nm. Thus in Figure 7.2(a), at highest STED laser power, z-STED ($\omega_{xy}/\omega_{xy,0} = 0.7$ and $\omega_z/\omega_{z,0} = 0.22$) images had lateral and axial sizes of respectively 157 and 137 nm. 3D-STED and CH-STED are parametric depletion patterns: their performances can be tuned, respectively by changing the amount of energy going in the 2D and z-STED arm and by changing the inner radius ρ of the bivortex phase mask. We therefore acquired datasets of fluorescent beads with different values of these parameters in order to obtain a fitting model for every situation. When necessary, the parameters of the fitting model were interpolated: for instance, the relationship between ω_{xy} and ω_z for CH-STED with a radius $\rho = 0.85$ was interpolated from the values of the model for $\rho = 0.8$ and $\rho = 0.9$.

From this, we obtained an analytical formula of the aspect ratio K as a function of the variation in lateral resolution $\omega_{xy}/\omega_{xy,confocal}$, which we could use in our FCS fitting model (Figure 7.2(b)). Confocal aspect ratio was set to a value of $K = 4$, higher than the measured value of 2.8 to account for residual system and specimen aberration that distort and elongate the observation volume in FCS but not when imaging fluorescent beads. With all STED confinement modes excepted 2D-STED, we assumed that these axial elongations were depleted even at minimal STED laser power, therefore leading to a discontinuity between STED and confocal aspect ratios (Figure 7.2(b)). In 2D-STED, instead, these contributions along the optical axis could not be depleted and the relatively larger aspect ratio was used in confocal as well as in STED.

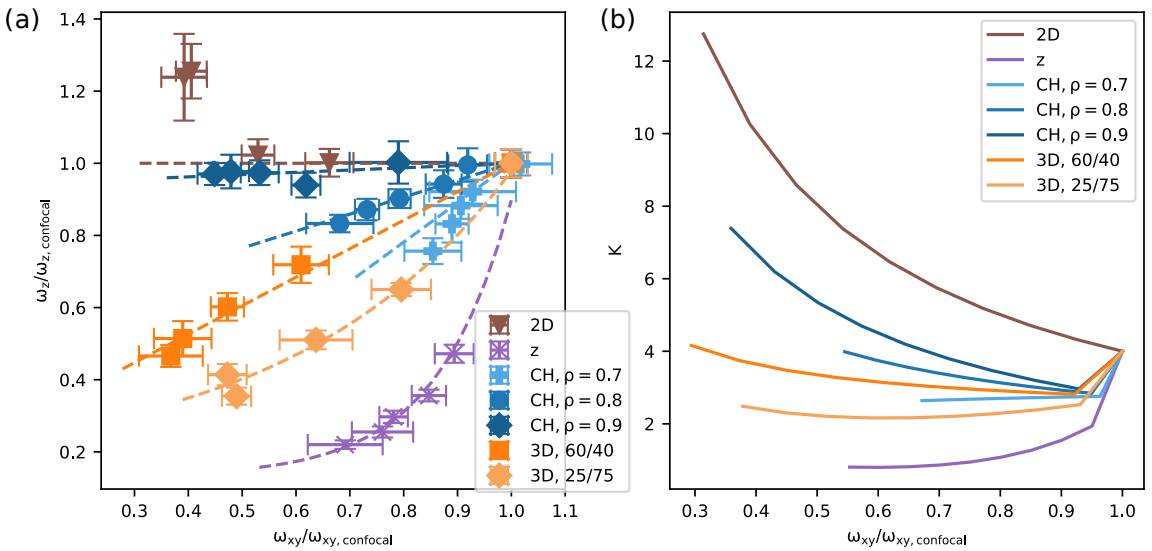

Figure 7.2: Calibration of aspect ratio variations for different STED confinement modes. (a) Relative axial ω_z and lateral ω_{xy} resolution variations for different STED confinement modes with STED laser power using fluorescent beads normalised with confocal values (mean +/- std, n = 10 beads per datapoint). For 3D-STED, the fraction of energy going in each arm (2D/z) is specified in the legend and for CH-STED, the inner radius of the phase mask ρ is specified in the legend. (b) Aspect ratio K as a function of lateral ω_{xy} $1/e^2$ radius normalised with its confocal value, determined from the fits to the data in panel (a) and used to fit STED-FCS data.

7.3 Origin of background in 3D STED-FCS

7.3.1 Simulations

Having determined the shape and aspect ratios of STED observation volumes, we then investigated the spatial origins of background in STED-FCS. In 2D-STED, this was previously achieved using simulations [62], which revealed that poor signal-to-background ratios were caused by a varying axial cross-section of the 2D-STED PSF and by low-intensity contributions that damp the amplitude of the FCS curves.

Using a similar methodology, we extended this study to the different STED confine-

ment modes we used in this chapter. We simulated axial intensity profiles of the STED confinement modes as well as of the excitation laser using vectorial diffraction theory as explained in chapter 5. As in reference [62], we assumed that low-intensity contributions did not contribute to the correlating signal and that they are therefore a source of background noise. In practice, we visualised these contributions in simulations using an arbitrary threshold set to $1/e^2$ of the maximum intensity (Figure 7.3, left). In order to minimise computing power, we calculated only 2-dimensional (rz) intensity profiles of the STED and confocal PSFs. In this representation, however, all pixels do not contribute to the total intensity equally: pixels far away from the optical axis correspond to a larger volume than those closer to the optical axis. Indeed, in cylindrical coordinates (Figure 7.3(a)), a volume element can be calculated as:

$$dV = r\, d\theta\, dr\, dz \tag{7.11}$$

and as a result a volume element dV far from the optical axis (large r) is larger than an element close to the optical axis (small r). For this reason, we also integrated the results along the azimuthal axis (Figure 7.3, right), which in effect corresponded to a multiplication of the value of every pixel by its radial coordinate r. This latter visualisation revealed important low-intensity contributions far away from the optical axis in 2D-, z- and 3D-STED in areas of poor overlap between excitation and depletion beams. Overlaying the simulated intensity distributions with contour plots of the corresponding depletion patterns confirmed that low intensity background was predominantly present in areas of low intensity of the depletion pattern. Thanks to an excellent overlap between excitation and depletion, CH-STED exhibited on the contrary low background contributions across the entire volume.

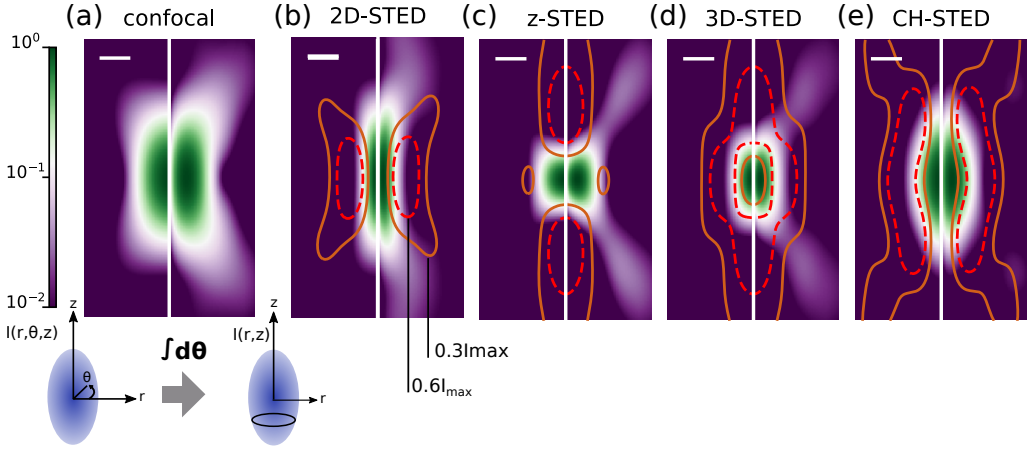

Figure 7.3: Spatial origin of signal and background in STED-FCS visualised with simulations. (a) Visualisation of the intensity distribution within a confocal observation volume, of an axial cross section (left) and integrated across the azimuthal axis (right). Signal values (comprised between 1 and $1/e^2$) were represented in green and background values (comprised between $1/e^2$ and 10^{-2}) in purple as indicated by the colorbar. (b-e) Visualisation of intensity distributions of (b) 2D-STED, (c) z-STED, (d) 3D-STED and (e) CH-STED as in panel (a). Contours (at 30 and 60% of the total intensity) of the depletion patterns are overlaid in red. Scale bars: 200 nm.

7.3.2 Experimental estimation of background

Having predicted the spatial origins of background using simulations, we then verified these predictions experimentally. To do this, we used a sample of SLBs, a single layer of freely diffusing lipids, as explained in chapter 4. For each confinement mode, we performed FCS measurements at various axial positions of the focus to measure both average molecular transit time in the observation surface τ_{xy}, average number of molecules in the observation surface N and average photon count I (Figure 7.4(a)). Readily in imaging, undepleted sidelobes were visible with z-STED and not with CH-STED (Figure 7.4(b)), auguring better background reduction with CH-STED. To quantitatively estimate depth-dependent background contributions, we compared the evolution of N and τ_{xy} (propor-

tional to the size of the observation surface). In absence of background, both should be proportional, while in presence of uncorrelated background N increases and τ_{xy} does not change. Under the reasonable assumption that no undepleted background was present at z=0 (SLB in the focal plane of the objective), we could calculate at each depth the SBR using the formula (see the methods section for derivation):

$$SBR = \sqrt{\frac{N_0 \tau_{xy}/\tau_{xy,0}}{N - N_0 \tau_{xy}/\tau_{xy,0}}} \tag{7.12}$$

Using this method, we could extract for different observation foci a series of parameters (Figure 7.4(c-f)): first, we could estimate the shape of the observation volume (left). For this, lateral transit times were used to estimate lateral size of the observation volume and total intensity at each depth was used to estimate axial size of the observation volume. Second, knowing total intensity and SBR, we could calculate at each depth the amount of signal and background (see equations 7.9-7.10 in methods section). In confocal (Figure 7.4(c)), we found negligible undepleted background as expected thanks to the 1 Airy Unit pinhole filtering out most background light. We found however that the intensity profile was slightly Lorentzian. This was explained by residual aberrations in the excitation focus, like coma, which distort the focus. When imaging point-like objects (fluorescent beads), this did not lead to a significant change in the shape of the axial intensity distribution. However, upon imaging extended objects like SLBs, these distortions add up and lead to an axial enlargement of the intensity profile. High background noise was measured in 2D-STED from distances of 300 nm to the focal plane, with even more significant background values appearing after 750 nm. These distances correspond to those we observed in simulations. Besides, we measured the axial FWHM of the 2D-STED depletion pattern using images acquired with scattering gold beads (see Figure 7.1(a)). We found that this

axial FWHM was equal to 900 nm, corresponding to a drop of depletion intensity by half at a distance of 450 nm from the optical axis. The increase in uncorrelated background contributions at distances to the focal plane between 300 and 750 nm could therefore be associated with a decrease in depletion intensity. z-STED (Figure 7.4(e)) exhibited in comparison much smaller background contributions, with the main background source being located around 800 nm from the focal plane, in undepleted sidelobes that can readily be seen in imaging (Figure 7.4(b)). The high depth at which these lobes can be found suggest that they are likely amplified by the axial elongation observed in confocal, suggesting that quality of the excitation focus is critical to the quality of STED-FCS measurements. Nevertheless, these sidelobes were consistently reported across a wide variety of systems [26, 30, 155], suggesting that they were not an artefact of our system. In comparison, CH-STED (Figure 7.4(f)) exhibited much lower background levels, despite some background remaining at focusing depths higher than 500 nm, probably caused by the low intensity of the CH-STED depletion pattern at these depths close to the optical axis.

To conclude, both simulations and experimental results showed that background occurs in areas of poor overlap between excitation and depletion, and that CH suppresses it the most efficiently. We therefore proceeded with experiments of 3D diffusion measured with STED-FCS to verify these predictions.

7.4 Results

7.4.1 Influence of CH radius parameter

The inner radius (parameter ρ) of the CH-STED phase mask can be changed to vary the shape of the CH-STED depletion pattern (Figure 7.5(a)). This in turn affects the shape

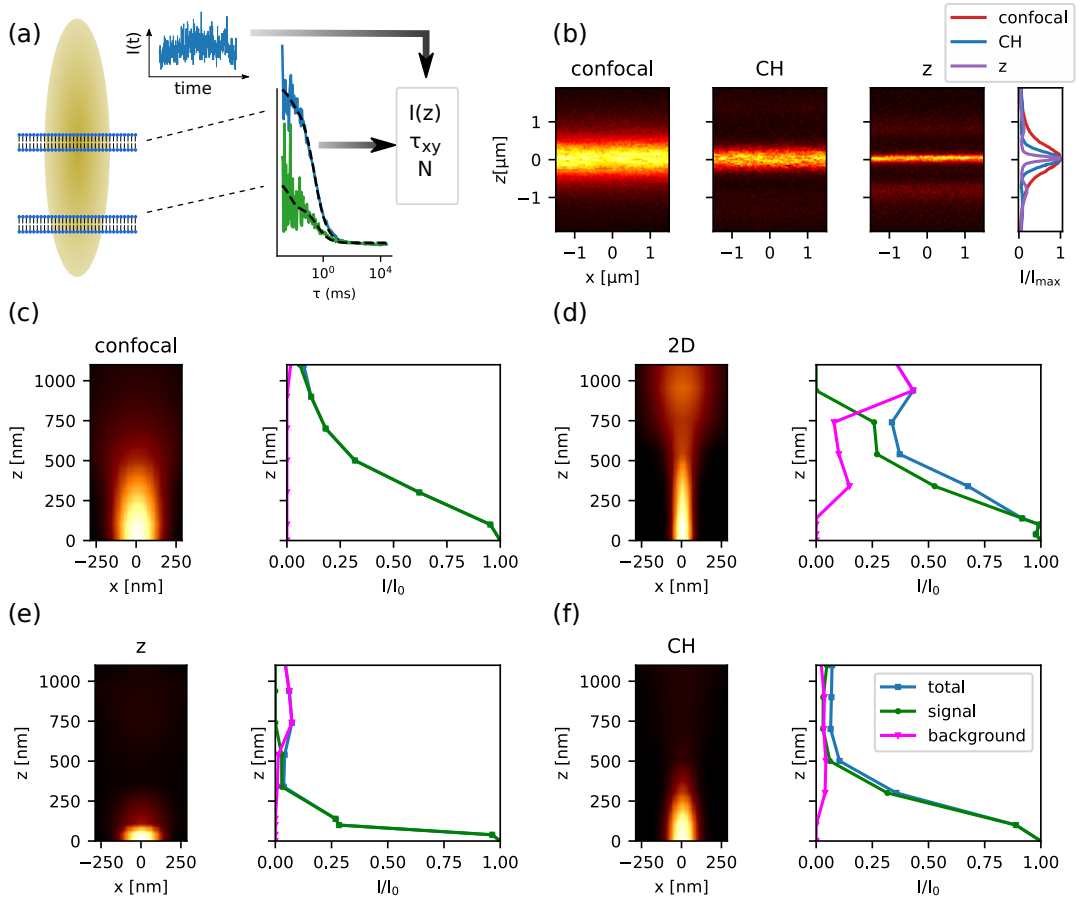

Figure 7.4: Experimental determination of spatial distribution of background using SLBs. (a) Scheme of the experiment: STED-FCS experiments in SLBs are performed at different axial positions of the focus to extract at each position the total photon counts I, average molecular lateral transit time τ_{xy} (as a measure of size of the observation surface) and average number of molecules N in the observation volume. (b) Axial images of SLBs imaged in confocal, CH- and z-STED modes. Right: normalised intensity profiles. (c-f) Left: axial reconstruction of observation volumes of confocal (c), 2D- (d), z- (e) and CH-STED (f) from FCS data in SLBs. Right: axial distributions of total intensity (blue), signal (green) and background (magenta) as indicated in the legend of panel (f).

of the observation volume. In practice, a higher value of the parameter ρ corresponds to lower axial resolution and higher lateral resolution, the extreme case being $\rho = 1$, corresponding to 2D-STED. In order to assess the performance of CH-STED with different values of the ρ parameter, we used a solution of freely diffusing Abberior Star Red in a 50:50 water:glycerol mixture. We added glycerol to the solution to increase the viscosity and reduce the diffusion coefficient in order to keep average molecular transit times larger than triplet correlation times even at high STED laser power. We performed STED-FCS experiments for values of the ρ parameter ranging from 0.7 to 1 in steps of 0.05, at two different STED laser powers (16 and 32 mW) to ensure that any effect observed was not power-specific. We also recorded confocal curves, from which confocal transit time was extracted for use in the fitting method (described in section 7.2.2). We also used values of N and τ_{xy} from confocal recordings to normalise results.

A visual inspection of the resulting FCS curves (Figure 7.5(b)) revealed that FCS curves obtained with a low ρ value had higher signal levels (as shown by less variations of the curve around its average value) and lower resolution (as shown by a shift of the curve towards longer lag times). In order to quantitatively assess the performances of CH-STED with different ρ parameters, we fitted the FCS curves to extract their average number of molecules in the observation volume and average molecular transit times. Because the shape of the observation volume varied with the value of the ρ parameter, as described in section 7.2, variations in resolution were best compared using the observation volumes instead of the lateral transit times. As expected, we found that observation volumes were smaller with high ρ parameters and that highest resolution was obtained with $\rho = 1$ (2D-STED). On the contrary, average number of molecules in the observation volume were smaller with low ρ parameters (Figure 7.5(d)), most likely due to a reduction in background noise. To verify this, we plotted together the relative variations of N and V, which should

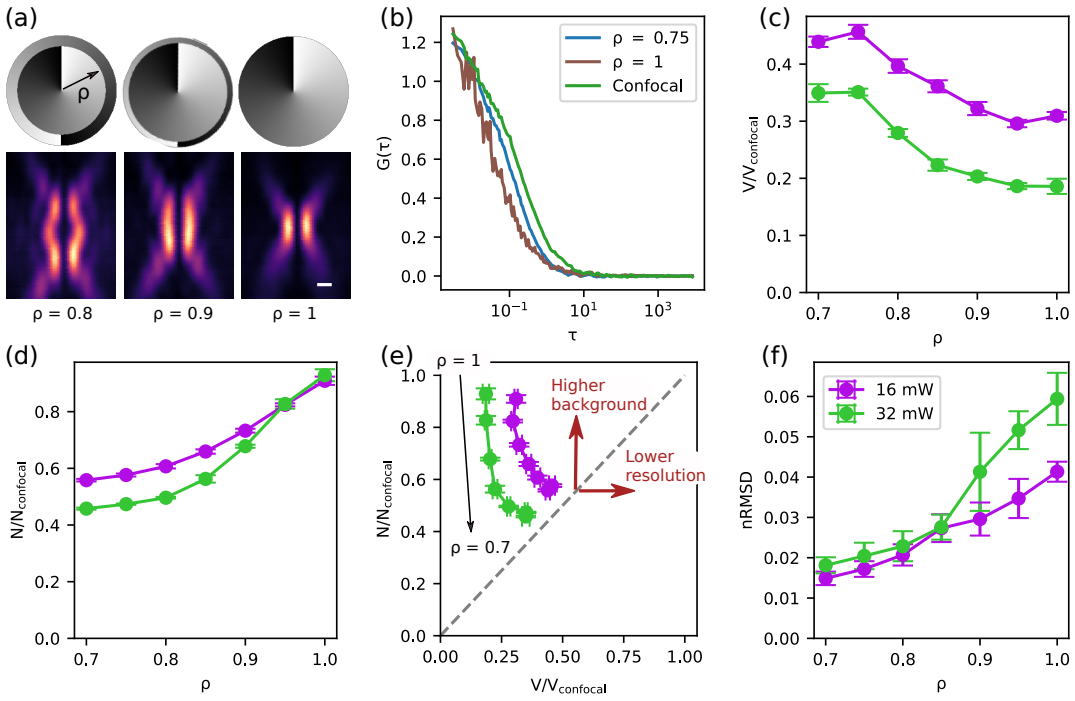

Figure 7.5: Influence of inner radius parameterm ρ on STED-FCS performance in a solution of Abberior StarRed dyes. (a) Tuning the inner radius ρ of the bivortex phase mask (top) affects the shape of the depletion pattern (bottom, imaged with scattering gold beads, scale bar: 300 nm). (b) Normalised confocal FCS curves obtained in a solution of Abberior StarRed and STED-FCS curves with different values of the parameter ρ, as indicated in the legend and at a STED laser power of 32 mW. (c,d) Extraction of (c) V and (d) N for different values of the parameter ρ from fitting FCS curves, normalised with confocal values and at two different STED laser power as shown in the legend in panel (f). (e,f) Estimation of background contributions in CH-STED as a function of the parameter ρ, determined from (e) pairwise N vs V plots (gray line: proportionality between N and V occurring in absence of background) and (f) fitting residuals normalised with curve amplitude (nRMSD), with higher fitting residuals indicating higher noise levels.

be proportional in absence of background (Figure 7.5(e)). This confirmed that minimum background contributions were obtained with low ρ parameters. As an alternative measure of background, we used root-mean-square of the fitting residuals normalized to the amplitude (nRMSD)(Figure 7.5(e)), which confirmed that lower ρ values lead to better suppression of background. As a result, we found a tradeoff between background suppression and resolution in the optimisation of ρ. Throughout the rest of this paper and unless specified otherwise, we will use the intermediate value of $\rho = 0.85$, which was previously used in CH-STED [30].

7.4.2 Comparison between STED confinement modes in solution

Having determined an optimal inner radius for the CH-STED phase mask, we then compared the performance of CH-STED with that of the other confinement modes. We used for this the same solution of freely diffusing Abberior StarRed in water:glyerol. As expected, FCS curves exhibited the highest amplitude with CH-STED, followed by z-STED, 3D-STED and 2D-STED (Figure 7.6(a)). Fitting the FCS curves with the appropriate models, we could extract the relative reduction in observation volumes, which revealed that 3D-STED reduced observation volumes most effectively (Figure 7.6(b)), while z- and CH-STED also increased resolution significantly (about 10-15 fold reduction in observation volume). Resolution in 2D-STED was limited, as found in previous experiments [57]. Fitting FCS curves also allowed extraction of the average number of molecules in the observation volume (Figure 7.6(c)), which was minimal with CH-STED. This indicated a reduction in background noise, as expected from our previous results. To verify this, we plotted the relative variations of N as a function of V (Figure 7.6(d)), which confirmed that CH-STED exhibited the lowest background values. We also calculated the nRMSD of the curves

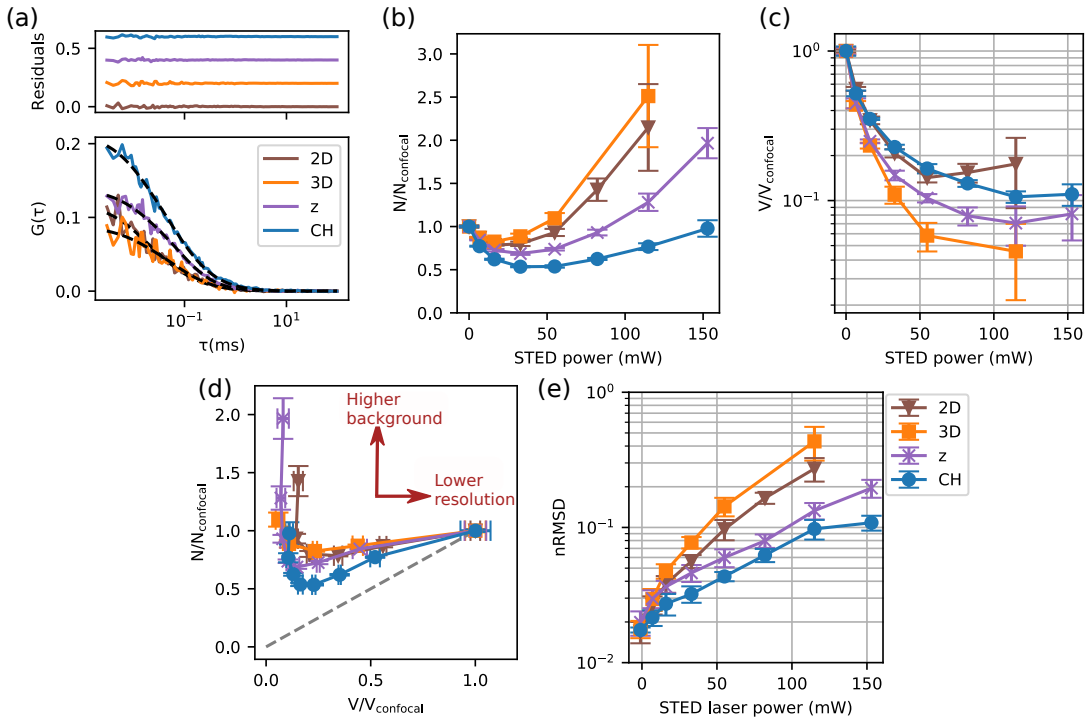

Figure 7.6: Comparison of different STED confinement modes for STED-FCS experiments in a solution of Abberior StarRed.(a) Bottom: STED-FCS curves obtained for all four confinement modes as indicated in the legend, at a STED laser power of 55 mW. Top: corresponding fitting residuals. (b,c) Variation of observation volume V(b) and average number of molecules N (c) with STED laser power for different STED confinement modes as indicated in the legend in panel (e). (d,e) Determination of background contributions using (d) N vs V pairwise plots (gray line: proportionality between N and V denoting an absence of background) and (e) normalised fitting residuals.

(Figure 7.6(e)), which confirmed that background noise levels were minimum with CH-STED.

7.4.3 Resistance against aberrations

The applicability of a technique is critical to facilitate its deployment. One of the reasons usually evocated explaining the relatively low deployment of z-STED (especially in FCS), is its large sensitivity to optical aberrations. Therefore, we investigated the sensitivity to aberrations of 2D-, z- and CH-STED. For this, we performed STED-FCS experiments in a solution of Abberior StarRed dyes, in which we first corrected aberrations using our adaptive correction method (developed in chapter 6) as we did throughout this chapter. This allowed us to ensure a perfect control over the aberrations present at any time in the system. We then introduced with the SLM known amounts of aberrations and acquired STED-FCS data with the different confinement modes (Figure 7.7). We compared the performance of these confinement modes in three different aberration regimes: first, in absence of aberration (0 rad rms of aberration introduced). The second regime corresponded to an aberration amplitude of 0.5 rad rms, corresponding to the typical amount of aberrations measured at low focusing depth (Figure 6.4 in chapter 6). The third regime (introduced aberration amplitude of 1 rad rms) corresponded to large aberrations found when focussing deep (15-20 µm) in presence of a refractive index mismatch, or when focusing deep through an optically inhomogeneous sample. In order to maximise the differences between 2D- and CH-STED, we set the value of the ρ parameter to 0.75, lower than in the rest of this chapter. We first evaluated the effects of spherical aberration on STED-FCS curves. As expected, spherical aberrations reduced the amplitude of z-STED-FCS curves the most (Figure 7.7(a-b)). To assess the impact of aberrations on STED-FCS quantita-

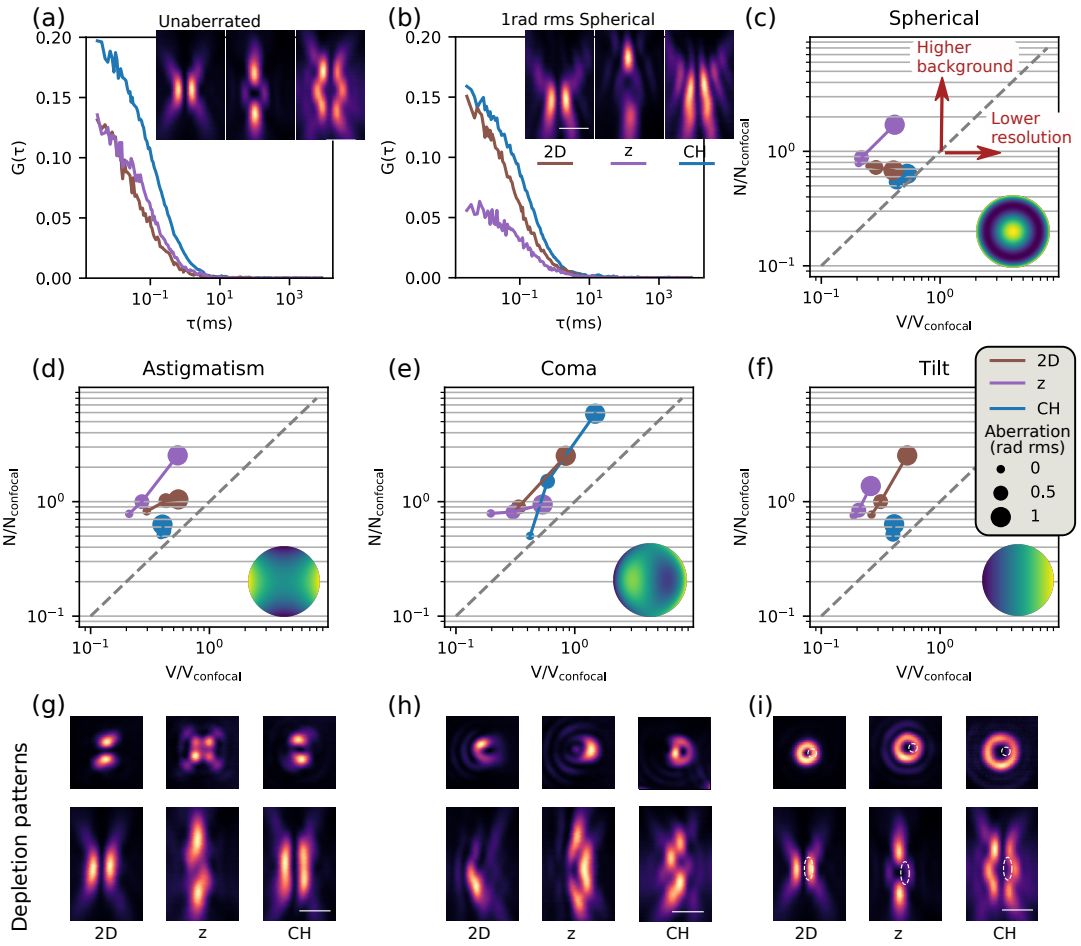

Figure 7.7: Effects of common aberration modes on the performance of STED-FCS experiments in a solution of Abberior StarRed dyes. (a,b) STED-FCS curves obtained in solution without (a) and with (b) 1 rad rms of spherical aberrations introduced in the depletion path with the SLM. Insets: corresponding depletion patterns imaged with a sample of scattering gold beads. (c-f) Pairwise N vs V plots for different STED confinement modes and different amounts of aberrations introduced as indicated in the legend in panel (f), for (c) primary spherical aberration, (d) astigmatism, (e) coma and (f) tilt. Inset: Phase distribution of the corresponding aberration modes. (g-i) Lateral (top) and axial (bottom) images of depletion patterns acquired with scattering gold beads upon introduction of 1 rad rms of (g) astigmatism, (h) coma and (i) tilt (white dotted ellipsoid: position of excitation focus). All scale bars: 1 µm. STED laser power: 16 mW.

tively, we fitted the curves to extract the relative variations in N and V in presence of aberrations (Figure 7.7(c)). This representation allowed to visualise at the same time decreases in resolution (as an increase of observation volume) and increase in background noise (as an increase in N for constant V). This revealed that spherical aberrations were particularly detrimental to z-STED as previously observed, while it had very little effect on CH-STED. Interestingly, introduction of spherical aberrations reduced background in 2D-STED, probably because of a better overlap between excitation and depletion beams due to axial elongation of 2D-STED (as can be seen in Figure 7.7(b)). Introducing astigmatism in the system (Figure 7.7(d)), we found again that z-STED displayed the highest sensitivity, while the performance of 2D-STED was only moderately reduced and that of CH-STED changed only marginally. Interestingly, visualising the corresponding depletion patterns in presence of 1 rad rms of astigmatism using gold beads (Figure 7.7(g)) revealed that the 2D- and CH-STED depletion patterns exhibited only two high-intensity lobes along one direction instead of their circular geometry. As a result, the loss of resolution along one direction was likely compensated by an increase in resolution along the other. Coma aberration (Figure 7.7(e,h)) was detrimental to all three confinement modes and particularly to CH- and 2-STED. Finally, we assessed the impact of a misalignment between excitation and depletion pattern (which can be caused for instance by drift of the system, as we observed in our experiments) using tilt (Figure 7.7(f,i)). The impact was most detrimental to 2D-STED, followed by z-STED and was minimal for CH-STED. These sensitivities to misalignments could be linked with the lateral size of the ring-shaped foci: distance between two intensity peaks was approximately 500 nm in 2D-STED, 700 nm for z-STED and 900 nm for CH-STED.

These results illustrate the sensitivity to optical aberrations of three confinement modes. They show in particular that, at the exception of coma, CH-STED was most re-

sistant against aberrations, especially to the very common spherical mode as predicted in previous work [30]. Due to the optical configuration used, we could not similarly assess the impact of aberrations on 3D-STED (created as an overlay between SLM-generated z-STED and phase-plate generated 2D-STED, without extra phase modulation possible). Sensitivity of 3D-STED to aberrations could be estimated from the results obtained with single phase masks and taking into account the effects of aberration-induced deformation that shift phase masks in different directions [134]. We used for each confinement mode a fitting model that supposed a given shape of the observation volume, calibrated with images of fluorescent beads. This model was well suited to fit unaberrated curves, however biases might have arised caused by the deformation of observation volumes in presence of aberrations. Besides, we performed these experiments at a single STED laser power and different effects might occur at different STED laser power. Therefore, these results are better understood qualitatively than quantitatively.

7.4.4 STED-FCS in living cells with different confinement modes

One of the great advantages of STED-FCS is its compatiblity with live-cell experiments [61]. Therefore, we determined the applicability of different STED confinement modes to perform STED-FCS measurements in the cytoplasm of living cells. We used for this a sample of human fibroblast expressing a cytoplasmic GFP-SNAP construct labelled with Silicon-Rhodamine (Figure 7.8(a)), which we used in chapter 6. This sample was used as a control as a part of a biological investigation and is therefore a perfect model sample for cytoplasmic investigations with STED-FCS. We investigated the performance of z-, 3D- and CH-STED, excluding 2D-STED which was consistently outperformed in our previous experiments (Figure 7.8(b)). Observation volumes were very similar with the

different confinement modes (Figure 7.8(c)). This was caused by two effects: first, a higher variability of STED-FCS measurements in cells caused by lower signal levels and higher heterogeneity induced a higher standard deviation of the measurement. This obscured the small difference in observation volume between the different confinement modes. Second, we used lower STED laser power than in calibration samples, to maximise signal values and to limit photobleaching as well as phototoxicity. We measured N for each confinement mode. To account for variations in label concentrations between cells, N was normalised with the value measured in confocal in the same cell (Figure 7.8(d)). As in solution, we found that N was minimised by CH-STED. This was again caused by an improvement in SBR, as shown by lower fitting residuals ((Figure 7.8(e)).

These measurements were performed with adaptive correction, determined once per microscope slide. We did not systematically assess the improvements brought by AO as we did in chapter 6, but results obtained in the previous section suggested that the predominantly spherical aberration we corrected would have affected z-STED-FCS much more than CH-STED-FCS. The impact on 3D-STED-FCS is however harder to assess, yet the only degradations of performance due to deformation of the z-STED depletion pattern suggest that the quality of 3D-STED-FCS would be more severely degraded than that of CH-STED-FCS. Overall, our results showed that CH-STED was superior to the other confinement modes in our cytoplasmic investigation.

7.5 Discussion

STED-FCS is a tool that has proven extremely useful in membrane research [121] thanks to its excellent and tunable spatial resolution as well as to its great temporal resolution. It was however seldomly used to study 3D diffusion, mainly due to high levels of

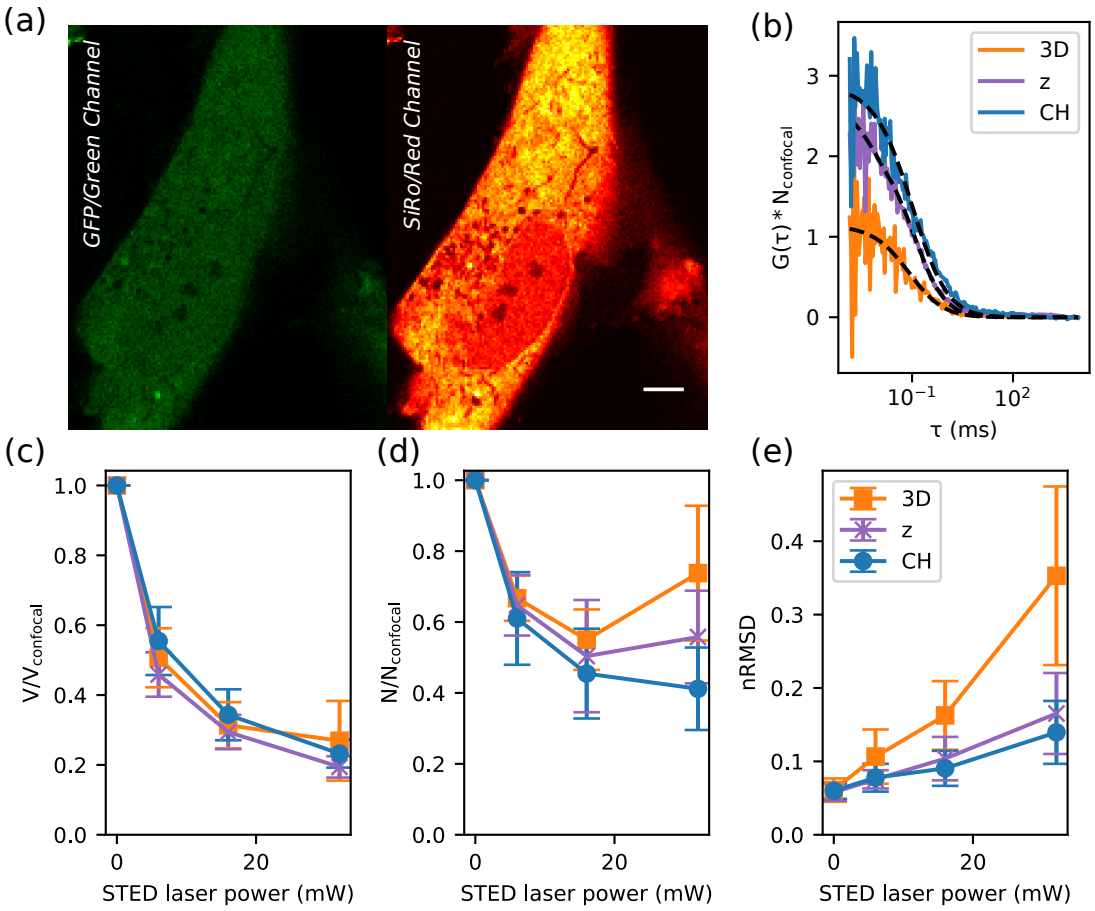

Figure 7.8: STED-FCS in the cytoplasm of living cells with different confinement modes to measure the diffusion of the protein GFP-SNAP, labelled with a SNAP silicon-rhodamine dye. (a) Exemplary confocal xy images of a cell used for STED-FCS experiments, with the green channel (left) collecting light from GFP and the red channel (right) collecting signal from SiRo. (b) STED-FCS curves and fits obtained with different confinement modes in the cytoplasm of a cell. (c,d) Observation volume V and average number of molecules N measured with STED-FCS at different STED laser powers and normalised with confocal values for different confinement modes as indicated in the legend of panel (e). (e) Estimation of background values using nRMSD at different STED laser power for different confinement modes.

undepleted background that reduce the quality of STED-FCS measurement and ultimately limit the maximum achievable resolutions. In this chapter, we investigated the origins of background in STED-FCS both experimentally and using simulations. We found that background was caused by an imperfect overlap between excitation and depletion foci. We explored how different confinement modes could be used to mitigate this issue, both in solution and in living cells and found that CH-STED removed undepleted background particularly efficiently.

We measured the sensitivity to optical aberrations of these different confinement modes, and found that CH-STED was extremely resistant against common aberration modes, especially against spherical aberrations. This should greatly facilitate the use of CH-STED-FCS, in particular in setups that cannot adaptively correct aberrations. Besides, the implementation of CH-STED-FCS is easy, especially in setups including a SLM in the depletion path which are readily commercially available an therefore CH-STED is a tool of choice for a wide use of STED-FCS in 3D. We characterised the performance of CH-STED together with FCS, yet these results (ease of use and resistance against aberrations) are also valid in the case of imaging. The reduction in background noise observed in STED-FCS corresponds to an increase in contrast in STED imaging, making CH-STED a useful tool in densely labelled specimens, as was previously found [30].

We developed in chapter 6 and in this chapter a new fitting model to take into account variations in the aspect ratio of the observation volume with STED laser power. This model has the advantage of accurately describing the shape of the observation volume, but is more complicated than usual models that fix either the lateral transit time [55] or the aspect ratio. CH-STED has the advantage of increasing both lateral and axial resolution and CH-STED aspect ratio could be approximated as a constant in most cases (see Figure 7.2) to simplify the data fitting procedure.

CH-STED physically removed undepleted background, as opposed to other methods based instead on photons filtering like gated STED-FCS [123] or SPLIT [64]. These techniques filter photons based on their average fluorescence lifetime, which depends itself on the local intensity of the STED focus: the fluorescence lifetime is shorter in presence of a high STED intensity. The absolute values of the fluorescence lifetime with and without STED laser are however dye-dependent, and these techniques therefore require a specific calibration for each dye used. This can be a problem in samples with spatially varying fluorescence lifetimes, while CH-STED could easily be used with such samples. Finally, as opposed to stimulated emission double depletion (STEDD) [27] or background substraction by polarisation switching (psSTED) [50], CH-STED does not require any modifications of the hardware and is therefore easier to implement. Besides, STEDD and psSTED both rely on a reduction of the fluorescence lifetime under STED conditions as in SPLIT and gated STED-FCS, and therefore suffer from the same shortcomings.

Chapter 8

Discussion and outlook

8.1 Discussion

We explored in this thesis the possibilities offered by wavefront shaping to improve STED microscopy, with a particular emphasis on 3D applications. Using a SLM as adaptive element, we developed a bespoke, adaptive optics-based calibration protocol that allowed our STED microscope to reach optimal performance. This excellent performance, combined with an efficient lipid labelling strategy that allows to bypass the usual limitations imposed on STED studies by photobleaching, allowed us to probe the 3D nanoscale structure and dynamics of living cells with exquisite details. To correct the effects of optical aberrations affecting STED images when focusing deeper in specimens, we developed a sensorless aberration correction method which proved to be functional in a wide variety of samples. To increase the performance of STED-FCS experiments, we developed a different aberration correction process which increased signal level, resolution and maximum focusing depth. We used this method as part of a wider biological investigation to study the diffusion modes of proteins in the cytoplasm in one of the very first studies of this kind, auguring a wealth of new applications. Finding that even an aberration-

free z-STED-FCS system had limited performance caused by undepleted background, we investigated the spatial origins of background in STED-FCS and minimised it using CH-STED, a new confinement mode recently developed that proved particularly effective at suppressing background in STED-FCS.

We therefore developed during this thesis a versatile toolbox relying on adaptive optics to increase the performance of STED microscopy and its variants in 3D. If most of this work consisted of improving the optical quality of a STED microscope (mostly by means of aberration correction), our study of lipid dynamics in living cells in chapter 4 highlighted the importance of the labelling strategy. This is particularly true in STED microscopy where photobleaching is usually considered to be a major limitation, much more than in most fluorescence microscopes. In our experiments, if photobleaching had to be considered (for instance in cytoplasmic measurements in chapter 6), this was essentially to avoid measurement biases. Photobleaching did not prevent measurements, rather imposed supplementary constraints on the design and parameters (typically, acquisition time) of experiments. The best mitigation to photobleaching was the use of self-replenishing fluorophores in chapter 4, yet even fixed samples with immobilised fluorophores were bright and stable enough to allow for the acquisition of multiple frames of the same field of view, therefore allowing sensorless aberration correction followed by volumetric imaging of the same area of the sample. This was off course allowed by the use of extremely photostable dyes (such as Silicon-Rhodamine or Abberior StarRed), which cannot yet be genetically expressed. This therefore limits the scope of applications, especially in living specimens where it is advantageous to use STED as compared with SMLM. An interesting alternative, however, consists of endogenously expressing a fluorescent protein with a SNAP tag and label this protein with a membrane permeable dye such as Silicon-Rhodamine, as we did in chapters 6-7. This approach brings the best of both worlds, with small tags genetically

expressed in the right locations and a STED-compatible dye labelling with high molecular brightness and stability.

We developed aberration correction methods for both STED imaging and STED-FCS. We applied these correction methods in a wide variety of samples like single cells and tissues. We measured and corrected many different aberration modes, with spherical aberrations being predominant. These were caused by a refractive index mismatch between the immersion oil of the objective, the aqueous medium in which samples were generally embedded and the sample itself. Imaging with an oil immersion objective through aqueous sample was a good system to develop and calibrate aberration correction systems, as they induced predictable amounts of aberrations, however future applications of the technology would further benefit from the use of an objective with an immersion medium minimising the refractive index mismatch with the sample (such as glycerol objectives for imaging brain slices [101]), with AO used to push the penetration depth even further.

We repeatedly found in our system a significant drift of the position of the depletion pattern with respect to excitation that deteriorated measurement performance. This was measured by using tip and tilt as aberration correction modes. The existence of drift in optical system is well known (and STED-specific misalignment between excitation and depletion was mentioned before [157]) and is sought to be minimised by mechanical design and temperature control of the imaging room. Despite these precautions, drift occurred in our system and probably does in other systems as well. Thanks to AO, we could both measure this drift and correct for it, therefore keeping an optimum microscope calibration throughout experiments.

The quality of the depletion focus is a key to the success of a STED experiment. Our experiments also revealed that at least in STED-FCS (and probably in STED imaging as well) the quality of the excitation focus is critical: indeed, we showed in chapter 7 that

the overlay between excitation and depletion was critical to limit undepleted background. In presence of aberrations, the size of the excitation focus increased while that of the depletion pattern remained the same thanks to aberration correction. This results in higher undepleted excitation intensity away from the observation area, leading to a reduction in SBR, but not an immediate loss of resolution which instead relied essentially on the depletion focus. This is what we observed upon focusing at increasing depths in aberrating medium with adaptive correction (Figure 6.4 in chapter 6). Full AO correction of all three beam paths (excitation, detection and depletion) is one way to get rid of this drawback, at the expense however of an even increased complexity.

We developed two adaptive correction methods in this thesis along with a graphical user interface for ease of use by non-specialists. This is not yet as simple as a push button interface and requires user input throughout the process. First, the choice and number of modes to correct are based either on prior information on the specimen structure or on a need to minimise correction time and photobleaching. Second, the results of aberration correction can be severely biased, for instance by a change of focus caused by axial drift in STED imaging, by large and bright molecular aggregates entering the observation focus in STED-FCS, or by specimen motion (for living specimens) in both. The current implementation therefore corrects a small number of modes at once, which are inspected by the user who chooses to either repeat the measurement if artefacts are detected, or to proceed with the correction procedure. The aberration correction procedure we developed therefore requires the user to have at least a limited understanding of the principles of AO deployed in this system.

In an apparent paradox, we believe that AO with a SLM made z-STED and z-STED-FCS easier to use than it is in conventional STED setups, where the z-STED depletion pattern is created thanks to a phase mask. At least three advantages come with the use

of a SLM: first, with a phase plate, the inner radius of the phase mask cannot be tuned and the size of the illumination profile has to be finely tuned to ensure a central intensity minimum, leading otherwise to a loss of performance. With a SLM, this parameter can be tuned without changing the optical setup. Second, the calibration procedure we developed in chapter 2 relies on AO and can significantly improve z-STED performance, as well as simplify the alignment procedure. Third, AO-based repositioning of the depletion pattern using tip and tilt proved to be extremely valuable, for initial calibration of the microscope using fluorescent beads and also for in-sample recalibration. As a result, if it is possible to use z-STED without a SLM, it would be much more impractical. Even without using adaptive correction within a specimen, having a SLM in a z-STED depletion beam brings major advantages.

Adaptive correction of aberration is generally simpler in STED-FCS than it is in STED imaging. Indeed, imaging experiments have to take into account the specimen structure (hence the need for elaborate quality metrics as explained in chapter 5). In certain specimens with either highly anisotropic features or that do not exhibit high frequency features, this can prevent an accurate correction. In STED-FCS in 3D, however, the specimen structure has no effect on the measurement and AO for STED-FCS is therefore more easily repeatable. Besides, photobleaching is much less of an issue in STED-FCS as fluorescent molecules in STED-FCS diffuse and therefore bleached molecules are continuously replaced with intact ones. Finally, STED-FCS is intrinsically a quantitative technique and it therefore benefits even more than imaging from aberration correction to measure unbiased diffusion parameters. Besides, the quantitative measurements obtained in STED-FCS make it easy to assess focus quality and therefore facilitate the development of aberration correction.

8.2 Outlook

8.2.1 Instrument development

We developed new aberration correction routines for STED microscopy using sensorless AO. This approach was functional, however requiring the acquisition of typically 5-7 measurements to correct one aberration mode and 50-70 measurements for a full aberration correction. This required the acquisition of a large number of photons: an average number of 1.7×10^6 photons per mode in STED imaging were acquired to obtain the results in Figure 5.8, and 8.5×10^5 in STED-FCS to obtain the results in Figure 6.3. Fortunately, photobleaching induced by these repeated measurements did not noticeably affect the correction procedure, but the long correction time can prevent aberration correction in dynamic systems like moving specimens. This also results effectively in a longer time to acquire STED and STED-FCS data, which severely complicates applications where many measurement points are required. Therefore, direct wavefront sensing for AO STED and STED-FCS is an interesting way forward. In 2-photon STED, it was already used with great success and proved able to correct aberrations for STED imaging in living brains [114]. It would be of interest to expand this work to the most common single photon STED and to STED-FCS.

We studied systems of axially close-by membranes, using z-STED and z-STED-FCS. In these systems, we found that axial motion complicated STED-FCS measurements as membranes left the observation volume if STED-FCS acquisition was too long. Coupling these measurements with fast axial scanning (faster than the average transit times, e.g in the kHz regime) using for instance a deformable mirror would solve this problem, allowing the quasi-simultaneous measurement of diffusion speed in two or more membranes.

Thanks to the capability of a DM to scan along all three dimensions indiscriminately, scanning z-STED-FCS could also be used to monitor subtle changes in diffusion properties across non-flat membranes in crowded environments, typically within organelles like the endoplasmic reticulum or mitochondria.

In this work, we corrected only phase aberrations. If these are ubiquitous in biological experiments, they are not the only defects that can limit the performance of STED microscopes. Certain biological specimens strongly affect the polarisation states of light [158, 159], which can in certain circumstances severely deteriorate the quality of STED measurements [104]. Using polarisation control devices [160, 161] in the depletion path of a STED microscope, one could develop new polarisation correction methods to compensate for these issues.

Finally, certain samples are also strongly scattering, which in STED might result in scattering of depletion photons across the entire imaging volume and particularly in the centre of the focus, leading to unwanted depletion of signal photons. Scattering compensation using adaptive optics has already been successfully developed in simpler microscopes [162] and the adaptation of such methods to STED microscopes might significantly increase the range of samples that can be investigated with STED.

8.2.2 Future applications

If interesting developments outlined above can further improve the AO-STED technology, the technologies developed during this DPhil project are now ready to be used for biological investigations. Defining use cases for AO-STED will also define new instrumentation needs that than can be iteratively met. The technological progresses achieved in this thesis in the field of STED-FCS in 3D can have multiple applications. The strength

of STED-FCS is its ability to measure diffusion speeds at different scales, down to the nanoscale. This in turn allows the measurement of different diffusion modes. This was widely used in 2D, but very few of such examples in 3D exist. To our knowledge, the only study of this kind used separation of photons by lifetime tuning (SPLIT) and STED-FCS to measure different diffusion modes of cytoplasmic tubulin [64]. Bacterial biofilms, which are known to exhibit non-Brownian diffusion [154] but could not be investigated down to the nanoscale, are an interesting system to study with the new techniques developed for this project. In general, biopolymers have been found to exhibit anomalous diffusion at different length scales [153], yet their diffusion properties at the nanoscale were not investigated due to a lack of appropriate methods. On top of the intrinsic scientific interest of studying the diffusion properties of fluorescent dyes in biopolymers, these systems could also serve as a positive control to estimate the sensitivity of the method. This would put our results of diffusion of peroxisomal matrix proteins in chapter 6 in perspective and allow us to verify that our technique indeed is capable of measuring different diffusion modes in 3D.

Combining our work on the study of membrane structure and dynamics in chapter 4 with the adaptive correction methods developed in chapters 5-6 will allow us to extend the membrane studies which are generally confined to single cells into tissues. A particularly promising area of research is the investigation of lipid structure and dynamics in neurons. Lipid composition and dynamics is thought to play a preeminent role in the formation of dendritic spines [163, 164], which are protrusions in dendrites where neuronal connexions are made. Yet direct evidence of this varying lipid composition is missing and could be uncovered using a combination of STED-FCS and polarity-sensitive dyes, as we used in chapter 4. Using adaptive optics, these measurements could be measured within tissues, typically in brain slices for maximum physiological relevance.

Bibliography

[1] J.-A. Conchello and J. W. Lichtman, "Optical sectioning microscopy", Nature Methods **2**, 920–931 (2005).

[2] L. A. Masullo, A. Bodén, F. Pennacchietti, et al., "Enhanced photon collection enables four dimensional fluorescence nanoscopy of living systems", Nature Communications **9**, 1–9 (2018).

[3] M. G. L. Gustafsson, "Surpassing the lateral resolution limit by a factor of two using structured illumination microscopy.", Journal of Microscopy **198**, 82–87 (2000).

[4] E. Betzig, G. H. Patterson, R. Sougrat, et al., "Imaging intracellular fluorescent proteins at nanometer resolution", Science **313**, 1642–1645 (2006).

[5] S. T. Hess, T. P. Girirajan, and M. D. Mason, "Ultra-high resolution imaging by fluorescence photoactivation localization microscopy", Biophysical Journal **91**, 4258–4272 (2006).

[6] M. J. Rust, M. Bates, and X. Zhuang, "Sub-diffraction-limit imaging by stochastic optical reconstruction microscopy (STORM)", Nature Methods **3**, 793–796 (2006).

[7] S. W. Hell and J. Wichmann, "Breaking the diffraction resolution limit by stimulated emission: stimulated-emission-depletion fluorescence microscopy", Optics Letters **19**, 780–782 (1994).

[8] T. A. Klar and S. W. Hell, "Subdiffraction resolution in far-field fluorescence microscopy", Optics Letters **24**, 954–956 (1999).

[9] A. Sharonov and R. M. Hochstrasser, "Wide-field subdiffraction imaging by accumulated binding of diffusing probes", PNAS **103**, 18911–18916 (2006).

[10] H. Kao and A. Verkman, "Tracking of single fluorescent particles in three dimensions: use of cylindrical optics to encode particle position", Biophysical Journal **67**, 1291–1300 (1994).

[11] B. Huang, W. Wang, M. Bates, et al., "Three-dimensional super-resolution imaging by stochastic optical reconstruction microscopy", Science **319**, 810–813 (2008).

[12] S. R. P. Pavani and R. Piestun, "Three dimensional tracking of fluorescent microparticles using a photon-limited double-helix response system", Optics Express **16**, 22048–22057 (2008).

[13] P. Bon, J. Linarès-Loyez, M. Feyeux, et al., "Self-interference 3d super-resolution microscopy for deep tissue investigations", Nature Methods **15**, 449–454 (2018).

[14] N. Bourg, C. Mayet, G. Dupuis, et al., "Direct optical nanoscopy with axially localized detection", Nature Photonics **9**, 587–593 (2015).

[15] F. Balzarotti, Y. Eilers, K. C. Gwosch, et al., "Nanometer resolution imaging and tracking of fluorescent molecules with minimal photon fluxes", Science **355**, 606–612 (2017).

[16] K. C. Gwosch, J. K. Pape, F. Balzarotti, et al., "MINFLUX nanoscopy delivers 3d multicolor nanometer resolution in cells", Nature Methods **17**, 217–224 (2020).

[17] J. Keller, A. Schönle, and S. W. Hell, "Efficient fluorescence inhibition patterns for RESOLFT microscopy", Optics Express **15**, 3361–3371 (2007).

[18] T. Grotjohann, I. Testa, M. Leutenegger, et al., "Diffraction-unlimited all-optical imaging and writing with a photochromic GFP", Nature **478**, 204–208 (2011).

[19] V. Westphal and S. W. Hell, "Nanoscale resolution in the focal plane of an optical microscope", Physical Review Letters **94**, 143903 (2005).

[20] B. Harke, J. Keller, C. K. Ullal, et al., "Resolution scaling in STED microscopy", Optics Express **16**, 4154–4162 (2008).

[21] S. W. Hell, "Toward fluorescence nanoscopy", Nature Biotechnology **21**, 1347–1355 (2003).

[22] K. I. Willig, R. R. Kellner, R. Medda, et al., "Nanoscale resolution in GFP-based microscopy", Nature Methods **3**, 721–723 (2006).

[23] S. Deng, L. Liu, Y. Cheng, et al., "Effects of primary aberrations on the fluorescence depletion patterns of STED microscopy", Optics Express **18**, 1657–1666 (2010).

[24] Y. Li, H. Zhou, X. Liu, et al., "Effects of aberrations on effective point spread function in STED microscopy", Applied Optics **57**, 4164–4170 (2018).

[25] J. Antonello, D. Burke, and M. J. Booth, "Aberrations in stimulated emission depletion (STED) microscopy", Optics Communications **404**, 203–209 (2017).

[26] B. Hein, K. I. Willig, and S. W. Hell, "Stimulated emission depletion (STED) nanoscopy of a fluorescent protein-labeled organelle inside a living cell", Proceedings of the National Academy of Sciences **105**, 14271–14276 (2008).

[27] P. Gao, B. Prunsche, L. Zhou, et al., "Background suppression in fluorescence nanoscopy with stimulated emission double depletion", Nature Photonics **11**, 163–169 (2017).

[28] T. A. Klar, S. Jakobs, M. Dyba, et al., "Fluorescence microscopy with diffraction resolution barrier broken by stimulated emission", Proceedings of the National Academy of Sciences **97**, 8206–8210 (2000).

[29] B. Wang, J. Shi, T. Zhang, et al., "Improved lateral resolution with an annular vortex depletion beam in STED microscopy", Optics Letters **42**, 4885–4888 (2017).

[30] A. Pereira, M. Sousa, A. C. Almeida, et al., "Coherent-hybrid STED: high contrast sub-diffraction imaging using a bi-vortex depletion beam", Optics Express **27**, 8092–8111 (2019).

[31] B. Yang, F. Przybilla, M. Mestre, et al., "Large parallelization of STED nanoscopy using optical lattices", Optics Express **22**, 5581–5589 (2014).

[32] A. Chmyrov, J. Keller, T. Grotjohann, et al., "Nanoscopy with more than 100,000 'doughnuts'", Nature Methods **10**, 737–740 (2013).

[33] A. Bodén, F. Pennacchietti, and I. Testa, *Three dimensional parallelized RESOLFT nanoscopy for volumetric live cell imaging*, preprint (bioRxiv, Jan. 9, 2020).

[34] T. J. Gould, J. R. Myers, and J. Bewersdorf, "Total internal reflection STED microscopy", Optics Express **19**, 13351–13357 (2011).

[35] S. Sivankutty, I. Coto Hernández, N. Bourg, et al., "Supercritical angle fluorescence for enhanced axial sectioning in STED microscopy", Methods **174**, 20–26 (2020).

[36] M. Dyba, S. Jakobs, and S. W. Hell, "Immunofluorescence stimulated emission depletion microscopy", Nature Biotechnology **21**, 1303–1304 (2003).

[37] R. Schmidt, C. A. Wurm, A. Punge, et al., "Mitochondrial cristae revealed with focused light", Nano Letters **9**, 2508–2510 (2009).

[38] R. Schmidt, C. A. Wurm, S. Jakobs, et al., "Spherical nanosized focal spot unravels the interior of cells", Nature Methods **5**, 539–544 (2008).

[39] H. Gugel, J. Bewersdorf, S. Jakobs, et al., "Cooperative 4pi excitation and detection yields sevenfold sharper optical sections in live-cell microscopy", Biophysical Journal **87**, 4146–4152 (2004).

[40] X. Hao, E. S. Allgeyer, M. J. Booth, et al., "Point-spread function optimization in isoSTED nanoscopy", Optics Letters **40**, 3627–3630 (2015).

[41] T. Staudt, A. Engler, E. Rittweger, et al., "Far-field optical nanoscopy with reduced number of state transition cycles", Optics Express **19**, 5644–5657 (2011).

[42] J. Heine, C. A. Wurm, J. Keller-Findeisen, et al., "Three dimensional live-cell STED microscopy at increased depth using a water immersion objective", Review of Scientific Instruments **89**, 053701 (2018).

[43] C. Osseforth, J. R. Moffitt, L. Schermelleh, et al., "Simultaneous dual-color 3d STED microscopy", Optics Express **22**, 7028–7039 (2014).

[44] D. Wildanger, R. Medda, L. Kastrup, et al., "A compact STED microscope providing 3d nanoscale resolution", Journal of Microscopy **236**, 35–43 (2009).

[45] B. Harke, C. K. Ullal, J. Keller, et al., "Three-dimensional nanoscopy of colloidal crystals", Nano Letters **8**, 1309–1313 (2008).

[46] D. Unnersjö-Jess, L. Scott, H. Blom, et al., "Super-resolution stimulated emission depletion imaging of slit diaphragm proteins in optically cleared kidney tissue", Kidney International **89**, 243–247 (2016).

[47] F. Göttfert, T. Pleiner, J. Heine, et al., "Strong signal increase in STED fluorescence microscopy by imaging regions of subdiffraction extent", Proceedings of the National Academy of Sciences **114**, 2125–2130 (2017).

[48] J. Heine, M. Reuss, B. Harke, et al., "Adaptive-illumination STED nanoscopy", Proceedings of the National Academy of Sciences **114**, 9797–9802 (2017).

[49] C. Spahn, J. B. Grimm, L. D. Lavis, et al., "Whole-cell, 3d, and multicolor STED imaging with exchangeable fluorophores", Nano Letters **19**, 500–505 (2019).

[50] J.-C. Lee, Y. Ma, K. Y. Han, et al., "Accurate background subtraction in STED nanoscopy by polarization switching", ACS Photonics **6**, 1789–1797 (2019).

[51] W. Zhang, A. Noa, K. Nienhaus, et al., "Super-resolution imaging of densely packed DNA in nuclei of zebrafish embryos using stimulated emission double depletion microscopy", Journal of Physics D: Applied Physics **52**, 414001 (2019).

[52] J. R. Lakowicz, *Principles of fluorescence spectroscopy*, Third edition (Springer, New York, 2006), 954 pp.

[53] H. Blom and G. Björk, "Lorentzian spatial intensity distribution in one-photon fluorescence correlation spectroscopy", Applied Optics **48**, 6050 (2009).

[54] H. Qian and E. L. Elson, "Distribution of molecular aggregation by analysis of fluctuation moments.", Proceedings of the National Academy of Sciences **87**, 5479–5483 (1990).

[55] L. Kastrup, H. Blom, C. Eggeling, et al., "Fluorescence fluctuation spectroscopy in subdiffraction focal volumes", Physical Review Letters **94**, 178104 (2005).

[56] C. Eggeling, C. Ringemann, R. Medda, et al., "Direct observation of the nanoscale dynamics of membrane lipids in a living cell", Nature **457**, 1159–1162 (2009).

[57] C. Ringemann, B. Harke, C. von Middendorff, et al., "Exploring single-molecule dynamics with fluorescence nanoscopy", New Journal of Physics **11**, 103054 (2009).

[58] D. M. Andrade, M. P. Clausen, J. Keller, et al., "Cortical actin networks induce spatio-temporal confinement of phospholipids in the plasma membrane – a minimally invasive investigation by STED-FCS", Scientific Reports **5**, 11454 (2015).

[59] S. Galiani, D. Waithe, K. Reglinski, et al., "Super-resolution microscopy reveals compartmentalization of peroxisomal membrane proteins", Journal of Biological Chemistry **291**, 16948–16962 (2016).

[60] F. Schneider, D. Waithe, M. P. Clausen, et al., "Diffusion of lipids and GPI-anchored proteins in actin-free plasma membrane vesicles measured by STED-FCS", Molecular Biology of the Cell **28**, 1507–1518 (2017).

[61] E. Sezgin, F. Schneider, S. Galiani, et al., "Measuring nanoscale diffusion dynamics in cellular membranes with super-resolution STED–FCS", Nature Protocols **14**, 1054–1083 (2019).

[62] K. Sozanski, E. Sisamakis, X. Zhang, et al., "Quantitative fluorescence correlation spectroscopy in three-dimensional systems under stimulated emission depletion conditions", Optica **4**, 982–988 (2017).

[63] M. Leutenegger, C. Ringemann, T. Lasser, et al., "Fluorescence correlation spectroscopy with a total internal reflection fluorescence STED microscope (TIRF-STED-FCS)", Optics Express **20**, 5243–5263 (2012).

[64] L. Lanzanò, L. Scipioni, M. Di Bona, et al., "Measurement of nanoscale three-dimensional diffusion in the interior of living cells by STED-FCS", Nature Communications **8**, 65 (2017).

[65] M. Schwertner, M. Booth, and T. Wilson, "Characterizing specimen induced aberrations for high NA adaptive optical microscopy", Optics Express **12**, 6540–6552 (2004).

[66] O. Azucena, J. Crest, J. Cao, et al., "Wavefront aberration measurements and corrections through thick tissue using fluorescent microsphere reference beacons", Optics Express **18**, 17521–17532 (2010).

[67] J. Zeng, P. Mahou, M.-C. Schanne-Klein, et al., "3d resolved mapping of optical aberrations in thick tissues", Biomedical Optics Express **3**, 1898–1913 (2012).

[68] R. J. Noll, "Zernike polynomials and atmospheric turbulence", Journal of the Optical Society of America **66**, 207–211 (1976).

[69] O. Azucena, J. Crest, S. Kotadia, et al., "Adaptive optics wide-field microscopy using direct wavefront sensing", Optics Letters **36**, 825–827 (2011).

[70] X. Tao, B. Fernandez, O. Azucena, et al., "Adaptive optics confocal microscopy using direct wavefront sensing", Optics Letters **36**, 1062–1064 (2011).

[71] X. Tao, O. Azucena, M. Fu, et al., "Adaptive optics microscopy with direct wavefront sensing using fluorescent protein guide stars", Optics Letters **36**, 3389–3391 (2011).

[72] J. W. Cha, J. Ballesta, and P. T. C. So, "Shack-hartmann wavefront-sensor-based adaptive optics system for multiphoton microscopy", Journal of Biomedical Optics **15**, 046022 (2010).

[73] S. A. Rahman and M. J. Booth, "Direct wavefront sensing in adaptive optical microscopy using backscattered light", Applied Optics **52**, 5523 (2013).

[74] R. Aviles-Espinosa, J. Andilla, R. Porcar-Guezenec, et al., "Measurement and correction of in vivo sample aberrations employing a nonlinear guide-star in two-photon excited fluorescence microscopy", Biomedical Optics Express **2**, 3135–3149 (2011).

[75] K. Wang, D. E. Milkie, A. Saxena, et al., "Rapid adaptive optical recovery of optimal resolution over large volumes", Nature Methods **11**, 625–628 (2014).

[76] M. Feierabend, M. Rückel, and W. Denk, "Coherence-gated wave-front sensing in strongly scattering samples", Optics Letters **29**, 2255–2257 (2004).

[77] M. Rueckel, J. A. Mack-Bucher, and W. Denk, "Adaptive wavefront correction in two-photon microscopy using coherence-gated wavefront sensing", Proceedings of the National Academy of Sciences **103**, 17137–17142 (2006).

[78] Robert Gonsalvez, "Phase retrieval and diversity in adaptive optics", Optical Engineering **21**, 829–832 (1982).

[79] B. M. Hanser, M. G. L. Gustafsson, D. A. Agard, et al., "Phase-retrieved pupil functions in wide-field fluorescence microscopy", Journal of Microscopy **216**, 32–48 (2004).

[80] S. Liu, E. B. Kromann, W. D. Krueger, et al., "Three dimensional single molecule localization using a phase retrieved pupil function", Optics Express **21**, 29462–29487 (2013).

[81] A. Aristov, B. Lelandais, E. Rensen, et al., "ZOLA-3d allows flexible 3d localization microscopy over an adjustable axial range", Nature Communications **9**, 2409 (2018).

[82] F. Xu, M. Donghan, K. P. MacPherson, et al., "Three-dimensional nanoscopy of whole cells and tissues with in situ point spread function retrieval", Nature Methods **17**, 531–540 (2020).

[83] D. Débarre, T. Vieille, and E. Beaurepaire, "Simple characterisation of a deformable mirror inside a high numerical aperture microscope using phase diversity", Journal of Microscopy **244**, 136–143 (2011).

[84] E. B. Kromann, T. J. Gould, M. F. Juette, et al., "Quantitative pupil analysis in stimulated emission depletion microscopy using phase retrieval", Optics Letters **37**, 1805–1807 (2012).

[85] M. A. A. Neil, M. J. Booth, and T. Wilson, "New modal wave-front sensor: a theoretical analysis", Journal of the Optical Society of America A **17**, 1098 (2000).

[86] M. A. A. Neil, R. Juskaitis, M. J. Booth, et al., "Adaptive aberration correction in a two-photon microscope", Journal of Microscopy **200**, 105–108 (2000).

[87] M. J. Booth, M. A. A. Neil, R. Juskaitis, et al., "Adaptive aberration correction in a confocal microscope", Proceedings of the National Academy of Sciences **99**, 5788–5792 (2002).

[88] N. Ji, D. E. Milkie, and E. Betzig, "Adaptive optics via pupil segmentation for high-resolution imaging in biological tissues", Nature Methods **7**, 141–147 (2010).

[89] D. Débarre, E. J. Botcherby, T. Watanabe, et al., "Image-based adaptive optics for two-photon microscopy", Optics Letters **34**, 2495–2497 (2009).

[90] J. Scrimgeour and J. E. Curtis, "Aberration correction in wide-field fluorescence microscopy by segmented-pupil image interferometry", Optics Express **20**, 14534–14541 (2012).

[91] D. Débarre, E. J. Botcherby, M. J. Booth, et al., "Adaptive optics for structured illumination microscopy", Optics Express **16**, 9290–9305 (2008).

[92] M. Žurauskas, I. M. Dobbie, R. M. Parton, et al., "IsoSense: frequency enhanced sensorless adaptive optics through structured illumination", Optica **6**, 370–379 (2019).

[93] D. Burke, B. Patton, F. Huang, et al., "Adaptive optics correction of specimen-induced aberrations in single-molecule switching microscopy", Optica **2**, 177 (2015).

[94] T. J. Gould, D. Burke, J. Bewersdorf, et al., "Adaptive optics enables 3d STED microscopy in aberrating specimens", Optics Express **20**, 20998–21009 (2012).

[95] S. T. Hess and W. W. Webb, "Focal volume optics and experimental artifacts in confocal fluorescence correlation spectroscopy", Biophysical Journal **83**, 2300–2317 (2002).

[96] C.-E. Leroux, I. Wang, J. Derouard, et al., "Adaptive optics for fluorescence correlation spectroscopy", Optics Express **19**, 26839–26849 (2011).

[97] C.-E. Leroux, A. Grichine, I. Wang, et al., "Correction of cell-induced optical aberrations in a fluorescence fluctuation microscope", Optics Letters **38**, 2401–2403 (2013).

[98] C.-E. Leroux, S. Monnier, I. Wang, et al., "Fluorescent correlation spectroscopy measurements with adaptive optics in the intercellular space of spheroids", Biomedical Optics Express **5**, 3730–3738 (2014).

[99] J. Gallagher, A. Delon, P. Moreau, et al., "Optimizing the metric in sensorless adaptive optical microscopy with fluorescence fluctuations", Optics Express **25**, 15558–15571 (2017).

[100] N. T. Urban, K. I. Willig, S. W. Hell, et al., "STED nanoscopy of actin dynamics in synapses deep inside living brain slices", Biophysical Journal **101**, 1277–1284 (2011).

[101] J. Tønnesen, V. K. Inavalli, and U. V. Nägerl, "Super-resolution imaging of the extracellular space in living brain tissue", Cell **172**, 1108–1121 (2018).

[102] M. O. Lenz, H. G. Sinclair, A. Savell, et al., "3-d stimulated emission depletion microscopy with programmable aberration correction: 3-d STED microscopy with programmable aberration correction", Journal of Biophotonics **7**, 29–36 (2014).

[103] S. Deng, L. Liu, Y. Cheng, et al., "Investigation of the influence of the aberration induced by a plane interface on STED microscopy", Optics Express **17**, 1714–1725 (2009).

[104] X. Chen, J. Chen, S. Dong, et al., "Effects of seidel aberration and light polarization on the resolution of STED imaging", Optik **130**, 76–81 (2017).

[105] B. R. Patton, D. Burke, R. Vrees, et al., "Is phase-mask alignment aberrating your STED microscope?", Methods and Applications in Fluorescence **3**, 024002 (2015).

[106] Y. Zhang, C. Wu, Y. Song, et al., "Machine learning based adaptive optics for doughnut-shaped beam", Optics Express **27**, 16871–16881 (2019).

[107] A. Klauss, F. Conrad, and C. Hille, "Binary phase masks for easy system alignment and basic aberration sensing with spatial light modulators in STED microscopy", Scientific Reports **7**, 15699 (2017).

[108] T. J. Gould, E. B. Kromann, D. Burke, et al., "Auto-aligning stimulated emission depletion microscope using adaptive optics", Optics Letters **38**, 1860–1862 (2013).

[109] B. R. Patton, D. Burke, D. Owald, et al., "Three-dimensional STED microscopy of aberrating tissue using dual adaptive optics", Optics Express **24**, 8862–8876 (2016).

[110] P. Zdańkowski, D. McGloin, and J. R. Swedlow, "Full volume super-resolution imaging of thick mitotic spindle using 3d AO STED microscope", Biomedical Optics Express **10**, 1999–2009 (2019).

[111] P. Zdańkowski, M. Trusiak, D. McGloin, et al., "Numerically enhanced stimulated emission depletion microscopy with adaptive optics for deep-tissue super-resolved imaging", ACS Nano **14**, 394–405 (2020).

[112] W. Yan, Y. Yang, Y. Tan, et al., "Coherent optical adaptive technique improves the spatial resolution of STED microscopy in thick samples", Photonics Research **5**, 176 (2017).

[113] L. Wang, W. Yan, R. Li, et al., "Aberration correction for improving the image quality in STED microscopy using the genetic algorithm", Nanophotonics **7**, 1971–1980 (2018).

[114] M. G. M. Velasco, M. Zhang, J. Antonello, et al., *3d super-resolution deep-tissue imaging in living mice*, preprint (bioRxiv, Oct. 2, 2019).

[115] M. G. M. Velasco, "Three-dimensional STED microscopy for deep-tissue applications", PhD thesis (Yale University, Dec. 2019), 101 pp.

[116] Y. Dai, J. Antonello, and M. J. Booth, "Calibration of a phase-only spatial light modulator for both phase and retardance modulation", Optics Express **27**, 17912–17926 (2019).

[117] A. Barbotin, "Alignment of an SLM-based STED depletion beam (v1.0)", Zenodo, 8 (2020).

[118] S. Galiani, B. Harke, G. Vicidomini, et al., "Strategies to maximize the performance of a STED microscope", Optics Express **20**, 7362–7374 (2012).

[119] J. Antonello, A. Barbotin, E. Z. Chong, et al., "Multi-scale sensorless adaptive optics: application to stimulated emission depletion microscopy", Optics Express **28**, 16749–16763 (2020).

[120] E. Auksorius, B. R. Boruah, C. Dunsby, et al., "Stimulated emission depletion microscopy with a supercontinuum source and fluorescence lifetime imaging", Optics Letters **33**, 113–115 (2008).

[121] E. Sezgin, I. Levental, S. Mayor, et al., "The mystery of membrane organization: composition, regulation and roles of lipid rafts", Nature Reviews Molecular Cell Biology **18**, 361–374 (2017).

[122] A. Barbotin, I. Urbančič, S. Galiani, et al., "Z-STED imaging and spectroscopy to investigate nanoscale membrane structure and dynamics", Biophysical Journal **118**, 2448–2457 (2020).

[123] M. P. Clausen, E. Sezgin, J. Bernardino de la Serna, et al., "A straightforward approach for gated STED-FCS to investigate lipid membrane dynamics", Methods **88**, 67–75 (2015).

[124] E. Sezgin and P. Schwille, "Fluorescence techniques to study lipid dynamics", Cold Spring Harbor Perspectives in Biology **3**, a009803 (2011).

[125] E. Sezgin, D. Waithe, J. B. d. l. Serna, et al., "Spectral imaging to measure heterogeneity in membrane lipid packing", ChemPhysChem **16**, 1387–1394 (2015).

[126] M. Nawaz and F. Fatima, "Extracellular vesicles, tunneling nanotubes, and cellular interplay: synergies and missing links", Frontiers in Molecular Biosciences **4**, 50 (2017).

[127] N. Sofroniew, T. Lambert, K. Evans, et al., *Napari/napari: 0.4.2rc0*, version v0.4.2rc0, 2020.

[128] V. Mueller, C. Ringemann, A. Honigmann, et al., "STED nanoscopy reveals molecular details of cholesterol- and cytoskeleton-modulated lipid interactions in living cells", Biophysical Journal **101**, 1651–1660 (2011).

[129] E. Sezgin, T. Gutmann, T. Buhl, et al., "Adaptive lipid packing and bioactivity in membrane domains", PLOS ONE **10**, edited by L. Johannes, e0123930 (2015).

[130] O. A. Kucherak, S. Oncul, Z. Darwich, et al., "Switchable nile red-based probe for cholesterol and lipid order at the outer leaflet of biomembranes", Journal of the American Chemical Society **132**, 4907–4916 (2010).

[131] E. Sezgin, F. Schneider, V. Zilles, et al., "Polarity-sensitive probes for superresolution stimulated emission depletion microscopy", Biophysical Journal **113**, 1321–1330 (2017).

[132] J. Ries, S. R. Yu, M. Burkhardt, et al., "Modular scanning FCS quantifies receptor-ligand interactions in living multicellular organisms", Nature Methods **6**, 643–645 (2009).

[133] M.-T. Wei, S. Elbaum-Garfinkle, A. S. Holehouse, et al., "Phase behaviour of disordered proteins underlying low density and high permeability of liquid organelles", Nature Chemistry **9**, 1118–1125 (2017).

[134] J. Antonello, E. B. Kromann, D. Burke, et al., "Coma aberrations in combined two- and three-dimensional STED nanoscopy", Optics Letters **41**, 3631–3634 (2016).

[135] V. V. G. K. Inavalli, M. O. Lenz, C. Butler, et al., "A super-resolution platform for correlative live single-molecule imaging and STED microscopy", Nature Methods **16**, 1263–1268 (2019).

[136] H. Colin-York, C. Eggeling, and M. Fritzsche, "Dissection of mechanical force in living cells by super-resolved traction force microscopy", Nature Protocols **12**, 783–796 (2017).

[137] J. Tröger, C. Hoischen, B. Perner, et al., "Comparison of multiscale imaging methods for brain research", Cells **9**, 1377 (2020).

[138] B. M. Hanser, M. G. L. Gustafsson, D. A. Agard, et al., "Phase retrieval for high-numerical-aperture optical systems", Optics Letters **28**, 801–803 (2003).

[139] P. Török, P. Varga, and G. Németh, "Analytical solution of the diffraction integrals and interpretation of wave-front distortion when light is focused through a planar interface between materials of mismatched refractive indices", Journal of the Optical Society of America A **12**, 2660 (1995).

[140] J.-L. Starck, J. Fadili, and F. Murtagh, "The undecimated wavelet decomposition and its reconstruction", IEEE Transactions on Image Processing **16**, 297–309 (2007).

[141] S. Koho, G. Tortarolo, M. Castello, et al., "Fourier ring correlation simplifies image restoration in fluorescence microscopy", Nature Communications **10**, 3103 (2019).

[142] A. Facomprez, E. Beaurepaire, and D. Débarre, "Accuracy of correction in modal sensorless adaptive optics", Optics Express **20**, 2598 (2012).

[143] D. S. Banks and C. Fradin, "Anomalous diffusion of proteins due to molecular crowding", Biophysical Journal **89**, 2960–2971 (2005).

[144] G. Meacci, J. Ries, E. Fischer-Friedrich, et al., "Mobility of min-proteins in escherichia coli measured by fluorescence correlation spectroscopy", Physical Biology **3**, 255–263 (2006).

[145] G. Tortarolo, Y. Sun, K. W. Teng, et al., "Photon-separation to enhance the spatial resolution of pulsed STED microscopy", Nanoscale **11**, 1754–1761 (2019).

[146] R. Wang, S. Brustlein, S. Mailfert, et al., "A straightforward STED-background corrected fitting model for unbiased STED-FCS analyses", Methods **140-141**, 212–222 (2018).

[147] A. Barbotin, S. Galiani, I. Urbančič, et al., "Adaptive optics allows STED-FCS measurements in the cytoplasm of living cells", Optics Express **27**, 23378–23395 (2019).

[148] P. Müller, *Python multiple-tau algorithm*, version 0.1.9, 2012.

[149] M. Weiss, M. Elsner, F. Kartberg, et al., "Anomalous subdiffusion is a measure for cytoplasmic crowding in living cells", Biophysical Journal **87**, 3518–3524 (2004).

[150] F. Schneider, P. Hernandez-Varas, B. Christoffer Lagerholm, et al., "High photon count rates improve the quality of super-resolution fluorescence fluctuation spectroscopy", Journal of Physics D: Applied Physics **53**, 164003 (2020).

[151] D. Waithe, F. Schneider, J. Chojnacki, et al., "Optimized processing and analysis of conventional confocal microscopy generated scanning FCS data", Methods **140-141**, 62–73 (2018).

[152] K. D. Niswender, S. M. Blackman, L. Rohde, et al., "Quantitative imaging of green fluorescent protein in cultured cells: comparison of microscopic techniques, use in fusion proteins and detection limits", Journal of Microscopy **180**, 109–116 (1995).

[153] D. S. Banks, C. Tressler, R. D. Peters, et al., "Characterizing anomalous diffusion in crowded polymer solutions and gels over five decades in time with variable-lengthscale fluorescence correlation spectroscopy", Soft Matter **12**, 4190–4203 (2016).

[154] V. Dunsing, T. Irmscher, S. Barbirz, et al., "Purely polysaccharide-based biofilm matrix provides size-selective diffusion barriers for nanoparticles and bacteriophages", Biomacromolecules **20**, 3842–3854 (2019).

[155] Y. Ma and T. Ha, "Fight against background noise in stimulated emission depletion nanoscopy", Physical Biology **16**, 051002 (2019).

[156] A. Barbotin, I. Urbančič, S. Galiani, et al., "Background reduction in STED-FCS using a bivortex phase mask", ACS Photonics **7**, 1742–1753 (2020).

[157] P. Mahou, N. Curry, D. Pinotsi, et al., "Simulated emission depletion microscopy to study amyloid fibril formation", Single Molecule Spectroscopy and Superresolution Imaging VIII **9331**, 93310U (2015).

[158] S. Jiao and L. V. Wang, "Two-dimensional depth-resolved mueller matrix of biological tissue measured with double-beam polarization-sensitive optical coherence tomography", Optics Letters **27**, 101–103 (2002).

[159] A. Pierangelo, A. Benali, M.-R. Antonelli, et al., "Ex-vivo characterization of human colon cancer by mueller polarimetric imaging", Optics Express **19**, 1582–1593 (2011).

[160] F. Kenny, D. Lara, O. G. Rodríguez-Herrera, et al., "Complete polarization and phase control for focus-shaping in high-NA microscopy", Optics Express **20**, 14015–14029 (2012).

[161] C. He, J. Chang, Q. Hu, et al., "Complex vectorial optics through gradient index lens cascades", Nature Communications **10**, 4264 (2019).

[162] I. M. Vellekoop and A. P. Mosk, "Focusing coherent light through opaque strongly scattering media", Optics Letters **32**, 2309–2311 (2007).

[163] H. Hering, C.-C. Lin, and M. Sheng, "Lipid rafts in the maintenance of synapses, dendritic spines, and surface AMPA receptor stability", The Journal of Neuroscience **23**, 3262–3271 (2003).

[164] C. G. Dotti, J. A. Esteban, and M. D. Ledesma, "Lipid dynamics at dendritic spines", Frontiers in Neuroanatomy **8**, 76 (2014).